Eindhoven University of Technology

MASTER

Atomic Beam Laser-cooled Ion Source : towards sub-nm ion beam milling

ten Haaf, G.

Award date:
2013

Link to publication

Eindhoven University of Technology
Department of Applied Physics
Coherence and Quantum Technology (CQT)

Atomic Beam Laser-cooled Ion Source: towards sub-nm ion beam milling

G. ten Haaf

CQT 2013-10

Supervisors:

dr.ir. E.J.D. Vredenbregt

ir. S.H.W. Wouters

Abstract

This report discusses the performance of the Atomic Beam Laser-cooled Ion Source (ABLIS) and the progress in its experimental realization. The ABLIS is a new source for focused ion beams (FIBs), which are tools that are used on a large scale in the semiconductor industry, to image and modify structures on the smallest possible length scale. In contrast to other FIB sources such as the Liquid Metal Ion Source (LMIS), the ABLIS is based on the fact that the ions are created with a very small spread in velocity instead of a very small spread in position. The main application of an ABLIS-based FIB will be so-called milling in which material is physically etched at the nanometer length scale.

In the ABLIS setup, a beam of atomic rubidium is created from a Knudsen cell. This beam is laser-cooled and -compressed, after which it is photo-ionized by means of two intense lasers. The ions are accelerated immediately to their required energy (mostly 30 keV) and finally focused to an as small as possible spot by a set of electrostatic lenses. Since the ionization will take place over a certain region, the energy spread of the ion beam, and thus also the amount of chromatic aberration of the lens system, will be proportional to the electric field.

The bottleneck of the setup is disorder-induced heating; ions, created at random initial positions, heat up due to relaxation of the potential energy associated with these positions. Investigations in this report show that this effect can be counteracted by applying a large electric field to quickly reduce the ion density. A relation was found between the minimum electric field needed to suppress disorder-induced heating and the beam current. This relation was used to calculate the amount of chromatic aberration of the lens system as a function of the current. Using this information, an analytical calculation was performed of the possible spot size of the ABLIS setup. It included its most important contributions, i.e., the brightness of the beam and spherical and chromatic aberration of a realistic lens system. The result showed that a spot size of 0.2 nm is possible at a current of 1 pA, compared to the 10 nm spot size possible with the LMIS. The calculation was verified with particle tracking simulations, which were in good agreement.

In order to perform laser cooling and compression, a laser is needed which is stable and can be precisely detuned from the cooling transition in rubidium. Furthermore a repump beam is needed which is tuned to a different transition. The laser system which matches these requirements was finalized in the work discussed here. A double pass acousto-optic modulator configuration was built to detune the laser frequency. Furthermore, an electro-optic modulator was added to the setup to create the repump beam.

An experimental setup was built in which the effect of laser cooling on the atomic beam can be tested with laser induced fluorescence (LIF). Simulations of the laser cooling experiment were performed, which showed it is possible to obtain a measure of the brightness of the beam directly from the LIF measurements. Furthermore, a simulation of the atoms in the collimating tube of the Knudsen cell is set up. Its results are in good agreement with earlier performed measurements and a theoretical model.

iv

Contents

Contents

Chapter 1

Introduction

The semiconductor industry has always been driven by Moore's law. Moore ascertained in 1965 that the number of components on an integrated circuit (IC) had doubled every two year over a period of seven years and predicted this trend to maintain for at least ten years [1]. His prediction was right and presently his law is still being followed, moreover it is used to set goals for the future. As a result of these goals, miniaturization is a leading theme in the semiconductor industry. The technology node, being the smallest feature size on IC's, is planned to be only 14 nm in the near future [2]. As the geometrical dimensions become smaller and smaller, physical limits will come in sight. To keep up with Moore's law at that point, 3D IC structures will be needed in which transistors are stacked vertically as well. Besides miniaturization, functional diversification also drives the industry [2]. This term encompasses the incorporation of additional functionalities such as sensors, micro-electromechanical systems (MEMS) and lab-on-a-chip. All of the processes above ask for tools that are able to image and modify the IC's at the nanometer length scale.

Focused ion beams (FIBs) are very suitable to fulfill these tasks. A FIB is an apparatus capable of producing very intense ion beams with a small beam waist. This enables them to image as well as modify structures at nanometer length scales. Figure 1.1 shows the three main application processes of FIBs. Imaging with a FIB works along the same principles as a scanning electron microscope (SEM). The ion beam is scanned over the surface and secondary electrons or ions are detected with a multichannel plate detector (MCP). The advantage of a FIB over a SEM is the much shorter De Broglie wavelength of ions and therefore in the limit a higher resolution. Milling is the process of sputtering and redepositing material from a substrate. Due to the high energy of incoming ions, substrate bonds are broken and material is removed. An other application is ion beam induced deposition, in which a precursor gas is brought to the vicinity of a surface which is scanned by an ion beam. Only at the illuminated part of the surface deposition then takes place.

Focused ion beams are used in the semiconductor industry for a wide range of applications, including direct patterning, photomask repairing, circuit diagnostics, circuit microsurgery and failure analysis [3]. Other applications are found in materials science, such as transmission electron microscope (TEM) specimen preparation [4]. Since the length scale in all of these applications becomes smaller there will be a strong demand for FIBs with a higher resolution in the near future.

1.1 FIB figures of merit

Before different sources for FIB instruments are discussed some figures of merit are introduced. The quality of a charged particle beam is usually expressed in terms of the brightness B and the longitudinal energy spread ΔU. The brightness is defined as the current density per unit of solid angle. Since the brightness increases with the beam energy U, a more useful
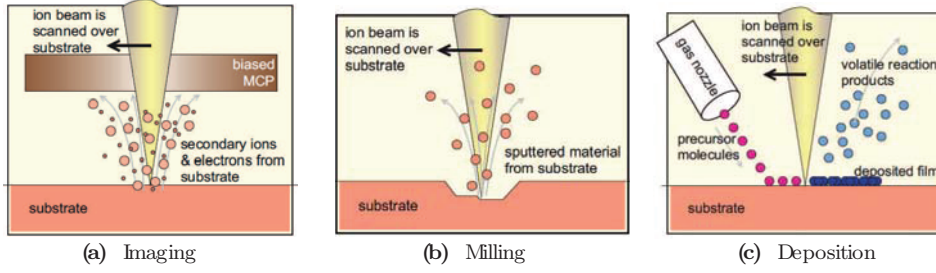
(a) Imaging   (b) Milling   (c) Deposition

Figure 1.1 The three main applications of FIB's: (a) Imaging, (b) Milling, (c) Deposition. The figure is taken from [5].

figure of merit is the reduced brightness B_r which is the brightness per unit of energy. In terms of beam parameters the reduced brightness can be written as

$$B_r = \frac{I}{4\pi^2 \epsilon_r^x \epsilon_r^y}, \tag{1.1}$$

in which I represents the beam current and ϵ_r^x and ϵ_r^y are the reduced emittances in the x- and y-direction respectively. These reduced emittances are defined by

$$\epsilon_r^i = \sqrt{\frac{m}{2}\left(\langle i^2 \rangle \langle v_i^2 \rangle - \langle iv_i \rangle^2\right)}, \tag{1.2}$$

in which m is the mass of the ions and $\langle ... \rangle$ denotes averaging over all particles. For a thermal source the brightness can also be written as [6]

$$B_r = \frac{eJ}{\pi k_b T}, \tag{1.3}$$

in which e is the elementary charge, J is the current density, k_b is Boltzmann's constant and T is the transverse source temperature. This equation reveals that both increasing the current density and decreasing the source temperature lead to a higher brightness.

According to Liouville's theorem the emittance, thus also the brightness, of a charged particle beam is a conserved quantity. If a perfect lens, lacking of any aberrations, would be used, the value of the brightness would determine the minimum achievable spot size together with the angular spread of the ions. A larger angular spread will lead to a smaller spot size as can be shown using equations 1.1 and 1.2 (see chapter 3). However, the lens system focusing the beam will never be perfect and spherical and chromatic aberration will play a role. Both of these aberrations are smaller for a smaller transverse beam size at the lens. Since this beam size also determines the angular spread after the lens, there will be an optimum angular spread leading to the smallest spot size. At what angle this will be, depends among other influences on the energy spread of the beam, since it determines the amount of chromatic aberration of the lens. For a chromatic aberration limited beam, in which spherical aberration is much smaller than chromatic aberration,

$$d \propto \left(\frac{I\sigma_U^2}{B_r}\right)^{\frac{1}{4}}, \tag{1.4}$$

in which d is the smallest achievable spot size and σ_U is the RMS energy spread. This equation shows why the brightness and energy spread are indicators for the quality of a charged particle beam. For a given current, the smallest spot size is reached with a beam which has an as large as possible brightness and an as small as possible energy spread.

1.2   Existing ion sources for FIBs

The source most often used in commercial FIB instruments is the Ga^+ Liquid Metal Ion Source (LMIS) [7]. In this type of source the ions are produced from liquid metal which is present on the tip of a needle. By applying a large electric field between the needle and an extraction electrode nearby, the liquid metal is shaped into a cone of which the tip can become as small as a few nm. Due to the extremely high electric field near the tip, field evaporation and ionization will take place. The atoms in the tip are ionized after which they are accelerated towards the extraction electrode. The resulting ion beam can then enter a FIB lens column containing the optics to focus the beam. Because of the extremely small tip from which the current is extracted, the source current density of a LMIS is of the order of 10 Acm^{-2} [8]. In such high current density beams Coulomb interaction will play an important role in determining the beams reduced brightness and energy spread. Illustrative for this Coulomb interaction is the fact that the virtual source size of the LMIS is an order of magnitude larger than its actual size, due to the trajectory displacement induced by stochastic Coulomb interaction [9]. The reduced brightness of the Ga^+ LMIS can be of the order of 10^6 A $m^{-2}sr^{-1}eV^{-1}$, while the RMS energy spread is at least 2.1 eV [10]. The latter limits the resolution of a LMIS FIB to $\approx$10 nm [7]. Another disadvantage of the LMIS is the lack of good alternatives to gallium, which has the unbeatable combination of a high surface tension and low vapor pressure.

An alternative to the LMIS is the so called Gas Field Ionization Source (GFIS), which has made great advances in the recent past. The GFIS is similar to the LMIS in the sense that it is also based on the presence of a very high electric field near the tip of a metal needle. Near this tip, gas phase atoms are ionized and accelerated away. The emitting part of the tip only consists of three atoms which increases the brightness profoundly compared to the LMIS. Currently the GFIS has been successfully constructed using helium [11] and neon [12]. The brightness is estimated at $2 \cdot 10^9$ $Am^{-2}sr^{-1}eV^{-1}$, while the energy spread is less than 1 eV [11]. This makes the GFIS an excellent choice for ion microscopy. The helium ion microscope is commercially available with a resolution of 0.5 nm [13]. The major disadvantage of the GFIS compared to other FIB sources is that currently only operation with light ions (helium and neon) is possible. Light ions do not only have a low sputter yield (number of atoms sputtered per incident ion), but also induce subsurface damage due to their large penetration depth [14]. This makes the GFIS an unattractive candidate for milling purposes.

Next to the commercially available GFIS and LMIS FIBs there are some sources which are being or have been investigated on a lab scale. Jun et al. are currently investigating the possibility of using a miniaturized gas chamber in combination with an electron gun to create an ion beam with an estimated reduced brightness of 10^7 $Am^{-2}sr^{-1}eV^{-1}$ [15]. This source, as well as the sources mentioned in the previous paragraphs, achieves its high brightness due to the fact that the beam is created from a very small source area. An other point of view will be to create the ions from cold atoms to reduce the temperature of the created ions. This principle is the basis of the ultracold ion source (UCIS) which has been investigated at the Coherence and Quantum Technology group of the Eindhoven University of Technology [16]. Before this source is explained in more detail, some elementary theory of laser cooling and trapping is treated since it plays an important role.

1.3   Magneto-optical trapping

Magneto-optical trapping is based on the interaction between light and matter. This interaction can take place when the frequency of the light field is very close to an electronic transition in the atom. In such a transition an electron is excited from a ground state to an excited state. The interaction is strongest when the difference in energy between the two states is equal to the energy of a photon of the light field.

Table 1.1 A summary of the quantum numbers and their selection rules. σ^+/σ^- light denotes right/left handed circularly polarized light

	Symbol	Selection rule
Principal quantum number	n	-
Orbital electronic angular momentum	L	$\Delta L = 0, \pm 1$
Intrinsic electronic angular momentum (spin)	S	$\Delta S = 0$
Total electronic angular momentum	J	$\Delta J = 0, \pm 1$
Intrinsic nuclear angular momentum	I	$\Delta I = 0$
Total atomic angular momentum	F	$\Delta F = 0, \pm 1$
Magnetic quantum number	M_F	linearly polarized light: $\Delta M_F = 0$ σ^+ light: $\Delta M_F = +1$ σ^- light: $\Delta M_F = -1$

Spectroscopic notation and selection rules

A common way of describing the energy levels in an atom is with the so called Russel Saunders notation, which is given by $n^{2S+1}L_J\, F$. In this notation n is the principal quantum number, which determines the 'orbit' of the electron around the nucleus. The total orbital angular momentum of the electrons in the atom is represented by the quantum number L and the total intrinsic electronic angular momentum (spin) by the quantum number S. The two electronic angular momenta can couple with eachother, which leads to the total electronic angular momentum quantum number J that can have values ranging between $|L-S|$ and $|L+S|$. The degeneration of the total electronic angular momentum into these $2S+1$ states is known as the fine structure of the atom. Finally, the total electronic angular momentum can couple with the intrinsic angular momentum I of the nucleus of the atom, which leads to the total angular momentum of the atom, represented by quantum number F. Just like for the coupling between L and S, F can have values ranging between $|J-I|$ and $|J+I|$, which is called the hyperfine structure. The last quantum number introduced here is the magnetic quantum number M_F which is the projection of F along some specified quantization axis, often along the direction of an applied magnetic field, hence the name. Due to the quantum mechanical nature of the interaction between light and atoms, certain rules apply to transitions from one state to another. These selection rules are shown in table 1.1 together with a summary of the quantum numbers to which they apply.

Magneto-optical forces

The force a radiation field can exert upon an atom originates from the fact that a photon carries a momentum $\hbar k$, in which $\hbar$ is the reduced Planck's constant and k is the (magnitude of the) wave vector of the light. When an atom absorbs a photon, it experiences a momentum kick $\hbar k$ in the direction the photon was traveling. When the atom subsequently falls back to the ground state it emits a photon. Again, it experiences a momentum kick, but this time in a random direction. When many of such absorptions and spontaneous emissions happen, the momentum kick due to the random emissions will average out to zero. The momentum kicks due to absorption will not however, so the radiation field will exert a net force upon the atom. For a still standing atom, this force F_{scatt}, also referred to as the scattering force, is given by [17]

$$F_{scatt} = \hbar k \frac{\gamma}{2} \frac{s_0}{1 + s_0 + (2\delta/\gamma)^2},\qquad(1.5)$$

in which γ is the natural line width of the transition, δ is the detuning of the laser beam and s_0 is the so-called saturation parameter, which is the ratio between the intensity I of the

Table 1.2 A summary of the most important parameters for laser cooling rubidium, data is taken from [18]. *The cooling transitions are the $5^2S_{1/2}$ $F = 3 \rightarrow 5^2P_{3/2}$ $F = 4$ for ^{85}Rb and $5^2S_{1/2}$ $F = 2 \rightarrow 5^2P_{3/2}$ $F' = 3$ for ^{87}Rb. The difference in frequency between the two transitions is 1204.6 MHz.

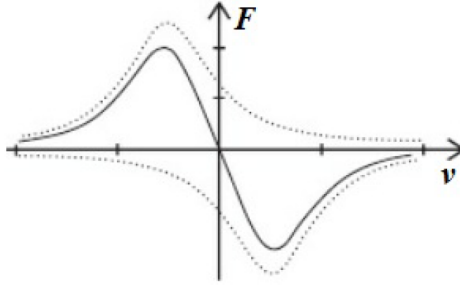| Parameters [unit]	Symbol	^{85}Rb	^{87}Rb
Mass [amu]	m	84.91	86.91
Natural abundance [%]	-	72.2	27.8
Cooling transition wavelength* [nm]	λ	780.2437	780.2462
Natural linewidth of cooling transition [MHz]	γ	5.98	5.98
Saturation intensity [W/m^2]	I_0	16.4	16.4

Figure 1.2 A plot of the scattering force of two counter propagating laser beams with a detuning of $\gamma/2$. The dotted lines represent the forces of the individual laser beams.

radiation field and the saturation intensity I_0, which is a materials constant. The detuning is the difference between the laser frequency and the frequency of the atomic transition. A summary of the most important parameters for laser cooling rubidium, the atom species used in this research, is given in table 1.2.

When an atom is moving, equation 1.5 is not valid anymore. Due to the velocity v, with which the atom is moving in the direction of the light field, it will experience a Doppler shifted frequency. Therefore the detuning in equation 1.5 must be replaced by the Doppler shifted detuning $\delta - \mathbf{k} \cdot \mathbf{v}$, so the scattering force becomes dependent on the velocity. Now imagine two counter propagating lasers that are red detuned ($\delta < 0$), which are applied to a cloud of atoms. When an atom moves in the opposite direction of one of the laser beams, the Doppler shifted laser frequency can become resonant with the transition ($\delta - \mathbf{k} \cdot \mathbf{v} = 0$). This means a force will be exerted upon the atom which is opposed to the direction in which it was traveling; the atom is decelerated. Figure 1.2 shows a schematic plot of the scattering force as a function of the velocity. As can be seen it is linear around $v = 0$. This means that slow moving atoms are decelerated and kept at $v \approx 0$ m/s; they are cooled down. They behave as if they are moving in a very viscous medium. The force has a maximum however, after which it decreases to zero again. This means that fast moving atoms will experience a small scattering force and therefore only a small deceleration. Unless they will experience this force for a very long time ($t \rightarrow \infty$), they will not be cooled down enough.

By adding a constant magnetic gradient and using circularly polarized light, it is possible to create a position dependent force F in a similar way, i.e., $F \sim -kx$, in which x is one of the transverse position coordinates constant and k is a spring constant. The atoms will then be forced towards the position where the magnetic field is zero. When this is done in three dimensions, the atoms will be cooled down and trapped to a small cloud due to the effects of the applied laser and magnetic field. Hence the name, magneto-optical trapping.

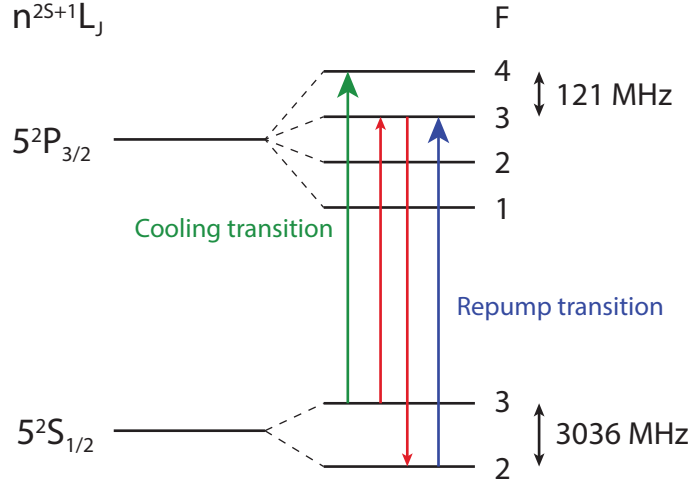***Laser cooling and trapping ^{85}Rb***

Figure 1.3 The hyperfine structure of the $5^2S_{1/2}$ and $5^2P_{3/2}$ levels in ^{85}Rb. The cooling transition is indicated in green and the repump transition in blue. One reason the repump transition is needed, is because of unwanted transitions such as those indicated in red. The repump beam excites the atoms in the unwanted ground state back to the $F = 3$ excited state. From here they can fall back to the preferred $F = 3$ ground state.

Laser cooling and trapping would be most efficient if a simple two level atom would exist, i.e., an atom without any hyperfine splitting of the ground and excited state. In that case, all electrons will either be in the only ground state or in the only excited state. The source described in this thesis will however be based on laser cooling and trapping of ^{85}Rb, which has a more complicated energy level structure. The transition used to laser cool and trap the atoms is the $5^2S_{1/2}$ $F = 3 \rightarrow 5^2P_{3/2}$ $F = 4$ transition, with a wavelength λ of 780.2437 nm. However, this is not the only possible transition with $\lambda \approx 780$ nm. Figure 1.3 shows the complete hyperfine structure of the $5^2S_{1/2}$ and $5^2P_{3/2}$ states. As can be seen there are actually two possible ground states and four possible excited states. The laser is tuned exactly to the $F = 3 \rightarrow F = 4$ transition, this means that an atom in the $F = 3$ ground state has the largest possibility to be excited to the $F = 4$ excited state. There is however a small but finite chance the atom is excited to the $F = 3$ or even $F = 2$ excited state. According to the selection rule for F (see table 1.1) it can then also decay to the $F = 2$ ground state. Furthermore, before the laser cooling and trapping starts, the rubidium will be evenly distributed among all ground states, i.e., all magnetic sub levels of the two hyperfine levels. The $F = 2$ ground states are unwanted however since the laser only has a very small probability of exciting these atoms and thus also a very small probability of cooling them. Therefore, there is a need to pump the atoms which are in the unwanted $F = 2$ ground state to an excited level from which they can decay back to the preferred ground state. This is done with an additional laser beam, known as the repump beam, which is tuned exactly to the $F = 2 \rightarrow F = 3$ transition as depicted in figure 1.3.

1.4   Cold ion sources

Now we know the basics of laser cooling and trapping we come back to the earlier mentioned UCIS, which is based on a three dimensional magneto-optical trap (MOT) of rubidium atoms. Ions are created by means of photo-ionization of the atoms in the MOT. The MOT was placed in a large electric field, which accelerates the ions away immediately after creation. The UCIS was capable of producing ion beams with a reduced brightness of $8 \cdot 10^4$ Am^{-2}sr^{-1}eV^{-1}, an
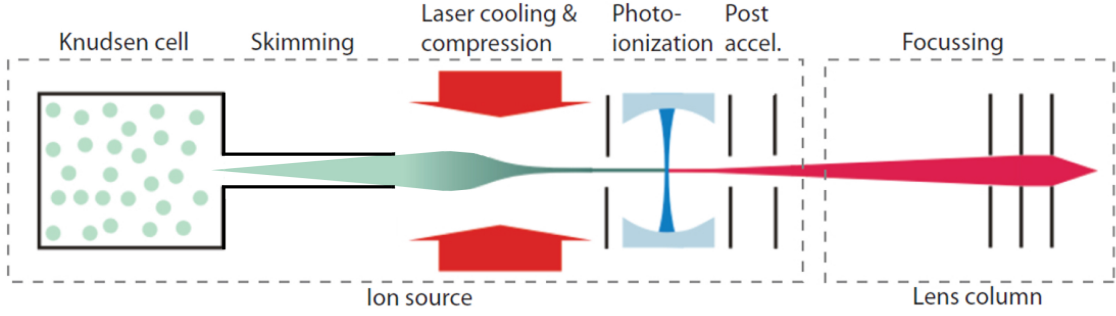
Figure 1.4 A schematic view of the ABLIS setup.

energy spread of 0.9 eV and a maximal (time-averaged) current of 13 pA [19]. The limitations to the current are mainly caused by the loading rate of the 3D MOT. Since the MOT was created from rubidium atoms in a vapor cell, the only possibility for atoms to get in the MOT is by diffusion. This diffusion process limits the maximum current to be extracted. The magneto-optical trap ion source (MOTIS), a source based on a similar concept but using lithium instead of rubidium, showed that ion beams originating from a MOT could be used for microscopy. A spot size of 27 nm was possible at a current of 0.7 pA and a beam energy of 2 keV [20].

The current limitations of the UCIS are due to the loading rate of the 3D MOT. It might be improved by adding a magneto-optical compressor, which is basically a 2D MOT, to load the 3D MOT. This increases the loading rate and therefore also the maximal current to be extracted from the MOT. These measures however increase the complexity of the source significantly. A simpler configuration was proposed by Mutsaers et al.[21]. By laser cooling and compressing an atomic beam, created in some other fashion, the limitations caused by loading of the MOT are eliminated. The idea of this so called Atomic Beam Laser-cooled Ion Source (ABLIS) is schematically shown in figure 1.4.

An atomic beam is created by using a Knudsen cell which is heated to a certain temperature (typically 100°C). Due to the low melting point of rubidium a reasonable vapor pressure is created inside the Knudsen cell, which creates a pressure gradient between the in- and outside of the cell. This pressure gradient causes the rubidium to effuse into the vacuum. A tube is connected to the opening of the Knudsen cell, so that off axis atoms are caught and sent back into the Knudsen cell to a large extent. This is done to increase the lifetime of the source. The next stage of the setup consists of a magneto-optical compressor, which is basically a 2D MOT. After this laser cooling and compression stage the brightness of the atomic beam will be increased significantly. The atoms are then photo-ionized with a second laser and immediately accelerated in a high electric field. The ions then enter a post-acceleration stage in which they are further accelerated towards the demanded energy (often 30 keV). Finally, the ions reach the final element in the beam line, which is the lens system to focus the ions to an as small as possible spot.

As explained previously the attainable spot size depends on the reduced brightness and energy spread of the beam. The energy spread of the ABLIS beam will mostly depend on the RMS width σ_L of the ionization laser beam and the acceleration field E. A particle that is created at the front of the ionization region, is created at a larger potential than a particle that is created at the back of the region, therefore it will attain more energy due to the acceleration. The energy spread of the ABLIS ion beam can, due to this effect, be written as

$$\sigma_U = eE\sigma_L. \tag{1.6}$$

Equation 1.6 shows that the energy spread and therefore chromatic aberrations will be smaller when smaller electric fields are used.

There is however another process which is influenced by the electric field strength. When the ions are created from the atomic beam, they are created at random initial positions. Associated with these random initial positions is a certain amount of potential energy. This potential energy can be transferred into kinetic energy due to Coulomb interactions, which leads to higher beam temperatures. When the initial separation between the particles is larger this process will be less important, since the initial potential energy of the particles will be lower. Therefore a large electric field will be beneficial to suppress disorder-induced heating since the ions will be removed from the ionization volume faster. This means there will be a trade off between chromatic aberration and disorder-induced heating and some optimum electric field at which the final spot size will be smallest.

Previous work at the CQT group included simulations of the laser cooling and compression stage and preliminary simulations of the disorder-induced heating showing that a reduced brightness of $2 \cdot 10^7$ Am^{-2}sr^{-1}eV^{-1} is possible at currents up till about 20 pA [22]. At higher currents, disorder-induced heating becomes important, which lowers the brightness. Concerning the laser system for the laser cooling and compression, a Titanium:Sapphire laser was proposed, stabilized with so called modulation transfer (MT) spectroscopy. Detuning of the laser system could be achieved by using two acousto optical modulators (AOMs), but was not yet realized. Furthermore, a Knudsen cell has been constructed which was capable of creating a usable flux of $2 \cdot 10^{10}$ s^{-1}, which is the flux within the range of velocities that can be captured with laser cooling and compression[23].

1.5 This thesis

The first part of this thesis is dedicated to further investigations of the performance limits of the ABLIS setup. First of all disorder-induced heating is investigated in chapter 2. An analytical model explaining the effects in certain parameter regimes is created and particle tracking simulations are performed to study the effects in more detail. It will lead to constraints with regard to the electric field to suppress disorder-induced heating.

Since the effect of the electric field on the disorder-induced heating is then known, we can combine this knowledge with theory about chromatic aberration to find an optimum electric field, which eventually leads to the smallest spot size. In order to get a realistic value of this spot size all contributions to the spot size are taken into account, i.e., the brightness of the beam and chromatic and spherical aberration of the lens column that will be used in the future.

The third chapter of this thesis describes experimental work that has been performed to extend the laser system. A new method is described which can be used to accurately set the detuning. Furthermore, the repump beam is added to the setup by making use of a so called electro-optic modulator (EOM). This will finalize the laser system so that laser cooling and trapping experiments can be performed in the future.

The fourth chapter will describe the experimental setup that has been built in the lab in order to perform laser cooling experiments. Simulations are performed of the collimating tube of the Knudsen cell and the laser cooling and compression stage, to test whether the laser cooling of the beam will be visible with laser induced fluorescence (LIF) measurements. The simulations of the tube are furthermore used to better understand some measurements that have been performed in previous work.

Chapter 2

Statistical Coulomb interaction in charged particle beams

This chapter deals with statistical Coulomb interactions in the ABLIS setup. These interactions are a fundamental bottleneck which limits the spot size of a focused ion beam. The chapter is separated in a theoretical part, describing the effects in an analytical manner and a numerical part in which the results of particle tracing simulations are discussed. These simulations are performed to check the validity of the analytical theory and to investigate the effects in regimes for which it is known that the theory is not valid.

2.1 Theory

2.1.1 Introduction

Coulomb forces between the charged particles can be divided in two separate effects: the space charge effect and statistical effects. Understanding the difference between these two is key to understanding the problems of Coulomb interactions in a focused ion beam. The space charge effect takes into account the smoothed out average force of all particles, while the statistical part takes into account all granularity effects.

The smoothed-out space charge force that an off-axis particle experiences, accelerates this particle away from the axis. The magnitude of this acceleration is proportional to the transverse position of the particle. This proportionality creates a correlation between the transverse velocities and positions. Such a correlation can however be undone with a positive lens [24], in which the focusing force is also proportional to the transverse position. Therefore the space charge effect does not change the brightness of the beam. The effect of space charge acceleration is illustrated in a phase space plot in figure 2.1.

Statistical Coulomb effects can be subdivided in two categories: relaxation of kinetic energy and relaxation of potential energy. Relaxation of kinetic energy can happen when the velocity distribution of the beam is anisotropic, i.e., when the temperature in one direction is different from the temperature in other directions. When this happens the energy present in the random motion in one direction can be transferred to the other directions due to Coulomb collisions. An anisotropic velocity distribution can be caused for instance by acceleration of the particles. As will be explained in section 2.2.3, acceleration decreases the temperature in the longitudinal direction. Therefore the kinetic energy present in the 'hotter' transverse direction will be transferred to the 'colder' longitudinal direction, which increases the longitudinal energy spread. This is known as the Boersch effect [25]. However, in the ABLIS setup the conditions are different since the ion beam will be created from a laser cooled atom beam so that the transverse temperature will only be a few hundred μK. The longitudinal energy spread will be significant however and the finite size of the ionization laser beam will further
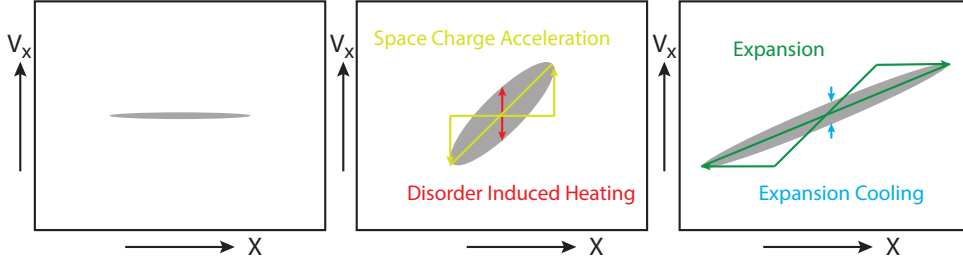
Figure 2.1 Schematic overview of the different processes happening in phase space. Left: the initial phase space volume of the beam. Middle: the phase space volume after space charge acceleration (indicated in green) and disorder-induced heating(indicated in red) have taken place, the phase space volume of the beam has become larger, i.e. the brightness of the beam has decreased. Right: the phase space volume after expansion of the beam (indicated in green), which cools the beam down (indicated in blue), while the brightness remains constant.

increase it as was explained with equation 1.6. Therefore the transverse temperature will be much smaller then the longitudinal temperature and the opposite of the Boersch effect can occur: a transition of the kinetic energy from the longitudinal to the transverse direction. Since the acceleration decreases the longitudinal temperature, this effect will however be very minor as will be shown in section 2.2.4.

The other statistical Coulomb effect is relaxation of potential energy, also known as disorder-induced heating. In the ABLIS setup, the ions are created by photo-ionization of an atom beam. Therefore they are created at random initial positions, so the Coulomb interaction forces associated with these positions will also point in random directions and will have random magnitudes. In other words, a certain amount of potential energy is created which will relax into thermal kinetic energy. As shown in figure 2.1, disorder-induced heating will decrease the phase space density of the beam. The ion density in the ABLIS ion beam will be very high. Therefore the effect of disorder-induced heating will be severely limiting the brightness, especially at higher currents [21]. At low currents the beam will be in the so called pencil beam regime. In this regime the transverse size of the beam is much smaller than the average longitudinal separation between ions in the beam. Therefore all interaction forces will more or less be pointing in the longitudinal direction and the transverse temperature of the beam will be unaffected. The other extreme case is when the beam is in the extended regime (at high currents) in which the transverse size of the beam is much larger than the longitudinal separation. The two regimes are discussed more thoroughly in section 2.2.2.

The first two effects shown in figure 2.1 are already mentioned. The third process shown, is the expansion of the ion beam and the cooling associated with this expansion. The positions of the particles become correlated to the velocities. Since the spread in positions becomes larger and the phase space density remains constant according Liouville's theorem, the local spread in velocities will become smaller, i.e., the beam cools down. However, the brigtness of the beam is not affected in this process.

One of the goals of this research is to find a model which describes the statistical Coulomb effects in the ion beam accurately, especially the dependency of the velocity distribution of the ions on experimental parameters such as the electric field strength and the current density. In order to do so, models which have been used in the past for the same purpose, are tested for their applicability to the ABLIS setup.

Fokker Planck approach

A method which has proven to be successful in describing statistical Coulomb effects in

the past is the so called Fokker Planck approach [26]. The Fokker Planck approach has its origin in the field of plasma physics and treats the statistical effects as a diffusion process in velocity space. In general the evolution of the distribution function $f(\boldsymbol{r}, \boldsymbol{v}, t)$ of a particle beam, which is basically a very specific type of non-neutral plasma, can be described with the Boltzmann equation [27]

$$\frac{\mathrm{d}f}{\mathrm{d}t} = \frac{\partial f}{\partial t} + \boldsymbol{v} \cdot \nabla f + \boldsymbol{a} \cdot \nabla_v f = \left(\frac{\delta f}{\delta t}\right)_{coll}, \tag{2.1}$$

in which ∇_v is a gradient operator in terms of the velocity components instead of position components. The collisional term $\left(\frac{\delta f}{\delta t}\right)_{coll}$ takes into account all effects due to collisions between particles. In the Fokker Planck approach this term is calculated as

$$\left(\frac{\delta f}{\delta t}\right)_{coll} = \beta \nabla_v \cdot \boldsymbol{v} f + D \nabla_v^2 f. \tag{2.2}$$

in which the coefficients β and D are the coefficient of dynamical friction and the diffusion constant, which can be expressed in terms of macroscopic parameters [28]. This specific collision term is only valid under a strict assumption. At the moment two ions collide they experience an intense but short acceleration, in other words they undergo a velocity jump. Equation 2.2 is only valid provided that these velocity jumps are small compared to the thermal velocity spread. This condition is met if the so called Coulomb logarithm is much larger than one [28]. For non-neutralized systems such as an ion beam, the Coulomb logarithm can be expressed as

$$\Lambda_C \approx \ln\left(\frac{\frac{3}{2}\mathrm{k_b T}}{\frac{e^2}{4\pi\epsilon_0}\mathrm{n}^{\frac{1}{3}}}\right), \tag{2.3}$$

in which $\frac{3}{2}k_b T$ can be recognized as the average random kinetic energy and $\frac{e^2}{4\pi\epsilon_0} n^{\frac{1}{3}}$ as the average potential energy. For the Coulomb logarithm to be larger than one, the random kinetic energy must be much larger than the potential energy. In normal plasmas this condition can be met easily. In the ABLIS setup however, the ion beam is created from a laser cooled atom beam, meaning that the temperature is very low and thus the Coulomb logarithm smaller than one. Therefore the Fokker Planck approach is not suited to describe the statistical Coulomb effects in the ABLIS setup. One can conclude that the Coulomb collisions in the ABLIS setup are incomplete and strong, while the Fokker Planck approach is designed to describe the collisional effects for the case of complete and weak collisions. In other words it is suited to describe relaxation of kinetic energy, but not to describe relaxation of potential energy.

Ultracold plasmas

Disorder-induced heating has been investigated a lot in the context of ultracold plasmas [29]. In such systems thermalisation will lead to kinetic energies $k_b T_i$ of the order of the initial potential energy,

$$k_b T_i \approx \frac{e^2}{4\pi\epsilon_0 a}, \tag{2.4}$$

in which a represents the Wigner Seitz radius which is given by

$$a = \left(\frac{3}{4\pi n}\right)^{\frac{1}{3}}. \tag{2.5}$$

The final temperature T_i is reached on a time scale of the order of the inverse plasma frequency ω_p^{-1}, given by

$$\omega_p^{-1} = \sqrt{\frac{m\epsilon_0}{ne^2}}. \tag{2.6}$$

Generally spoken, an ultracold plasma is created in the ABLIS setup. However, the ions and electrons are accelerated out of the ultracold plasma immediately after creation. This acceleration lowers the ion density in the beam. The disordered induced heating process is therefore slowed down and the equilibrium temperature will be lower. The equations above do not give a good description of this acceleration process, but they can be used to estimate the temperature to which the plasma would heat up and the time scale at which this would happen if no acceleration would take place. To calculate these values the initial ion density in the ABLIS setup is needed which is given by

$$n = \frac{\phi}{v_a}, \tag{2.7}$$

in which ϕ represents the flux density reached after the cooling and compression stage and v_a is the longitudinal velocity of the atoms. Typical values of these quantities are $\phi = 5 \cdot 10^{19}$ $\text{m}^{-2}\text{s}^{-1}$ and $v_a = 314 \text{ ms}^{-1}$, leading to a density of $1.6 \cdot 10^{17} \text{ m}^{-3}$. Using this value for the density in equations 2.4-2.6 leads to an equilibrium ion temperature of 15 K, which is reached in 18 ns, compared to the sub mK temperatures reached after the laser cooling. These values indicate the necessity of accelerating the ions immediately. Ionizing the atoms outside the acceleration stage to prevent a large energy spread is not possible since disorder-induced heating heats up the ion beam too fast.

In the remainder of this theoretical part, an attempt is made to find equations which analytically describe the disorder-induced heating process. The basis of the solution to this problem is found in the extended two particle approximation, by Jansen et al. [30], which is extensively discussed in sections 2.1.2 and 2.1.3. In the following section general aspects of the so called Holtsmark distribution are described, since it plays an important role in the theory. In sections 2.1.5 and 2.1.6 the extended two particle model is applied to the ABLIS setup and equations are found which describe the evolution of the transverse velocity distribution accurately, but under a few assumptions.

2.1.2 The extended two-particle approximation

Since charged particles interact with each other, their trajectories in six dimensional phase space will undergo changes in the course of time with respect to their unperturbed trajectories. The probability that a particle will undergo such a change, referred to as a displacement from now on, is determined by the so called displacement distribution. This section deals with the mathematical framework of the calculation of this displacement distribution as was described by Van Leeuwen and Jansen [30] and more elaborately in Jansen's PhD-thesis [28].

In general the problem of finding the displacement distribution can be split up in a dynamical and a statistical part [24]. The dynamical part is to calculate the displacement $\Delta\boldsymbol{\eta}$ induced to the trajectory of a test particle by a certain environment of field particles and the statistical part is to calculate the probability that such an environment occurs.

The coordinates $\boldsymbol{\xi} = (x, y, z, v_x, v_y, v_z)$ of the field particles are measured with respect to the coordinates of the test particle. In other words, the coordinate system is traveling along with the test particle. This means the position of the origin $z(t)$ of this moving coordinate system is a function of time t given by

$$z(t) = \frac{eE_a}{2m}t^2 + v_a t, \tag{2.8}$$

in which E_a is the electric field strength in the acceleration stage and v_a is the velocity of the test particle before entering the acceleration stage. Equation 2.8 can be solved for the time as a function of the position, leading to

$$t(z) = \frac{m}{eE_a}\left(\sqrt{v_a^2 + \frac{2eE_a z}{m}} - v_a\right). \tag{2.9}$$

In a beam consisting of N particles the test particle will interact with N-1 field particles. Therefore the displacement of the test particle is in general a function of all $6(N\text{-}1)$ coordinates $\boldsymbol{\xi}_1...\boldsymbol{\xi}_{N-1}$ of the field particles. In general the displacement can be written in terms of an integral over time. The velocity displacement $\Delta\boldsymbol{v}$ can for example be written as

$$\Delta\boldsymbol{v}\left(t\right) = \int_0^t \frac{1}{m}\boldsymbol{F}\left(\boldsymbol{\xi}_1\left(t'\right)...\boldsymbol{\xi}_{N-1}\left(t'\right)\right)\mathrm{dt}', \qquad (2.10)$$

in which $\boldsymbol{F}\left(\boldsymbol{\xi}_1\left(t\right)...\boldsymbol{\xi}_{N-1}\left(t\right)\right)$ is the force acting on the particle at time t and m is the particle's mass. Solving the dynamical part of the problem is a very complicated task since the force acting on the particles on a certain time t is determined by the relative coordinates at that time. However these relative coordinates are influenced by the force acting on the particles prior to that time t. Due to this coupling of the force and the coordinates, simplifying approximations have to be made in order to solve the problem. One of these approximations is the first order perturbation approximation, which is the subject of sections 2.1.5 and 2.1.6.

The other part of the problem is the statistical part of finding the probability $P\left(\boldsymbol{\xi}_1...\boldsymbol{\xi}_{N-1}\right)$ that the particles are in the configuration $\boldsymbol{\xi}_1...\boldsymbol{\xi}_{N-1}$ at t=0. From this probability the displacement distribution $\rho\left(\Delta\boldsymbol{\eta}\right)$ can be calculated with

$$\rho\left(\Delta\boldsymbol{\eta}\right) = \int P\left(\boldsymbol{\xi}_1...\boldsymbol{\xi}_{N-1}\right)\delta\left(\Delta\boldsymbol{\eta} - \Delta\boldsymbol{\eta}\left(\boldsymbol{\xi}_1...\boldsymbol{\xi}_{N-1}\right)\right)\mathrm{d}\boldsymbol{\xi}_1...\mathrm{d}\boldsymbol{\xi}_{N-1}, \qquad (2.11)$$

in which $\delta\left(\boldsymbol{x}\right)$ is the n dimensional delta-Dirac function, with n the dimension of $\Delta\boldsymbol{\eta}$.

In order to find ρ, another simplifying approximation has to be used, namely that the particles can be treated as independent statistical quantities. The probability $P\left(\boldsymbol{\xi}_1...\boldsymbol{\xi}_{N-1}\right)$ can then be written as

$$P\left(\boldsymbol{\xi}_1...\boldsymbol{\xi}_{N-1}\right) = \prod_{i=1}^{N-1} P_2\left(\boldsymbol{\xi}_i\right), \qquad (2.12)$$

in which $P_2\left(\boldsymbol{\xi}_i\right)$ denotes the probability that the ith field particle has coordinates $\boldsymbol{\xi}_i$. This assumption implies that no correlations exist between the coordinates of different particles, which is not true in general. Correlations can be divided in correlations caused by the source and correlations due to screening effects. In the ABLIS setup, ions are produced by photo-ionization of an atom beam. Since atoms only weakly interact with each other, it is reasonable to assume that no correlations are present between the coordinates of individual ions due to the source. Secondly, the goal of this research is to study the heating of the beam immediately after ionization. Therefore the ions have no time to re-arrange themselves, so it is a valid assumptions that no correlations exist between the ion positions at all, i.e., also screening effects do not play a role.

Equation 2.12 gives an expression for the N particle probability in terms of the two particle probabilities. An expression for the N particle displacement in terms of the two particle displacements can be found by making use of the fact that the force on the particle is equal to the sum of the individual forces. Therefore the displacement of the particle can be written as the sum of the two particle displacements $\Delta\boldsymbol{\eta}_2$,

$$\Delta\boldsymbol{\eta}\left(\boldsymbol{\xi}_1...\boldsymbol{\xi}_{N-1}\right) = \sum_{i=1}^{N-1} \Delta\boldsymbol{\eta}_2\left(\boldsymbol{\xi}_i\right). \qquad (2.13)$$

When equations 2.11-2.13 are now combined, a new expression for the displacement distribution can be found. After a few calculus operations [28], this results in

$$\rho\left(\Delta\boldsymbol{\eta}\right) = \frac{1}{\left(2\pi\right)^n}\int e^{i\boldsymbol{k}\cdot\Delta\boldsymbol{\eta} - \lambda p(\boldsymbol{k})}\mathrm{d}\boldsymbol{k}, \qquad (2.14)$$

13

in which λ is the linear particle density and $\boldsymbol{k}$ is an n-dimensional vector which is introduced due to the fact that the Dirac-delta function in equation 2.11 can be written as

$$\delta\left(\boldsymbol{x}\right) = \frac{1}{(2\pi)^n} \int e^{i\boldsymbol{k}\cdot\boldsymbol{x}} \mathrm{d}\boldsymbol{k}. \tag{2.15}$$

The function $p\left(\boldsymbol{k}\right)$ in equation 2.14 is given by

$$p\left(\boldsymbol{k}\right) = L \int P_2\left(\boldsymbol{\xi}\right) \left(1 - e^{-i\boldsymbol{k}\cdot\Delta\boldsymbol{\eta}_2(\boldsymbol{\xi})}\right) \mathrm{d}\boldsymbol{\xi}, \tag{2.16}$$

in which L represents the length of the beam segment under consideration. This L has entered the analysis on the basis of normalization arguments.

The last step is to introduce the two particle displacement distribution $\rho_2\left(\Delta\boldsymbol{\eta}\right)$, which gives the probability that a displacement $\Delta\boldsymbol{\eta}$ is caused when the beam would only contain a single field particle. The two particle distribution function is given by

$$\rho_2\left(\Delta\boldsymbol{\eta}\right) = \int P_2\left(\boldsymbol{\xi}\right) \delta\left(\Delta\boldsymbol{\eta} - \Delta\boldsymbol{\eta}_2\left(\boldsymbol{\xi}\right)\right) \mathrm{d}\boldsymbol{\xi}. \tag{2.17}$$

Finally, the function $p\left(\boldsymbol{k}\right)$ can be written in terms of $\rho_2\left(\Delta\boldsymbol{\eta}\right)$, by making use of the properties of the Dirac-delta function, resulting in

$$p\left(\boldsymbol{k}\right) = L \int \rho_2\left(\Delta\boldsymbol{\eta}\right) \left(1 - e^{-i\boldsymbol{k}\cdot\Delta\boldsymbol{\eta}}\right) \mathrm{d}\Delta\boldsymbol{\eta}. \tag{2.18}$$

Equations 2.14, 2.17 and 2.18, derived along the lines of [28], are the main result of this section. The convenience of these formulas is that simple two particle statistics and dynamics can be used to find the displacement distribution of the N-particle problem. The first step is to calculate the two particle displacement distribution with equation 2.17. Next, the N-particle displacement distribution can be calculated with the aid of equations 2.14 and 2.18.

2.1.3 Force distribution in an infinitely large cloud of charged particles

The analysis in section 2.1.2 was done in terms of the displacement of the test particle. However, all the reasoning is also valid for the force $\boldsymbol{F}$ acting on the test particle. Therefore, by replacing $\Delta\boldsymbol{\eta}$ with $\boldsymbol{F}$ in equations 2.14, 2.17 and 2.18, a scheme is obtained for finding the force distribution. To make this job a little easier, two more assumptions are made: the beam is assumed to be uniformly distributed with a density n and the beam diameter is assumed to be infinitely large and equal to the length L of the beam line, which is thus also assumed to be infinitely long. With these assumptions the beam can be considered as an infinitely large spherical cloud of particles. For the calculation in this section again the reasoning of [28] is used.

The first step in finding the force distribution $\rho\left(\boldsymbol{F}\right)$ is to write equations 2.14, 2.17 and 2.18 in spherical coordinates. Since spherical symmetry is present it is possible to solely describe the force distribution in terms of the magnitude F. Equation 2.17 now changes to

$$\rho_2\left(F\right) = 4\pi F^2 \rho_2\left(\boldsymbol{F}\right) = \int P_2\left(\boldsymbol{\xi}\right) \delta\left(F - F_2\left(\boldsymbol{\xi}\right)\right) \mathrm{d}\boldsymbol{\xi}, \tag{2.19}$$

in which $\rho_2\left(F\right)\mathrm{d}F$ denotes the probability that a force with a magnitude between F and $F + \mathrm{d}F$ is experienced by the test particle in the case that only a single field particle is present in the beam and $\delta\left(x\right)$ is the one dimensional delta function. Making use of the first equality in equation 2.19, equation 2.18 can be written as

$$p\left(k\right) = L \int_0^\infty \int_0^{2\pi} \int_0^\pi \frac{\rho_2\left(F\right)}{4\pi F^2} \left(1 - e^{-ikF\cos(\phi)}\right) \sin\left(\phi\right) F^2 \mathrm{d}\phi\mathrm{d}\theta\mathrm{d}F. \tag{2.20}$$

14

Solving the angular integrals leads to

$$p(k) = L \int_0^\infty \rho_2(F) \left(1 - \frac{\sin(kF)}{kF}\right) \mathrm{d}F. \tag{2.21}$$

Finally, equation 2.14 can be transformed to

$$
\begin{aligned}
\rho(F) &= 4\pi F^2 \rho(\boldsymbol{F}) \\
&= \frac{F^2}{2\pi^2} \int_0^\infty \int_0^{2\pi} \int_0^\pi e^{ikF\cos(\phi) - \lambda p(k)} \sin(\phi) \, k^2 \mathrm{d}\phi \mathrm{d}\theta \mathrm{d}k \\
&= \frac{2F}{\pi} \int_0^\infty e^{-\lambda p(k)} \sin(kF) \, k \mathrm{d}k.
\end{aligned}
\tag{2.22}
$$

The next step is to apply equations 2.19, 2.21 and 2.22 to the uniform cloud of particles. Since the density in the cloud is uniform, the two particle probability is constant and given by

$$P_2(\boldsymbol{\xi}) = \frac{3}{4\pi L^3}. \tag{2.23}$$

The two particle force distribution function is now found by substituting this expression in equation 2.19, resulting in

$$\rho_2(F) = \int_0^\infty \frac{3}{4\pi L^3} \delta\left(F - \frac{C_0}{r^2}\right) 4\pi r^2 \mathrm{d}r, \tag{2.24}$$

in which $C_0 = \frac{e^2}{4\pi\epsilon_0}$, with ϵ_0 the vacuum permittivity. This integral is solved by making the substitution $x = \frac{C_0}{r^2}$, which leads to

$$
\begin{aligned}
\rho_2(F) &= \int_0^\infty \frac{3C_0}{xL^3} \delta(F - x) \sqrt{\frac{C_0}{4x^3}} \mathrm{d}x \\
&= \frac{3C_0^{\frac{3}{2}}}{2L^3 F^{\frac{5}{2}}}.
\end{aligned}
\tag{2.25}
$$

This two particle force distribution is substituted in equation 2.21. The resulting integral can be solved with integration by parts, which leads to

$$\lambda p(k) = \frac{\lambda \left(8\pi C_0^3\right)^{\frac{1}{2}} k^{\frac{3}{2}}}{5L^2}. \tag{2.26}$$

The expression in equation 2.26 does not become zero for $L \to \infty$, since $\lambda \propto L^2$ for $L \to \infty$. This can be understood by considering the total number of particles N in the beam, which is for $L \to \infty$ equal to

$$N = \lambda L = \frac{4}{3}\pi L^3 n, \tag{2.27}$$

therefore

$$\frac{\lambda}{L^2} = \frac{4}{3}\pi n. \tag{2.28}$$

Combining equations 2.26 and 2.28 leads to

$$\lambda p(k) = (F_n k)^{\frac{3}{2}}, \tag{2.29}$$

where F_n is the so called normalized field strength which is given by

$$F_n = \left(\frac{4n}{15}\right)^{\frac{2}{3}} 2\pi C_0. \tag{2.30}$$

Finally, substitution of 2.29 in equation 2.22 leads to the desired force distribution function, which is given by

$$\rho(F) = \frac{2F}{\pi} \int_0^\infty e^{-(F_n k)^{\frac{3}{2}}} \sin(kF)\, k \mathrm{d}k. \tag{2.31}$$

The distribution of equation 2.31 is a so called Holtsmark distribution, named after the first person to derive it. Characteristic for the Holtsmark distribution is the $\frac{3}{2}$ power dependency. The value of F_n determines the width of the distribution.

2.1.4 General aspects of the Holtsmark distribution

Equation 2.31 shows that the force acting on a particle in an infinitely large cloud of charged particles is distributed according to a Holtsmark distribution. The Holtsmark distribution is a specific type of the more general symmetric stable distributions $\rho(x)$ which can be written as [31]

$$\rho(x) = \frac{1}{2\pi} \int_{-\infty}^\infty \phi(k)\, e^{-ikx} \mathrm{d}k \tag{2.32}$$

in which $\phi(k)$ is the so called characteristic function, defined as

$$\phi(k) = e^{ik\mu - \left| \frac{\sigma}{\sqrt{2}} k \right|^\alpha} \tag{2.33}$$

with μ the average of the quantity x, σ a parameter related to the width of the distribution and α a parameter defining the shape of the distribution. Comparison of these equations with equation 2.31 shows that for the Holtsmark distribution $\alpha = \frac{3}{2}$.

For the Holtsmark distribution, the integral defined by equations 2.32 and 2.33 does not lead to a simple analytic function. However, for $\alpha = 2$ the probability distribution can be written in a very simple form. Since the Fourier transform of a product of two functions can be written as a convolution of the Fourier transforms of the individual functions [32], equation 2.32 leads to

$$\begin{aligned}
\rho_{\alpha=2}(x) &= \frac{1}{(2\pi)^2} \left(\int_{-\infty}^\infty e^{-ik(x-\mu)} \mathrm{d}k * \int_{-\infty}^\infty e^{-ikx - \frac{\sigma^2 k^2}{2}} \mathrm{d}k \right)(x) \\
&= \frac{1}{(2\pi)^2} \left(2\pi \delta(\mu - x) * \sqrt{\frac{2\pi}{\sigma^2}} e^{-\frac{x^2}{2\sigma^2}} \right)(x) \\
&= \frac{1}{\sqrt{2\pi}\sigma} e^{-\frac{(x-\mu)^2}{2\sigma^2}},
\end{aligned} \tag{2.34}$$

in which $*$ denotes a convolution.

The result of equation 2.34 is the well known Gaussian distribution. Figure 2.2 shows the difference between the Gaussian distribution and the Holtsmark distribution. The most pronounced difference between the two is the long tail of the Holtsmark distribution compared to the Gaussian. This tail is also the reason that the variance $\langle x^2 \rangle - \langle x \rangle^2$ of the Holtsmark distribution does not exist, i.e., the integral $\int_{-\infty}^\infty x^2 \rho(x)\, \mathrm{d}x$ diverges for $\alpha < 2$. Therefore there is no such thing as an RMS width of the Holtsmark distribution and other measures have to be used to specify its width, for example the parameter σ, the full width at half maximum (FWHM) or the full width of the 50 percent closest to the center of the distribution (d_{50}). Another possibility is to define the variance of part of the distribution, for example of a certain percentage closest to the center of the distribution.

As was shown in the previous sections the force distribution in the extended beam regime is a Holtsmark distribution. Analytical and numerical calculations of other regimes were done by Jansen et al. [28], who showed that $p(k)$ can often be approximated by

$$\lambda p(k) = A k^\gamma, \tag{2.35}$$

in which A is determined by experimental parameters. For $\gamma = \frac{3}{2}$ this again leads to the Holtsmark distribution. For other values of γ it leads to other types of stable distributions.
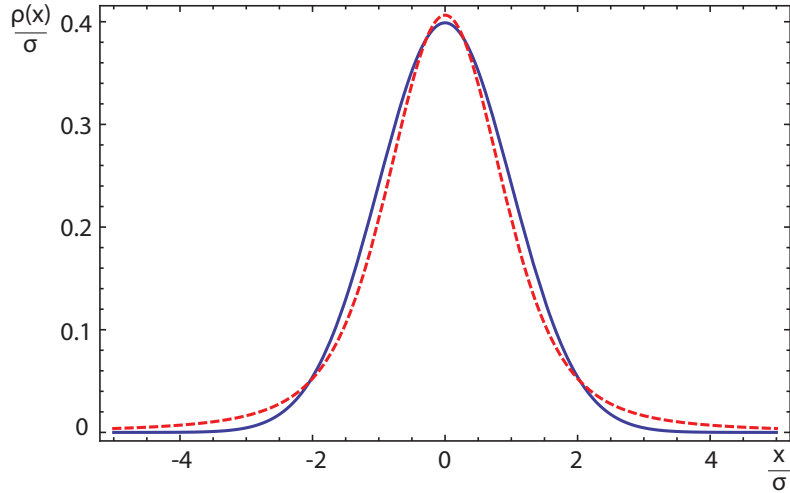
Figure 2.2 One dimensional Gaussian and Holtsmark distribution with the same scale parameter σ.

2.1.5 Force evolution upon acceleration

Section 2.1.2 and 2.1.3 described the most important equations of the extended two particle model. These equations have never been successfully applied to describe the evolution of the velocity distribution in a charged particle beam which undergoes an acceleration. This section will describe the steps to go from the force distribution of section 2.1.3 to the time dependent average transverse force. In order to do so several assumptions have to be made, which are introduced first.

In section 2.1.3 the distribution of the force acting on one of the particles in a charged particle beam was derived under the assumption of an infinitely large beam. In reality of course no such beam exists, but for beams with a large beam radius compared to the inter particle distance the error made in this approximation becomes very small. Therefore the force distribution from section 2.1.3 is valid for beams in the extended regime. As will be shown in section 2.2.2, the beam is in the extended regime for currents $\gtrsim$10 nA and larger. One can say that, for such beams, the statistical part of the problem is solved. The next step is to solve the dynamical part.

Due to the electric field in the ionization stage the particles are accelerated. This acceleration lowers the linear particle density, i.e., the separation between the particles becomes larger. Therefore the interaction force becomes smaller, but also its direction changes. The longitudinal separation becomes larger, but the transverse separation stays the same, so the direction of the interaction force changes towards the longitudinal direction.

The dynamical part of the problem is the calculation of the force evolution under the influence of acceleration of all individual particles. The way to solve the problem was actually already layed out by equations 2.14, 2.17 and 2.18. This process starts with calculating the value of $\Delta\eta_2(\xi)$, substituting it in equation 2.17 and solving the resulting integral. It is however very hard, if not impossible, to solve this integral analytically, let alone solving the integrals in 2.18 and 2.14. Therefore another method has to be found to solve the problem. The method described in this section is based on the approximation that the evolution of the interaction force may be treated as if it was produced by only a single field particle. Strictly spoken this approach is incorrect, but intuitively one expects that the many particle force evolution will not be very different from the single particle force evolution. As will be shown later when comparing the theoretical results with particle tracing simulations, this is indeed the case.

In the ABLIS setup, ions are produced by photo-ionization of a laser cooled atom beam. For the evaluation of the force evolution the assumption is made that the ionization of the test particle and its surrounding field particles take place simultaneously at time $t = 0$. Under this assumption the force exerted on the test particle at $t = 0$ is distributed according to the Holtsmark distribution of equation 2.31. From this moment forward the force acting on the test particle is correlated to the force at $t = 0$.

As mentioned earlier in section 2.1.2, the problem of finding the evolution of the force acting on the test particle is very complicated. The force depends on the positions of the field particles, but these positions depend on the force. When the heating of the particles however takes place in a very small time span, one may assume the interaction force does not change the position of the particles. In the ABLIS setup this first order perturbation model will be valid on approximately the first 1-10 mm of the acceleration. In the rest of this theoretical part this approximation is used, so the results will only be valid for the first 1-10 mm of the setup. In the simulation section of this chapter it will be investigated whether disorder-induced heating also plays a role in the remainder of the beam line.

Now that all approximation are laid out, the actual calculation can start. Assume a force with magnitude F_0 is acting on the test particle at $t = 0$. The virtual field particle from which this force is originating, lies on a sphere with a radius ρ_0 given by

$$\rho_0 = \sqrt{\frac{C_0}{F_0}}. \tag{2.36}$$

Now suppose the position vector $\boldsymbol{\rho}_0$ makes an angle θ_0 with the z-direction, see figure 2.3. Then the initial longitudinal coordinate z_0, and initial transverse coordinate r_0 are given by

$$\begin{aligned} r_0 &= \rho_0 \sin\theta_0, \\ z_0 &= \rho_0 \cos\theta_0. \end{aligned} \tag{2.37}$$

When time evolves the transverse coordinate remains constant, but the longitudinal coordinate will grow. Assume for now that the longitudinal coordinate z is given by

$$z = f(t)z_0, \tag{2.38}$$

in which $f(t)$ is a function of time, which takes into account the acceleration process. The distance between the field and test particle can now be written as

$$\rho(t) = \sqrt{(f(t)z_0)^2 + r_0^2}. \tag{2.39}$$

Using equations 2.36, 2.37 and 2.39, an equation for the transverse part of the time dependent interaction force can be derived,

$$\begin{aligned} F_r(t) &= \sin\theta(t)\frac{C_0}{\rho(t)^2} \\ &= \frac{C_0 r_0}{\rho(t)^3} \\ &= \frac{C_0\rho_0\sin\theta_0}{\left(f(t)^2\rho_0^2\cos^2\theta_0 + \rho_0^2\sin^2\theta_0\right)^{\frac{3}{2}}} \\ &= F_0\frac{\sin\theta_0}{\left(f(t)^2\cos^2\theta_0 + \sin^2\theta_0\right)^{\frac{3}{2}}}. \end{aligned} \tag{2.40}$$

Equation 2.40 shows the time evolution of the transverse component of the interaction force. This evolution is different for forces with different initial directions. To relate the
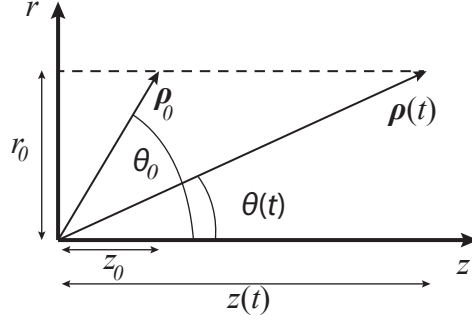
Figure 2.3 Illustration of the initial coordinates and the evolution of the coordinates. The radial part of the position vector stays the same, but by accelerating the particles, the longitudinal part of the position vector grows, thereby changing the magnitude as well as the direction of the force.

size of the initial force to the average transverse velocity displacement this force causes, one has to average over all possible initial directions. The average transverse force component is given by

$$F_{r,avg} = \frac{F_0}{4\pi} 2 \int_0^{2\pi} \int_0^{\frac{\pi}{2}} \frac{\sin^2\theta_0}{\left(f(t)^2\cos^2\theta_0 + \sin^2\theta_0\right)^{\frac{3}{2}}} \mathrm{d}\theta_0 \mathrm{d}\phi_0. \tag{2.41}$$

Before the integral in equation 2.41 can be evaluated, the function $f(t)$ has to be found which specifies the ratio of the distance between the test and field particle at time t and this distance at $t = 0$. To find this distance one cannot assume that the test and field particle are ionized simultaneously since they will then experience exactly the same acceleration and the distance between the particles will remain the same. Therefore the real ionization process has to be taken into account, in which one particle is ionized earlier than the other. In contrast to the preceding calculations, the analysis of $f(t)$ is done in the lab frame instead in the moving frame. Assume the second particle is ionized as the first particle is at a position z_0. Since the first particle is already accelerated over a distance z_0 its velocity $v_{1,0}$ is

$$v_{1,0} = \sqrt{v_a^2 + \frac{2eE_az_0}{m}}, \tag{2.42}$$

in which E_a is the accelerator electric field strength and v_a is the velocity of both particles before they are ionized. Therefore the positions $z_1(t)$ and $z_2(t)$ of the two particles are

$$z_1(t) = \frac{eE_a}{2m}t^2 + \sqrt{v_a^2 + \frac{2eE_az_0}{m}}t + z_0$$

$$z_2(t) = \frac{eE_a}{2m}t^2 + v_at \tag{2.43}$$

and the function $f(t)$ can be written as

$$f(t) = \frac{z_1(t) - z_2(t)}{z_0} = 1 + \frac{\left(\sqrt{v_a^2 + \frac{2eE_az_0}{m}} - v_a\right)t}{z_0}. \tag{2.44}$$

As can be seen $f(t)$ is a linear function of time with a slope which is dependent on the initial separation z_0. This dependence is very unpractical for further evaluation of the problem, since it makes equation 2.41 very difficult to solve. Therefore an approximation for $f(t)$ is needed which is independent of z_0. For very small values of z_0, $f(t)$ can be approximated by

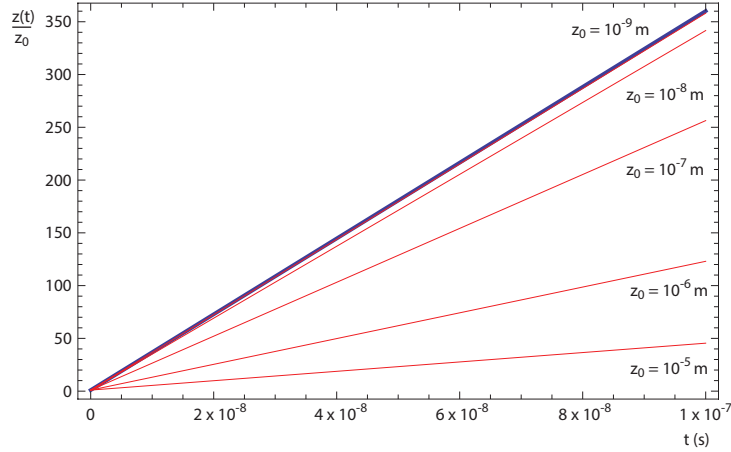$$f(t) \equiv \frac{z(t)}{z_0} \approx 1 + \frac{eE_at}{mv_a}. \tag{2.45}$$

Figure 2.4 Plots of f(t) (equation 2.44) for different values of z_0 together with a plot of the first order approximation of $f(t)$ for small z_0 (equation 2.44)

Figure 2.4 shows a plot of equation 2.45 together with plots of equation 2.44 for different values of z_0. It can be seen that for $z_0 < 10^{-8}$ m the approximation is good. In the ABLIS setup z_0 will however be of the order of micrometers and a better approximation is given by

$$f(t) \approx 1 + \frac{peE_a t}{mv_a}, \tag{2.46}$$

in which p is a factor between 0 and 1, which is found by comparison with particle tracing simulations. As will be shown in the second part of this chapter this approximation leads to satisfactory results within the investigated range of electric fields and fluxes.

Now that an expression for $f(t)$ is found, the integral of equation 2.41 can be evaluated, leading to a large and unpleasant expression containing elliptic integrals, which is not shown here. However, an approximation of this solution is

$$F_{r,avg} = \frac{1.15mv_a F_0}{(peE_a t + 2mva)}, \tag{2.47}$$

which is the main result of this section.

To check the validity of equation 2.47, the integral in equation 2.41 is solved numerically using the unsimplified $f(t)$ from equation 2.44. Figure 2.5 shows a comparison of this numerical solution with the approximation given by equation 2.47. For the numerical solution an F_0 of $\frac{1}{4\pi\epsilon_0 a_0^2}$ is used, in which a_0 is the Wigner Seitz radius. It can be concluded that the two are different, but the difference is small for $t < 10^{-8}$ s, which is also the regime in which the first order approximation is valid. In figure 2.5 the value of p in the approximated solution is the value found by comparison with particle tracking simulations (see section 2.2.3).

2.1.6 Transverse velocity distribution

The transverse velocity distribution can be found by relating the average transverse velocity v_r to the magnitude of the initial force F_0. The transverse velocity distribution can then be found with a coordinate transform of the force distribution given by equation 2.31. The relation between v_r and F_0 is found by integrating the transverse acceleration over time,
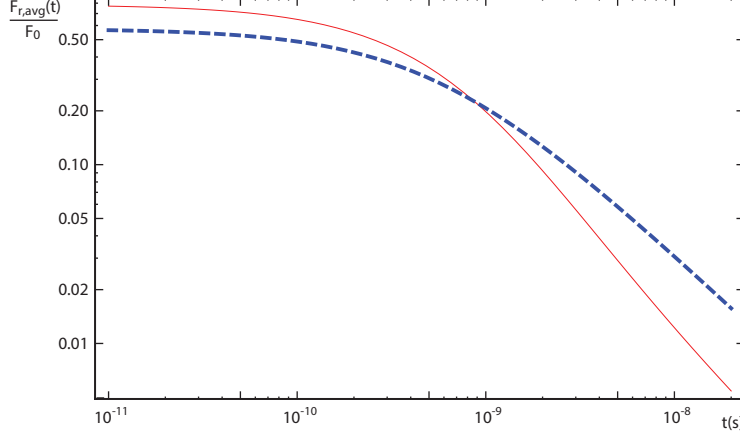
Figure 2.5 A plot of the numerical solution of equation 2.41 (solid curve) and an approximation of this solution (dashed curve), given by equation 2.47.

using equation 2.47,

$$
\begin{aligned}
v_r &= \int_0^t \frac{F_{r,avg}(t')}{m} \mathrm{d}t' \\
&= \frac{1.15 v a F_0}{p e E_a} \ln \left(1 + \frac{p e E_a t}{2 m v_a} \right) \\
&= g(t) F_0
\end{aligned}
\tag{2.48}
$$

Now the relation between v_r and F_0 is known, the transverse velocity distribution can be calculated from equation 2.31. This is done by doing the coordinate transform from F_0 to v_r as defined by equation 2.48. This transform results in

$$
\begin{aligned}
\rho(v_r) &= \frac{\mathrm{d}F}{\mathrm{d}v_r} \rho(F_0(v_r)) \\
&= \frac{2 v_r}{\pi \left(g(t) \right)^2} \int_0^\infty e^{-(F_n k)^{\frac{3}{2}}} \sin \left(k \frac{v_r}{g(t)} \right) k \mathrm{d}k
\end{aligned}
\tag{2.49}
$$

This equation reveals the the transverse velocity distribution, however one more step is needed to recognize the shape of the distribution. This step is the coordinate transform $k = g(t) k'$, which leads to

$$
\rho(v_r) = \frac{2 v_r}{\pi} \int_0^\infty e^{-\left(F_n g(t) k' \right)^{\frac{3}{2}}} \sin \left(k' v_r \right) k' \mathrm{d}k'.
\tag{2.50}
$$

A comparison of this equation with equation 2.32 shows that $\rho(v_r)$ is a Holtsmark distribution with scale parameter $\sigma(t)$ given by

$$
\sigma(t) = 1.15 \left(\frac{2 v_a \phi^2}{225} \right)^{\frac{1}{3}} \frac{e \ln \left(1 + \frac{p e E_a t}{2 m v_a} \right)}{p E_a \epsilon_0},
\tag{2.51}
$$

in which the value of F_n of equation 2.30 is filled in and the initial density of equation 2.7 is used. This scale parameter can be written in terms of the longitudinal position z instead of the time with equation 2.9, resulting in

$$
\sigma(z) = \frac{1.15 \cdot 2^{\frac{1}{3}} e v_a^{\frac{1}{3}} \phi^{\frac{2}{3}} \ln \left(1 + \frac{p}{2} \left(\sqrt{1 + \frac{2 e E_a z}{v_a^2 m}} - 1 \right) \right)}{15^{\frac{2}{3}} p E_a \epsilon_0}.
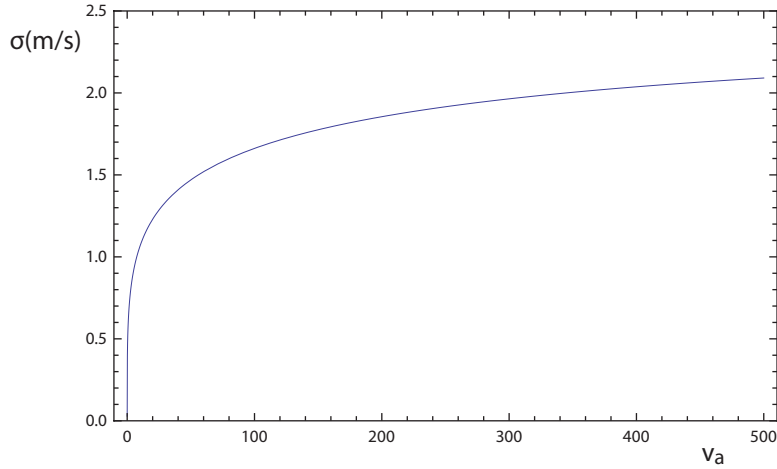\tag{2.52}
$$

21

Figure 2.6 A plot of equation 2.52 as a function of the initial longitudinal velocity for $E_a = 3$ MV/m, $\phi = 5 \cdot 10^{19}$ $m^{-2}s^{-1}$ and z=1 cm.

Equation 2.52 gives a direct relation between the transverse velocity distribution width (related to the transverse beam temperature) in the acceleration stage and the experimental parameters for large beam currents, i.e., $I \gtrsim 10$nA. The dependence on the electric field strength is clear: a larger electric field causes the transverse interaction forces to decay faster, which leads to a narrower transverse velocity distribution. The effect of the flux density can also be understood easily. A larger flux density means that the atoms are closer together at the moment they are ionized. Therefore the initial interaction forces will be larger, so the temperature will be larger as well.

The dependence on the initial longitudinal velocity v_a, which is determined by the temperature of the Knudsen cell and the laser cooling process, is harder to understand. Figure 2.6 shows this dependence for typical values of the other parameters. As can be seen σ is larger for larger longitudinal velocities. The explanation of this effect is as follows. For a larger longitudinal velocity, the density of the atom beam is lower at equal flux densities (equation 2.7). Therefore the average longitudinal distance between an atom and its nearest neighbor will be larger, as it is proportional to $n^{-1/3} = (\frac{v_a}{\phi})^{1/3}$. The average time between ionization of the two atoms is found by dividing this longitudinal distance by the longitudinal velocity, leading a time proportional to $v_a^{-2/3}$. In other words, a larger longitudinal velocity leads to a shorter time between subsequent ionizations. Because the acceleration term in equation 2.8 is much larger than the drift term (with E_a of the order 1 MV/m), this means the atom has traveled less far at the time the next atom is ionized. Therefore there is more heating at smaller longitudinal velocities. Figure 2.6 however shows that for a realistic average value of the velocity of 314 m/s (the average velocity at 400 K), the dependence is very minor. Only at very low velocities of below 100 m/s the dependence becomes significant.

2.2 Simulations

The first part of this chapter was concerned with theoretical models of the Coulomb interaction in the ABLIS setup. The second part of the chapter is devoted to particle tracing simulations using the General Particle Tracing (GPT) software [33].

2.2.1 Simulation setup

In the GPT software the beam is simulated using a certain number of macro particles which typically represent a large number of individual particles. The dynamics of these particles

are determined by the electromagnetic fields of the beam line elements as well by the mutual Coulomb interaction of the particles. The simulations shown in this report are all performed using the built in `spacecharge3Dtree` routine. It uses a Barnes-Hut algorithm to compute the self fields of the particles, in which the interaction between near neighbors is calculated individually, but distant particles are grouped and treated as if they were a single charge or other multipole term. The `spacecharge3Dtree` therefore includes granularity effects, which is crucial for studying disorder-induced heating.

In the simulations ions are being created at a certain rate which is set by means of the beam current. The initial positions of the created particles are determined randomly, but taking into account a certain initial distribution. In the ABLIS setup ions are created by photo-ionization. Therefore the longitudinal initial distribution is a Gaussian with a width that is equal to the width σ_L of the ionization laser. The transverse initial distribution is taken uniform, such that the distribution is constant for a radial position $r < r_A$ and zero for $r > r_A$, where r_A is the radius of the aperture after the cooling and compression stage. In the simulations r_A is implicitly determined by the flux density ϕ and the beam current I. A larger current at a constant flux density, means a larger aperture radius according to

$$r_A = \sqrt{\frac{I}{\pi e \phi}}. \tag{2.53}$$

Since the atoms are laser cooled in the transverse direction before they are ionized, the initial transverse velocity distribution will be Gaussian. The width $\sigma_{v_\perp} = \sigma_{v_x} = \sigma_{v_y}$ of this distribution is determined by the transverse beam temperature $T_\perp$ after the laser cooling stage according to

$$\sigma_{v_\perp} = \sqrt{\frac{k_b T_\perp}{m}}. \tag{2.54}$$

It is assumed the longitudinal velocity distribution $f(v_z)$ is the same Maxwell-Boltzmann distribution as was created by the Knudsen cell [22]. In the simulations this distribution is approximated by a Gaussian centered at the average longitudinal velocity $v_{z,avg}$ given by

$$v_{z,avg} = \sqrt{\frac{8 k_b T_{oven}}{\pi m}}, \tag{2.55}$$

and a RMS-width σ_{v_z} equal to the RMS-width of the Maxwell-Boltzmann distribution,

$$\sigma_{v_z} = \sqrt{\frac{(3 - \frac{8}{\pi}) k_b T_{oven}}{m}}. \tag{2.56}$$

Strictly spoken the longitudinal velocity distribution will be changed by the laser cooling and compression stage since particles with a lower velocity have a larger probability of being compressed towards the center of the beam. Therefore these particles have a larger chance of being selected by the aperture in front of the acceleration stage. In practice this means that the longitudinal velocity distribution is still a Maxwell Boltzmann distribution but with a lower temperature than T_{oven}.

The beam line of the simulations is shown is figure 2.7. The ions are created at $z=0$ and the accelerator is simulated by a constant electric field which is pointing in the z-direction with an electric field strength E_a. The electric field strength jumps from E_a to zero at d_a. Unless stated otherwise the values of parameters in the simulation are shown in table 2.1.

2.2.2 Brightness vs. current

Since the beam size in the ionization stage is dependent on the current (see equation 2.53), the current determines the regime in which the beam is. At very low currents the beam will

Table 2.1 Simulation parameters.

Parameter name	Symbol	Value
Oven temperature	T_{oven}	400 K
average atom velocity	v_a	315 m/s
Atom mass	m	85.47 amu
Laser width	σ_L	1 μm
Length acceleration stage	d_a	1 cm
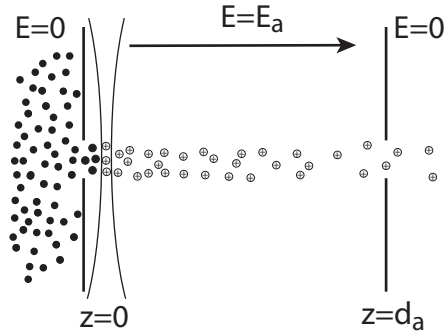
Figure 2.7 Schematic overview of the beam line in the simulations. The ions are created at z=0 and accelerated with an electric field E_a up to $z = d_a$.

be in the pencil beam regime which is characterized by the fact that the average longitudinal separation is much larger than the beam size. At very large currents it will be in the extended regime in which the longitudinal separation is much smaller than the beam size. To characterize this, simulations are performed of the reduced brightness at the end of the acceleration stage as a function of the current. The results of these simulations are shown in figure 2.8. In these figures the brightness B_r is the reduced brightness of the best 50 percent of the beam. This 50 percent brightness is calculated with a GPT program which determines the smallest possible phase space volume that contains 50 percent of the particles. From this phase space volume a phase space density is calculated which can be linked to the brightness. In practice this brightness can be realized by placing an aperture in the waist of the beam. If this aperture only transmits the 50 percent of particles closest to the axis the brightness of the transmitted beam is the 50 percent brightness.

As can be seen, at very low currents the brightness is independent of the exact value of the current. This is caused by the fact that at very low currents the ions will be on a line and all forces will be in the longitudinal direction. No transverse heating will take place and the brightness will remain at its maximum value, determined by the laser cooling and compression. When the beam current becomes higher, the beam diameter becomes larger and ions have a larger probability to be created at the same longitudinal position, in other words they can become transverse 'neighbors'. Therefore a larger part of the interaction force will point in the transverse direction and the brightness will start to decrease. When the current is raised even more the beam diameter becomes even larger and the brightness keeps becoming lower; however, the rate at which this happens gets smaller from a certain current onward. This is caused by the fact that only particles in close vicinity of each other will interact, i.e., a particle at the border of the beam will exert a much smaller force upon a particle in the center of the beam than a particle closer to the center of the beam will do. At large currents, the beam diameter will therefore be so large that an increase of current will have no significant effect on the brightness of the beam. So the brightness is independent of the beam current in the extended regime. Although the rate in decrease has become small at 10 nA, it still decreases so the extended regime is not fully reached at that current.
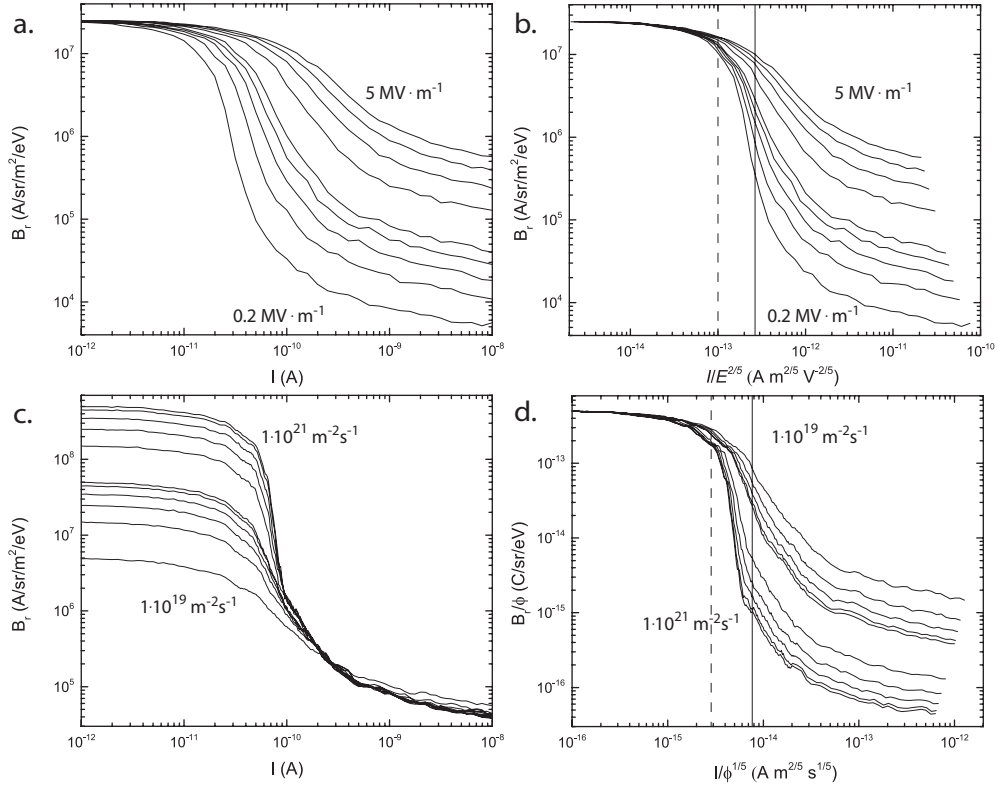
Figure 2.8 Simulation results showing the brightness at a longitudinal position of 10 mm, as a function of current for: (a) a constant flux density of $5 \cdot 10^{19}$ m^{-2}s^{-1} and varying electric field strengths and (c) a constant electric field of 1 MVm^{-1} and varying flux densities. In figures b and d the same simulations are plotted, but for a scaled current, showing the dependence of the current at which the transverse heating starts to occur on the electric field strength. The solid vertical lines in figure b and d show the current for which the transverse size of the beam is equal to the average initial longitudinal separation of the ions in the beam (equation 2.57). The dashed vertical lines indicate the (somewhat arbitrary) end of the pencil beam regime.

Figure 2.8a shows that the current at which the brightness drops is larger for higher electric field strengths. This is caused by the fact that because of a higher electric field strength the ions are accelerated more. Because of this larger acceleration each ion will be at a larger longitudinal position at the moment the next ion is created, so they will repel each other less. The current at which the brightness starts to drop, is hard to quantify. What can be quantified is the current for which the beam diameter is equal to the average initial longitudinal separation of the ions. The average time between the ionization of two atoms is $\frac{e}{I}$. Therefore the position of the front ion at the moment the next ion is ionized can be calculated by using this value for the time in equation 2.8. Equating this position to the beam diameter (using equation 2.53) leads to

$$I = \left(\frac{e^3 E_a}{4m} \sqrt{\pi e \phi} + e v_a I \right)^{\frac{2}{5}} \approx \left(\frac{e^3 E_a}{4m} \sqrt{\pi e \phi} \right)^{\frac{2}{5}}. \tag{2.57}$$

This equations reveals the dependence between the current at which the brightness starts to drop and the electric field and the flux density. It shows that this current scales with $E_a^{\frac{2}{5}}$ and $\phi^{\frac{1}{5}}$. Figures 2.8b and 2.8d show the same data as figure 2.8a and 2.8c, but now as a function of a scaled current. It can be seen that the scaling is right. No significant heating takes place up till approximately a quarter of the value given by equation 2.57.

Figure 2.8c shows that a higher current density leads to higher brightness at low currents. This is expected according to equation 1.3, which shows the brightness is proportional to the current density and inversely proportional to the transverse temperature. The transverse temperature is constant at these low currents, so the brightness is higher for larger flux densities. At high currents the brightness is nearly the same for all simulated flux densities. Apparently the increase in temperature (nearly) cancels out the higher brightness because of the higher flux density. This plot shows that it is beneficial to have an as high as possible flux density, since it gives a higher brightness at low currents and (nearly) does not affect the brightness at high currents.

According to equation 2.52 the width of the transverse velocity distribution is proportional to $\phi^{\frac{2}{3}}$. It is hard to connect this width to a temperature; moreover it is not possible to calculate a temperature at all since the second moment of the Holtsmark distribution does not exist. Because the Holtsmark distribution is very similar to the Gaussian distribution, a good approximation however is to take the temperature to be proportional to the square of the width σ of the distribution. In this approximation the transverse temperature is proportional to $\phi^{\frac{4}{3}}$. Therefore according to equation 1.3 the brightness in the extended regime is expected to be proportional with $\phi^{-\frac{1}{3}}$, so a higher flux density leads to a slightly lower brightness in the extended regime. This does not entirely agree with the brightnesses at which the different curves saturate in figure 2.8c. The reason for this disagreement is probably the fact that the extended regime is not completely reached at 10^{-8} A, since the brightness still decreases slightly as a function of the current.

2.2.3 Phase space evolution

In this section the phase space evolution of the beam is investigated at a current of 10^{-8} A. As explained previously, at this current the extended regime is not completely reached. The evolution of the transverse velocity distribution should however still be predictable by the theory of section 2.1.6 to a reasonable extend since the extended regime is almost reached. A current of 10^{-8} A is preferred over higher currents in the simulation, since for higher currents more particles had to be used, which goes at the cost of a larger computation time. Using GPT phase space plots and uncorrelated velocity plots of the beam are made at different positions. Figure 2.9 shows these plots for an electric field of $1 \text{ MV} \cdot \text{m}^{-1}$ and flux density of $5 \cdot 10^{19} \text{ m}^{-2}\text{s}^{-1}$. The positions at which these figures are made are all inside the accelerator structure. The phase space plots show that a correlation between the velocity and position is built up. This correlation is caused by two effects: space charge acceleration and expansion.

The uncorrelated velocity plots show the distributions of the uncorrelated transverse velocities which are found by subtracting a linear fit from the phase space data. The velocity distribution at $z = 0$ is fitted with a Gaussian distribution, since this is the expected distribution after the cooling and compression stage. The distributions at $z = 1$ mm and $z = 1$ cm are fitted with a Holtsmark distribution, which is the expected shape of the distribution after disorder-induced heating has taken place in the extended regime. The distributions fit the data very well. Therefore, fits like these are used to investigate the evolution of the distribution width as a function of the longitudinal position.

Figure 2.10 shows plots of the simulated transverse and longitudinal distribution widths as a function of the longitudinal position for varying electric field strength. These simulations were performed for a simplified beam in which the width of the ionization laser was set to zero and no energy spread was present before ionization. This was done to avoid any transverse heating due to relaxation of kinetic energy. The thick line in figure 2.10 is a plot of equation 2.52 for $p = 0.33$. This value was found by comparison with the simulation results. Despite all simplifications that were made in the derivation of equation 2.52 the resemblance between the transverse simulation data and the theoretical curve is very large. Apparently the value of p is independent of the electric field in this range of fields.

As expected the distribution width in the longitudinal direction grows faster than the width in the transverse direction. This is caused by the fact that the interaction force between the ions is forced towards the longitudinal direction as was explained in section 2.1.5. However this is only the case in the very first part of the acceleration stage. After a few tenths of mm it smooths out and even starts to decrease a bit. This effect can be attributed to the fact that acceleration lowers the longitudinal velocity spread while the energy spread is unaffected. According to [34] the relation between temperature T_i for direction i and average energy $\langle E_i \rangle$ present in direction i is given by

$$k_b T_i = \frac{(\Delta E_i)^2}{4 \langle E_i \rangle}, \tag{2.58}$$

in which ΔE_i represents the spread in the energy present in direction i. It shows that T_z is inversely proportional to $\langle E_z \rangle$ and since acceleration increases $\langle E_z \rangle$, it would decrease the temperature if the energy spread would remain constant. However, the energy spread increases as a function of position due to disorder-induced heating. In other words, in terms of the longitudinal temperature the heating and the acceleration are two competing processes, which lead to the dotted curves shown in figure 2.10.

Figure 2.11 shows the same kind of plots, but for a varying flux density and a constant electric field strength. It can be seen that the value of p has to be adjusted a little bit to achieve a full similarity between the theory and simulations. This is caused by the fact that the flux density determines the average separation between the particles before they are ionized. Therefore the flux density determines the value of z_0 in figure 2.4. A higher flux density means that the particles are closer together and z_0 is smaller. As can be seen in the same figure this means that the slope of $f(t)$ (equation 2.44) is larger. Therefore the value of p should also be larger for higher flux densities, as is indeed the case. For a flux density of $3 \cdot 10^{20}$ m^{-2}s^{-1}, no satisfactory result can be achieved for the theoretical curve by adjusting the value of p. At this high values of the flux densities the shape of the curve changes, i.e., a stagnation in the growth of σ occurs around 0.3 mm. This is caused by the fact that the first order approximation is not valid anymore. Due to the higher flux density, the space charge effect will be larger and the velocities which the particles achieve due to the space charge acceleration will also be larger. Therefore the expansion cooling, which was explained in section 2.1.1, starts to occur at smaller longitudinal positions. The stagnation of the growth of σ around 0.3 mm can be ascribed to this effect.
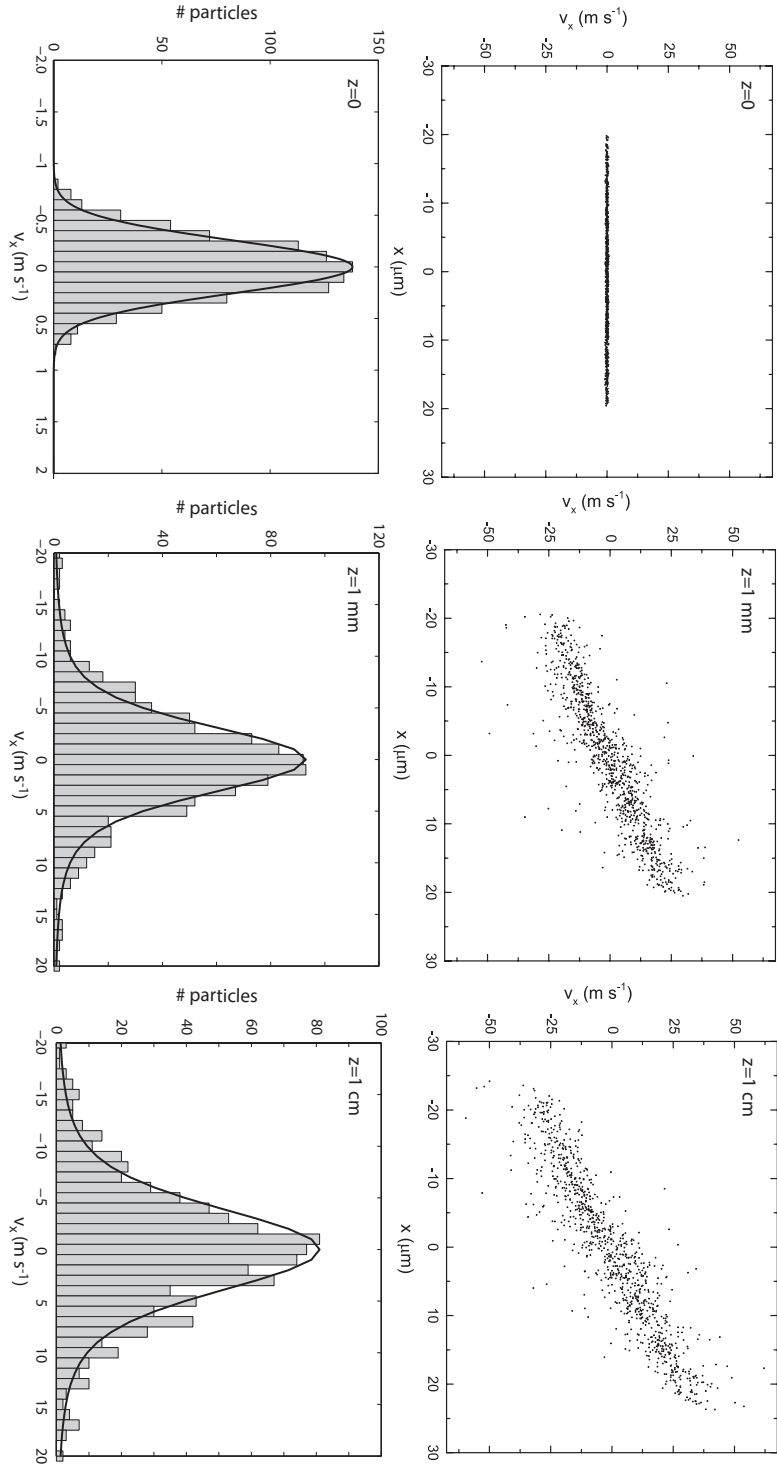
Figure 2.9 Phase space and transverse velocity distribution plots at different longitudinal positions. The velocity distribution at $z = 0$ is fitted with a Gaussian, leading to $\sigma = 0.18 \mathrm{m \cdot s^{-1}}$, while those at $z = 1$ mm and $z = 1$ cm are fitted with a Holtsmark distribution, leading to $\sigma = 2.76 \mathrm{m \cdot s^{-1}}$ and $\sigma = 3.41 \mathrm{m \cdot s^{-1}}$.
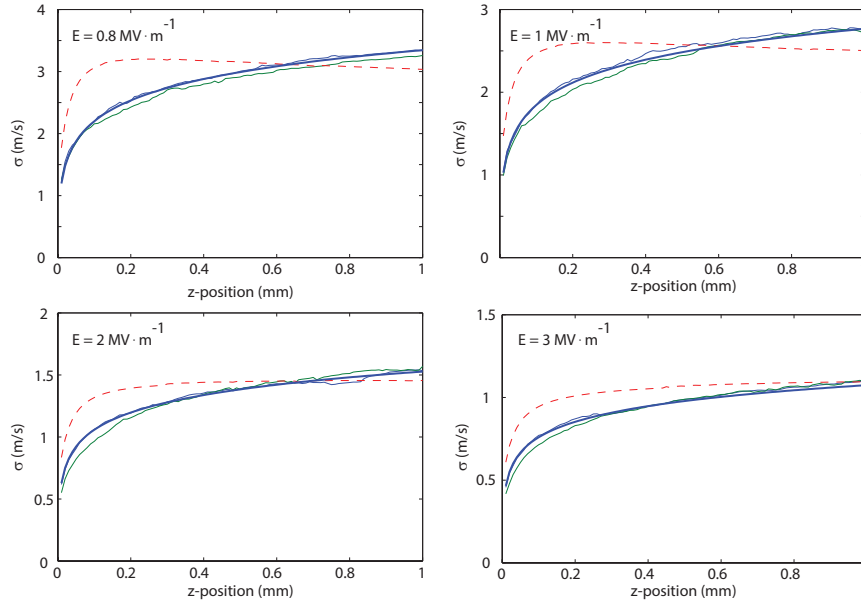
Figure 2.10 Plots of the (Holtsmarkian) distribution widths as a function of longitudinal position for different electric field strengths and a flux density of $5 \cdot 10^{19}$ m^{-2}s^{-1}. The two thin solid curves are the distribution widths of the two transverse directions, the dashed curve is the distribution width of the longitudinal direction and the thick solid curve is a plot of equation 2.52 for $p = 0.33$.
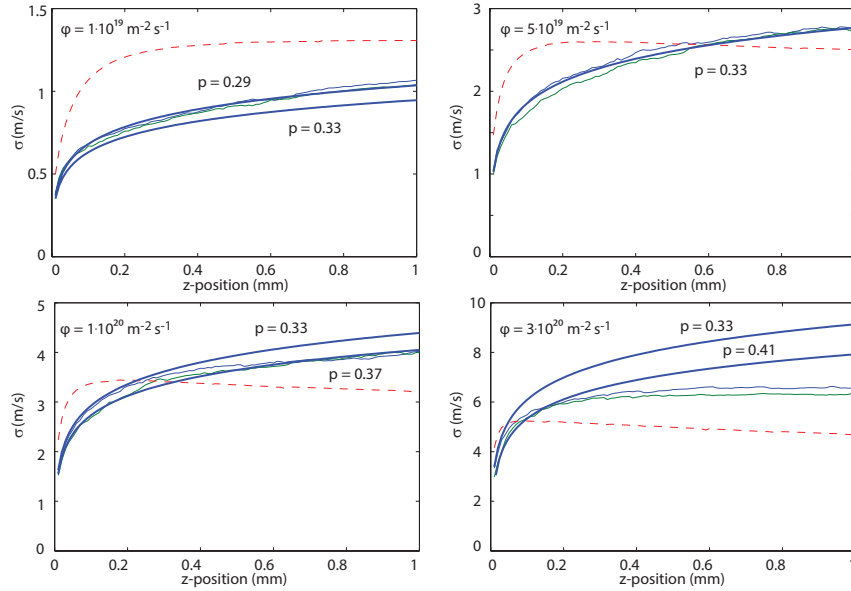

Figure 2.11 Plots of the (Holtsmarkian) distribution widths as a function of longitudinal position for different flux densities and an electric field strength of 1 MVm^{-1}. The two thin solid curves are the distribution widths of the two transverse directions, the dashed curve is the distribution width of the longitudinal direction and the thick solid curves are plots of equation 2.52 for different values of p, which are indicated in the figures.
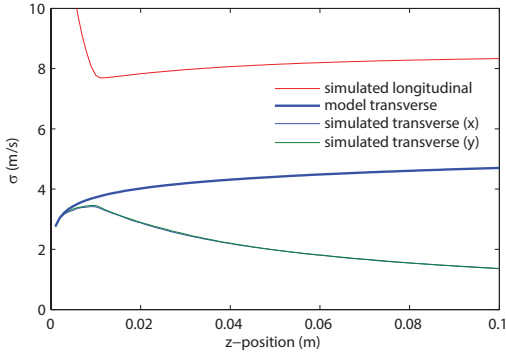
Figure 2.12 The width of the transverse and longitudinal velocity distribution widths as a function of the longitudinal position. In the simulation a realistic accelerator structure was used of 1 cm.
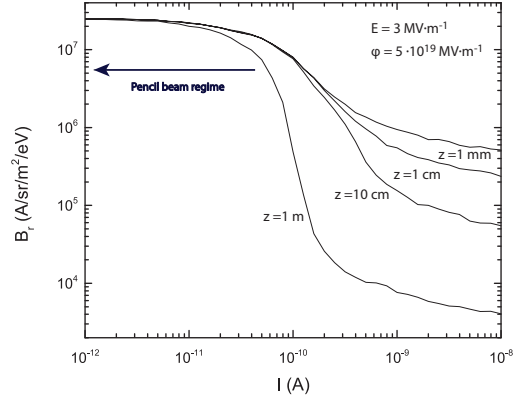

Figure 2.13 Plots of the 50 percent reduced brightness as a function of the beam current at different longitudinal positions.

2.2.4 Heating after acceleration stage and effect of energy spread

In the previous sections simulation results were shown of brightness and distribution widths at 1 mm and 1 cm, which is the position at which the accelerator stage ends. However, it is not known whether all disorder-induced heating takes place within this first centimeter or if there is also heating of the ion beam in the rest of the setup. Therefore simulations are performed of the brightness at larger longitudinal positions. Furthermore, in the simulations shown in section 2.2.3, the assumption was made of a monochromatic beam and an infinitely small laser beam width. This was done to be sure that no relaxation of kinetic energy from the longitudinal direction to the transverse direction could take place, so that only the effects of disorder-induced heating were taken into account. The simulation in this section are done to investigate heating after the acceleration stage as well as heating due to relaxation of kinetic energy.

Figure 2.12 shows simulation results of the velocity distribution widths as a function of the longitudinal position. In this simulation a realistic accelerator structure is used to incorporate the exit kick of the accelerator. Because the electric field will switch from E_a to 0 at the end of the accelerator, the particles will experience an outward force [35], the so called exit kick. The end of the accelerator ($z=1$ cm) is clearly visible in the curves. Inside the accelerator, the longitudinal velocity distribution width decreases according to equation 2.58. After the first centimeter it doesn't decrease anymore since the average kinetic energy does not increase anymore. It even starts to increase which can be attributed to disorder-induced heating. No trend towards a decline of longitudinal temperature can be seen. Therefore it can be concluded that relaxation of kinetic energy towards the transverse direction does not play a role or is at least much smaller than the disorder-induced heating in the longitudinal direction. The transverse distribution widths start to decrease from the end of the accelerator onwards. This is caused by expansion cooling as was explained in section 2.1.1. Due to the space charge acceleration, a correlation between velocity and position is built up inside the accelerator. This correlation is is strengthened due to the exit kick of the accelerator, after which the beam starts to expand significantly.

As explained in the previous paragraph the transverse temperature decreases after the accelerator due to expansion of the beam. Therefore temperature is not a good measure for beam quality in the rest of the setup. The brightness however is, so to get a conclusive answer of disorder-induced heating after the acceleration stage, simulations are performed of the brightness as a function of the beam current at different longitudinal positions. The results are shown in figure 2.13. From these results it can be concluded that at large currents

(I >100 pA) the disorder-induced heating is still significant after the accelerator. In the extended regime the brightness still drops about two orders of magnitude. In the pencil beam regime however, the brightness is still not affected after 1 m, which is not surprising, since the ions are on a line, so if there was any heating at all, it was in the longitudinal direction.

2.3   Conclusion

In this section the most important conclusions on the investigation of disorder-induced heating in the ABLIS setup are summarized.

- The basis of an analytical solution for the brightness or beam temperature as a function of experimental parameters was the extended two-particle approximation of Jansen [28]. This model was extended with several assumptions and led to a closed form analytical solution. This solution for the transverse velocity distribution width of equation 2.52 is, due to the assumptions, only valid inside the acceleration stage and for large currents. When these assumptions are fulfilled the solution agrees very well with particle tracing simulations. It predicts, as expected, a larger beam temperature for smaller electric fields and larger flux densities. Furthermore the dependence on the initial velocity is small.

- The disorder-induced heating in the ABLIS setup is investigated numerically using GPT simulations. A higher electric field extends the pencil beam regime, in which no transverse disorder-induced heating takes place, towards higher currents. With an electric field of 5 MV/m the pencil beam regime reaches up till ≈70pA. It was found that the current at which the pencil beam regime ends scales with $E_a^{\frac{2}{5}}$ and $\phi^{\frac{1}{5}}$.

- In the pencil beam regime, also no disorder-induced heating takes place after the acceleration stage. In the extended regime however, heating in the rest of the setup is not negligible. The brightness drops about two orders of magnitude after one meter drift. This will limit the use of an ABLIS-based FIB at higher currents (>100pA).

- Purely regarding disorder-induced heating it is beneficial to achieve an as high as possible flux density. In the pencil beam regime the brightness remains unaffected, therefore a higher density means a higher brightness. The pencil beam regime is even shifted a bit towards higher currents for higher densities, since a higher density means a smaller beam size at equal currents.

Chapter 3

Probe size contributions

In the previous chapter disorder-induced heating and its relation with experimental parameters was investigated. It was concluded that disorder-induced heating could be suppressed at low currents (I<100pA) as long as the acceleration electric field is high enough. However, as explained in the Introduction a higher electric field leads to larger chromatic aberrations of the lens system. These aberrations will finally lead to a larger spot size. In order to quantify this effect, all individual contributions to the probe size of a charged particle beam have to be identified and investigated.

As a starting point of this chapter, the assumption is made that the laser cooling and compression stage has produced an atomic beam with a current density J_S and a transverse temperature of T_r. The values of these parameters are based on laser cooling and compression simulations, which are not discussed here. A schematic view of the ion beam line in the ABLIS setup is shown in figure 3.1. The atomic beam enters the figure from the left and is apertured when it enters the ionization stage, which has a length d_a. When it leaves the ionization stage the ion beam goes from a region with an electric field E_a to a region without any electric field. A side effect of this structure is that it will act as a negative lens for the ions, with a focal length f_a [35]. The beam will then drift over a distance L towards a lens system with a focal length f, which is illustrated as a thin lens in figure 3.1. Due to this lens the beam will be focused to a small spot. A summary of the important parameters in this chapter and their values is given in table 3.1. Most of the parameters will be further explained in the rest of the chapter.

The rest of this chapter deals with the analytical treatment of the most important contributions to the ABLIS probe size. Since the current density distribution at the lens is of
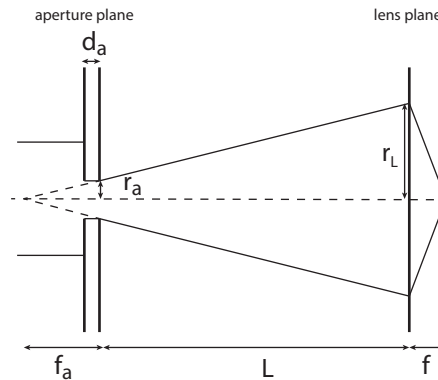

Figure 3.1 A schematic overview of the acceleration stage and the drift region towards the lens plane.

Table 3.1 A summary of the parameters describing the ion beam line in the ABLIS setup.

Parameter [unit]	Symbol	Value
Source current density [Am^{-2}]	J_S	10.91
Transverse temperature [mK]	T_r	0.8
Rubidium mass [amu]	m	84.91
Accelerator length [cm]	d_a	1
Exit kick focal length [cm]	f_a	-4
Drift length between accelerator and lens system [cm]	L	20
Last lens focal length [mm]	f	6.5
Mean ion kinetic energy [keV]	U_m	30

influence on all individual contributions it is discussed in the first section. In the following three sections the brightness-limited probe size and spherical and chromatic aberration are discussed. The last sections are dedicated to the problem of how to combine the individual contributions to one single probe size and a discussion of the expected performance of the ABLIS setup.

3.1 Current density distribution

In the ABLIS setup atoms are cooled and compressed before they are apertured. If the radius r_a of the aperture is chosen sufficiently small the current density in the aperture will be constant and given by

$$J\left(R'\right) = \frac{I}{\pi r_a^2} = J_s \qquad (3.1)$$

where I represents the total current through the aperture and the symbol $J_s = e\phi$ is introduced for the source current density. After this aperture the atoms will be ionized with a very intense laser, which will ionize all atoms. The produced ions are immediately accelerated in a homogeneous electric field $E_a = \frac{V}{d_a}$ over a distance d_a, in which the ions achieve a kinetic energy qV, with q the charge of the ion and V the acceleration potential. Since the ions will go from a region with an electric field E_a to a region with no electric field after the ionization stage, the ions will get a momentum kick in the positive radial direction at the border between these regions. In other words the accelerator works as a negative lens. The focal length f_a of this lens is given by [35]

$$f_a = -\frac{4U_0}{qE_a} = -\frac{4qV}{q\frac{V}{d_a}} = -4d_a, \qquad (3.2)$$

where U_0 represents the mean ion kinetic energy, which is assumed to be negligible compared to qV before the accelerator ($U = U_0 + qV \approx qV$, in which U_0 is the kinetic energy before the accelerator). The lens action of the exit kick is illustrated in figure 3.1.

Since the atoms will have a finite temperature, each point in the aperture will lead to a two-dimensional Gaussian distribution in the lens plane. Therefore the current through the infinitesimal ring-shaped surface $2\pi R'dR'$ with radius R' and width dR' in the aperture plane will be imaged as a ring-shaped infinitesimal Gaussian distribution $dJ\left(R\right)$ in the lens plane. This $dJ\left(R\right)$ is given by

$$dJ\left(R\right) = dC\left(e^{-\frac{\left(R - R'\left(1 - L/f_a\right)\right)^2}{\sigma_R^2}} + e^{-\frac{\left(R + R'\left(1 - L/f_a\right)\right)^2}{\sigma_R^2}}\right) \qquad (3.3)$$

where R represents the radial position in the lens plane, σ_R is the RMS spread in the radial position in the lens plane of the ions originating from one point in the aperture plane, dC

is a normalization constant and L is the distance between the ionization stage and the lens. The RMS spread σ_R is given by the RMS spread in divergence multiplied by a length factor determined by the geometry. Assuming the temperature of the ions in the radial direction is given by T_r, the mass of the ions is m and the kinetic energy of the ions is U_0, σ_R can be written as

$$\sigma_R = \sqrt{\frac{k_b T_r}{2U_0}} \left(L + \frac{L - f_a}{4} \right) \tag{3.4}$$

where k_b is Boltzmann's constant. Equation 3.4 shows that σ_R consists of two terms. The first one is simply the RMS spread in divergence multiplied with the drift length, which would have been the RMS spread if no exit kick was present after the acceleration. The other term is the extra contribution due to the exit kick.

To find the value of the normalization constant dC we consider the infinitesimal current dI flowing through the surface $2\pi R' dR'$. This dI should be equal to the integral of $dJ(R)$ over the whole lens plane, so

$$dI = J_s 2\pi R' dR' = \int\limits_0^\infty 2\pi R \, dC \left(e^{-\frac{(R - R'(1 - L/f_a))^2}{\sigma_R^2}} + e^{-\frac{(R + R'(1 - L/f_a))^2}{\sigma_R^2}} \right) dR. \tag{3.5}$$

Rewriting this equation and solving the integral leads to

$$dC = \frac{-f_a J_s R'}{-f_a \sigma_R^2 e^{-\frac{(L - f_a)^2 R'^2}{f_a^2 \sigma_R^2}} + \sqrt{\pi}(L - f_a) R' \sigma_R erf\left(-\frac{(L - f_a)R'}{f_a \sigma_R}\right)} dR' = f(R') dR'. \tag{3.6}$$

The last step in finding the current density in the lens plane is to add all infinitesimal contributions, i.e., integrating over all $dJ(R)$. Using equations 3.3 and 3.6 this leads to

$$J(R) = \int\limits_0^{r_a} f(R') \left(e^{-\frac{(R - R'(1 - L/f_a))^2}{\sigma_R^2}} + e^{-\frac{(R + R'(1 - L/f_a))^2}{\sigma_R^2}} \right) dR'. \tag{3.7}$$

Figure 3.2 shows a plot of $J(R)$ for different values of the total current. It can be seen that for most values of the current $J(R)$ can be approximated by a uniform distribution. In the center and at the edge the distribution is different from a uniform distribution. The length scale over which this deformation takes place is σ_R. Only for small currents (I<1 pA), when the size of the beam is comparable to σ_R, the distribution deviates from a uniform one significantly.

3.2 Brightness limited probe size

As was already hinted in the Introduction the brightness determines together with the angular spread the achievable spot size if a perfect lens would be used, i.e., a lens lacking of any aberrations. This is done by using the brightness as given by equation 1.1. In the waist of a beam the correlation term $\langle iv_i \rangle$ in this equation becomes zero and the brightness can be written as

$$B_r = \frac{I}{2\pi^2 m \sigma_x \sigma_y \sigma_{v_x} \sigma_{v_y}} \tag{3.8}$$

in which σ_x and σ_y represent the RMS positions in the waist of the beam and σ_{v_x} and σ_{v_y} are the RMS velocities in the whole beam segment. For an azimuthally symmetric beam $\sigma_x = \sigma_y = \frac{1}{\sqrt{2}} \sigma_r$ and $\sigma_{v_x} = \sigma_{v_y} = \frac{1}{\sqrt{2}} \sigma_{v_r}$ with σ_r the RMS position in the radial direction in the waist and σ_{v_r} the RMS velocity in the radial direction. Using these equalities one can write the reduced brightness of a non-relativistic beam as

$$B_r = \frac{2I}{\pi^2 m \sigma_r^2 \sigma_{v_r}^2} \frac{\frac{1}{2} m v_z^2}{U_0} = \frac{I}{\pi^2 U_0 \sigma_r^2 \sigma_{r'}^2}, \tag{3.9}$$
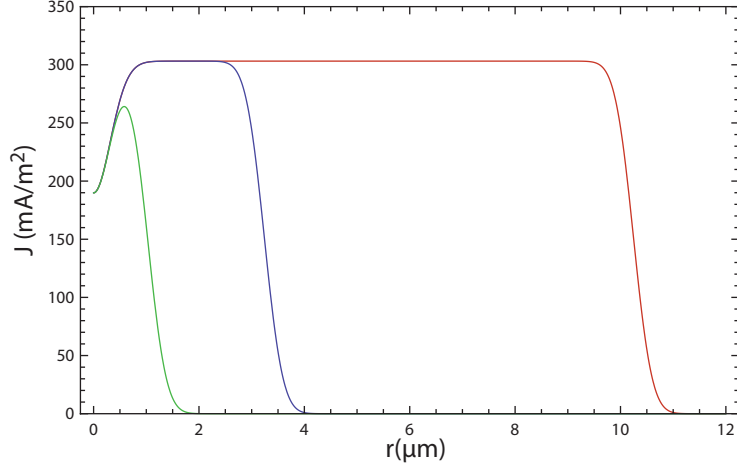
Figure 3.2 Plot of the current density in the lens plane as a function of the radial position for a total current of 1 pA, 10 pA and 100 pA.

in which is made use of the fact that the kinetic energy of the beam $U_0 = \frac{1}{2}mv_z^2$, with v_z the average axial velocity of the ions and with $\sigma_{r'}$ the RMS divergence. Rewriting this equation in terms of σ_r gives an equation for the RMS size of the beam in the waist. As can be seen this size will be limited by the spread in divergence, which is determined by the spread in radial position at the lens and therefore by the current density distribution.

As was shown in section 3.1, the current density at the lens can be approximated by a circular uniform distribution for most values of the current. The radius r_L of this distribution is given by

$$r_L = -\frac{L - f_a}{f_a}r_a, \tag{3.10}$$

as can be verified using figure 3.1. Furthermore for a uniform circular distribution the RMS radial position is the same as $d_{50}/2$, in which d_{50} is the diameter of a circle containing 50 percent of the current, therefore

$$\sigma_{r_L} = \frac{d_{50,L}}{2} = \frac{1}{\sqrt{2}}r_L. \tag{3.11}$$

Under the assumption of a perfect lens, the RMS spread in divergence in the waist $\sigma_{r'_f}$ can be calculated with

$$\sigma_{r'_f} = \frac{\sigma_{r_L}}{f}. \tag{3.12}$$

Rewriting equation 3.9 and making use of equation 3.10-3.12 leads to a spot size σ_{r_f} in the focal plane of

$$\sigma_{r_f} = \frac{f r_a}{r_L v_z}\sqrt{\frac{4 J_s}{\pi m B_r}}. \tag{3.13}$$

This equation shows that σ_{r_f} is inversely proportional to the brightness of the beam. So the spot size is limited by the brightness, hence the name 'brightness limited spot size'. Although Equation 3.13 is a valid equation for σ_{r_f}, filling in the expression of equation 3.9 makes the equation much clearer. Doing this and substituting the values of σ_r and $\sigma_{r'}$ in the aperture plane, i.e., $\sigma_{r_A} = \frac{r_A}{\sqrt{2}}$ and $\sigma_{r'_A} = \frac{1}{v_z}\sqrt{\frac{k_b T_r}{m}}$, leads to

$$\sigma_{r_f} = \frac{d_{50,B}}{2} = \frac{f r_a}{r_L v_z}\sqrt{\frac{k_b T_r}{m}}, \tag{3.14}$$

in which $d_{50,B}$ represents the brightness limited spot size (diameter) containing 50 percent of the current.

Surprisingly the final brightness-limited spot size is independent of the total current. When the total current is increased the radius of the aperture after the cooling and compression stage is also increased, which increases the emittance. However the divergence spread after the final lens will increase with the same factor since it is proportional to the radius of the aperture (see equation 3.10). Therefore the final spot size in the Gaussian image plane will be the same.

In equation 3.14 it looks like the spot size is inversely proportional to the axial velocity v_z. However, the spot size is actually independent of v_z since the focal length of the lens is also proportional to v_z. Equation 3.14 does show the dependence on other parameters however. A larger divergence after the last lens leads to a smaller brightness-limited spot size. Therefore a larger drift length and a smaller focal length of the exit kick lead to a smaller brightness limited spot size. Furthermore a lower beam temperature leads to a higher brightness and therefore a smaller brightness limited spot size. For the values stated in table 3.1, $d_{50,B}$ is 1.6 nm.

3.3 Spherical aberration

The theory of Gaussian imaging makes use of the paraxial approximation which does not take into account higher order terms in the radial position and radial divergence. Therefore all particles in a non-divergent beam with transverse temperature equal to zero will in this theory be focused to a single point, i.e., $\sigma_{r_f} \to 0$ for $T_r \to 0$ (see equation 3.13). When higher order terms are however taken into account, such a beam will not be focused to a single point, but will have a certain size in the Gaussian image plane. Deviations from the Gaussian theory of imaging due to these higher order terms are usually referred to as geometrical aberrations. As explained in most basic optics books (for example [36]) geometrical aberrations can be divided into different types. From all types of geometrical aberrations, only spherical aberration usually plays a significant role in the probe size of a focused ion beam.

It can be shown that an ion which has a radial position R in the lens plane will have a radial position $C_s \frac{R^3}{f^3}$ [37] in the Gaussian image plane, in which C_s is the so-called spherical aberration constant. Doing basic geometrical calculations, it can then also be shown that the radial position r in an observation plane positioned a distance Δz before the Gaussian image plane is given by

$$r = \left| \frac{\Delta z}{f} R - \frac{C_s R^3}{f^3} + \frac{C_s R^3 \Delta z}{f^4} \right| \approx \left| \frac{\Delta z}{f} R - \frac{C_s R^3}{f^3} \right|, \tag{3.15}$$

where the assumption is made that $\frac{C_S R^3}{f^3} \ll R$ and $\frac{\Delta z}{f} \ll 1$.

The approach discussed in [38] is used to calculate the current density and probe size due to spherical aberration in the observation plane. By making the substitutions $x = \sqrt{\frac{C_s}{\Delta z}} \frac{R}{f}$ and $y = \sqrt{\frac{C_s}{\Delta z^3}} r$, equation 3.15 can be written as

$$y(x) = \left| x - x^3 \right|. \tag{3.16}$$

A plot of $y(x)$ is shown in figure 3.3. As can be seen there is not a one to one relationship between x and y, and therefore neither between R and r.

Figure 3.3 shows that when

$$y \leq \frac{2}{3\sqrt{3}} \text{ and}$$
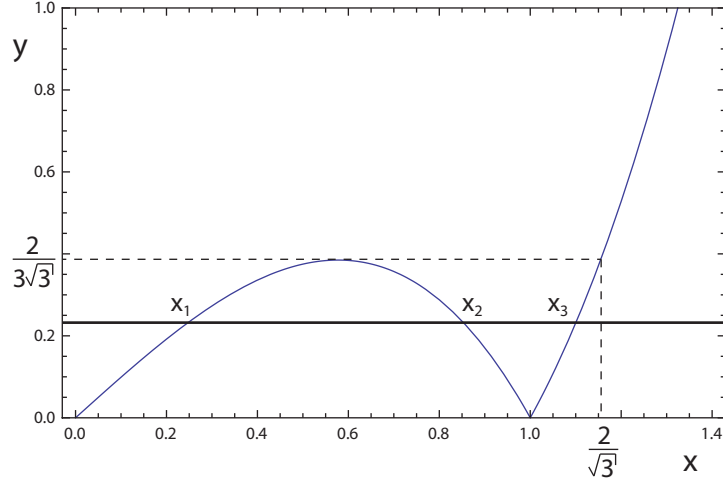$$x \leq \frac{2}{\sqrt{3}}, \tag{3.17}$$

Figure 3.3 A plot of equation 3.16.

there are two parts that contribute to the fraction of current β contained within a radius y, namely the current that falls between 0 and x_1 and between x_2 and x_3 in the lens plane. Taking this into account the fraction of current can be calculated as

$$\beta\left(y\right) = \frac{\int_{R_{range}} 2\pi R dR}{\pi r_L^2} = \frac{2}{x_L^2}\left(\int_0^{x_1} x dx + \int_{x_2}^{x_3} x dx\right) = \frac{x_1(y)^2 - x_2(y)^2 + x_3(y)^2}{x_L^2}, \quad (3.18)$$

in which R_{range} is that part of the domain of radial positions at the lens plane which will lead to a radial position smaller than y in the image plane and $x_1(y)$, $x_2(y)$ and $x_3(y)$ are the three cubic roots of equation 3.16. When these roots are expressed in terms of y, an equation is derived for y which can be transformed back to an equation for the radius $r(\beta)$ of a circular surface which contains a fraction β of the current,

$$r\left(\beta\right) = \frac{\beta}{2}\sqrt{\zeta - \frac{\beta}{2}} C_s \frac{r_L^3}{f^3} \quad (3.19)$$

in which the so-called defocus $\zeta = \frac{\Delta z}{C_s \frac{r_L^2}{f^2}}$ is introduced. Using equation 3.19 and the definition of the defocus, the constraints in x and y (equation 3.17) lead to constraints in terms of ζ. Therefore equation 3.19 is only valid for $\frac{3\beta}{4} \leq \zeta \leq \frac{3}{4}$, so the minimal spherical aberration limited spot is found at $\zeta = \frac{3\beta}{4}$. Using a value of $\beta = \frac{1}{2}$ the 50 percent fraction of current diameter $d_{50,S}$ of the spherical aberration probe size can be written as,

$$d_{50,S} = \frac{1}{4\sqrt{2}} C_s \frac{r_L^3}{f^3} \quad (3.20)$$

Realistic values for the spherical aberration and a comparison of spherical aberration with other contributions are found in section 3.6.

3.4 Chromatic aberration

Chromatic aberration is a term that is used for the phenomenon that ions with a different axial velocity experience a different focal length when traveling through a lens. To investigate the effect of chromatic aberration, again the approach of [38] is used. Due to chromatic

aberration, an ion with a kinetic energy U that has a radial position R at the lens, has a radial position r in the Gaussian image plane, that in a first order approximation in $\left|\frac{U-U_0}{U_0}\right|$ is given by

$$r = \frac{C_c}{f}\left|\frac{U-U_0}{U_0}\right|R \tag{3.21}$$

with the chromatic aberration coefficient given by C_c and U_0 representing the average kinetic energy of the ions in the beam. Equation 3.21 gives a mapping between the radial positions in the lens plane and the Gaussian image plane. Making use of this mapping, the current distribution $J(r)$ in the Gaussian image plane can be derived from the current distribution $J(R)$ in the lens plane. The infinitesimal current dI flowing through the area $2\pi R dR$ is with the mapping of equation 3.21 also flowing through the area $2\pi r dr$ and is given by

$$\mathrm{d}I = 2\pi R J_U(R,U)\,\mathrm{d}R\mathrm{d}U \tag{3.22}$$

in which $J_U(R,U)$ represents the current density per unit of energy. Assuming the distribution in U is Gaussian and the distribution in R is uniform, $J_U(R,U)$ can be written as

$$J_U(R,U) = \begin{cases} J_N e^{-\frac{(U-U_0)^2}{2\sigma_U^2}} & R \leq r_L \\ 0 & R > r_L \end{cases} \tag{3.23}$$

with σ_U the RMS spread in energy and J_N a normalization constant. This J_N can be calculated by integrating equation 3.23 over all positions and energies and equating the result to the total current I, so

$$J_N = I\left(\int_0^\infty \int_0^{r_L} e^{-\frac{(U-U_0)^2}{2\sigma_U^2}}\,\mathrm{d}R\mathrm{d}U\right)^{-1} = \sqrt{\frac{2}{\pi^3}}\frac{I}{\sigma_U r_L^2 \left(1 + erf\left(\frac{U_0}{\sqrt{2}\sigma_U}\right)\right)}. \tag{3.24}$$

When equations 3.21-3.23 are combined and the kinetic energy is written in terms of a dimensionless energy $U' = \frac{U-U_0}{U_0}$, dI can be written as

$$\mathrm{d}I = 2\pi r J_N \frac{f^2}{C_c^2}\frac{U_0}{U'^2}e^{-\frac{U_0^2 U'^2}{2\sigma_U^2}}\,\mathrm{d}r\mathrm{d}U'. \tag{3.25}$$

From this equation $J_U(r,U')$ can be extracted. To calculate the current density $J_U(r,U')$ has to be integrated over all possible U'. This is not simply from minus one to infinity, because the kinetic energy of the ions that are at a position r in the Gaussian image plane is limited by the fact that R is limited due to the aperture. Since $R \leq r_L$, equation 3.21 leads to $|U'| \geq \frac{fr}{C_c r_L}$. Therefore the current density in the Gaussian image plane is given by

$$J(r) = \int_{-1}^{-\frac{fr}{C_c A_L}} J_U(r,U')\,\mathrm{d}U' + \int_{\frac{fr}{C_c A_L}}^{\infty} J_U(r,U')\,\mathrm{d}U' \tag{3.26}$$

with

$$J_U(r,U') = J_N\frac{f^2}{C_c^2}\frac{U_0}{U'^2}e^{-\frac{U_0^2 U'^2}{2\sigma_U^2}}. \tag{3.27}$$

The integrals in equation 3.26 can be solved analytically but lead to very large expressions which are not displayed here. A plot of the current density is shown in figure 3.4a.

Figure 3.4b shows a plot of the fraction of current as a function of the radius. It is very hard to obtain an analytical equation for the fraction of current. Therefore it is obtained by numerically integrating the solution of equation 3.26. From plots of the fraction of current it
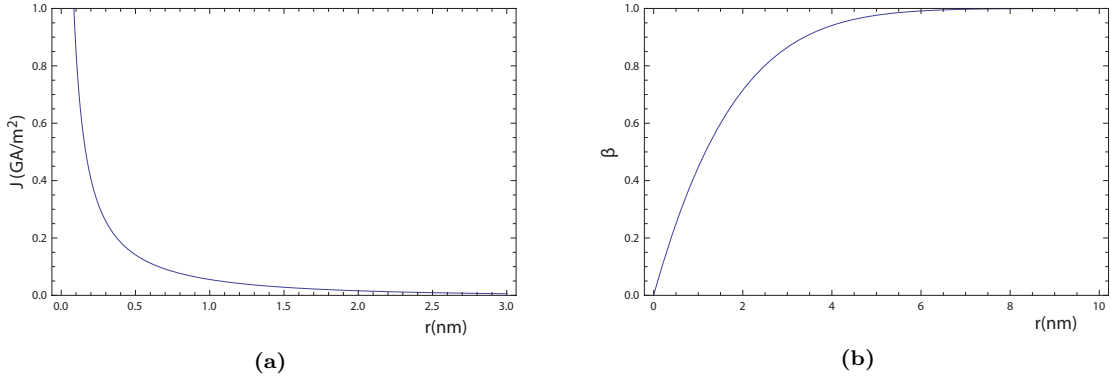
Figure 3.4 Plots of (a) the current density and (b) the fraction of current as a function of the radial position for $C_C = 20$ mm, $f = 6.5$ mm, $U_0 = 30$ keV, $\sigma_U = 1$ eV, $J_s = 10.91$ A $\cdot$ m^{-2}, $I = 1$ nA $L = 10$ cm and $f_A = -2.4$ cm.

was however possible to obtain an equation for the diameter d_{50} which includes 50 percent of the current:

$$d_{50,C} = 0.811 \cdot C_C \frac{\sigma_U}{U_0} \frac{r_L}{f} \tag{3.28}$$

This section showed a derivation of the chromatic aberration limited probe size for a uniform current density at the lens. The derivation for a Gaussian current density can be done in a similar way, but is not shown in this report since in the ABLIS setup the current density can be approximated uniform for most values of the current.

3.5 Aberration constants

The previous two sections were devoted to the contributions to the spot size of the spherical and chromatic aberration. But before we can quantitatively investigate these contributions and compare them with the brightness limited spot size, the aberration constants C_S and C_C have to be known. To find these constants the electric field lens, which will be used in the ABLIS setup in the future, was implemented in the GPT code. By comparing the RMS spot sizes that are then obtained in the image plane with their theoretical values, the aberration constants can be obtained.

The information about the lens was provided by Sander Henstra from FEI Company. The lens actually consists of two separate structures, the condenser lens and the objective lens. When entering the lens column the ion beam will be slightly divergent, due to the Coulomb expansion and the exit kick of the accelerator. The condenser lens aims to collimate this divergent ion beam after which the objective lens focuses it to a small spot. Therefore most of the aberrations will be caused by the objective lens, since it does most of the work. The electric field profiles used in the simulation are an off-axis expansion to the 4th order of a number of Gaussians fits through the on-axis ($x = y = 0$) field-profile [39].

In order to find the spherical aberration constant, a beam was simulated with infinite brightness and no energy spread. To make sure that no stochastic heating effects are playing a role, a GPT routine was used without inter-particle interactions. In this way the only contributions to the spot size are geometrical aberrations, from which spherical aberration is by far the most important one. Theoretically the RMS size of a spherical aberration limited beam in the waist is given by [38]

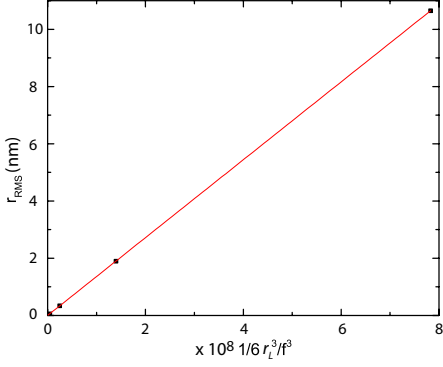$$r_{RMS,S} = \frac{1}{6} C_S \frac{r_L^3}{f^3}, \tag{3.29}$$

Figure 3.5 A plot of the rms size of a spherical aberration limited beam. The slope of this figure is equal to the spherical aberration constant.
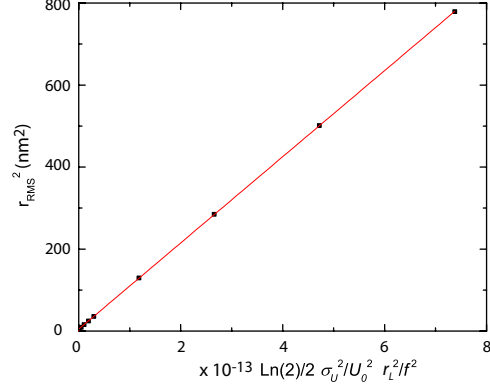

Figure 3.6 A plot of the rms size of a chromatic aberration limited beam. The slope of this figure is equal to the chromatic aberration constant.

which is, apart from a numerical factor, equivalent to equation 3.20. The value of r_L was varied in the range between 5-50 μm, resulting in the plot in figure 3.5. From this plot the spherical aberration constant was determined to be (136±1) mm.

To find the chromatic aberration constant almost the same simulation was run, but now with a Gaussian energy distribution with a RMS width σ_U. However, in GPT a velocity distribution has to be defined instead of an energy distribution. Therefore the energy distribution is transformed to a velocity distribution:

$$
\begin{aligned}
f\left(E\right)dE &= \exp\left(-\frac{(U-U_0)^2}{\sigma_U^2}\right)\mathrm{d}E \\
&= mv\exp\left(-\frac{\frac{1}{4}\left(v^2-v_0^2\right)^2}{2\frac{\sigma_U^2}{m^2}}\right)\mathrm{d}v \\
&\approx mv_0\exp\left(-\frac{(v-v_0)^2}{2\frac{\sigma_U^2}{m^2v_0^2}}\right)\mathrm{d}v.
\end{aligned}
\tag{3.30}
$$

From the second to the third line, the approximation is made that when $|v - v_0| \ll v_0$, $v^2 - v_0^2 = (v - v_0)(v + v_0) \approx (v - v_0)2v_0$. By doing this approximation it was possible to use the built-in GPT Gaussian distribution.

Theoretically the RMS size of a spherical and chromatic aberration limited beam in the waist is given by [38]

$$
r_{RMS}^2 = \frac{1}{36}C_S^2\frac{r_L^6}{f^6} + \frac{\ln 2}{2}C_C^2\frac{\sigma_U^2}{U_0^2}\frac{r_L^2}{f^2},
\tag{3.31}
$$

of which the second part is equivalent to equation 3.28 apart from a numerical factor . To find the chromatic aberration constant, σ_U was varied while leaving the other parameters constant, which resulted in the plot in figure 3.6. The square root of the slope of this plot is equal to the chromatic aberration constant, which was determined to be (32±1) mm.

3.6   Total probe size

The preceding sections were devoted to the individual contributions to the ion probe: the brightness limited probe size and the probe sizes due to spherical and chromatic aberration. Mathematically, the current density in the observation plane is a convolution of the the

current densities of the individual contributions [38]. However, due to the very extended equations it is much easier to apply a so called root power sum (RPS) algorithm. Other research [40] showed that for ion sources with a Gaussian current density, Gaussian energy distribution and uniform angular distribution the total probe size $d_{50,T}$ can be approximated by

$$d_{50,T} \approx \left(\left(d_{50,S}^{1.3} + d_{50,B}^{1.3} \right)^{\frac{2}{1.3}} + d_{50,C}^2 \right)^{\frac{1}{2}}, \tag{3.32}$$

with $d_{50,T}$ the total probe size (diameter) containing 50 percent of the current. Since the ABLIS setup has a more or less uniform current density, it is not known whether this equation is the right RPS algorithm. However, reasonable assumptions can be made for the upper and lower limit of the total probe size. For the upper limit, simply the sum of the contributions (RPS with factor 1) can be taken and for the lower limit the largest contribution can be taken as the total size (RPS with factor ∞).

In designing the ABLIS the total probe size $d_{50,T}$ should be minimized. Very important in this minimization is the parameter $\kappa = \frac{r_L}{f}$, commonly known as the numerical aperture. Equation 3.14 shows that the brightness limited probe size is inversely proportional with this factor, while equations 3.20 and 3.28 show that the spherical and chromatic aberrations are proportional with κ. This means there exists an optimum κ that leads to a minimum probe size.

The brightness limited spot size calculated in section 3.2 is only valid under the assumption of no disorder-induced heating. Therefore it is only possible to calculate probe sizes for currents in the pencil beam regime. As was explained in section 2.2.2, the current to which the pencil beam regime reaches is determined by the electric field strength and the flux density. From equation 2.57 and figure 2.8b the electric field to reasonably suppress disorder-induced heating at a flux density of 10^{20} m^{-2}s^{-1} is determined at

$$E = \left(\frac{\alpha I}{2^{\frac{1}{5}}} \right)^{\frac{5}{2}}, \tag{3.33}$$

in which α is a constant with a value of 10^{13} V$^{\frac{2}{5}}$m$^{-\frac{2}{5}}$A^{-1}. The factor in the denominator is due to the fact that the simulations shown in figure 2.8b are performed for a current density of $5 \cdot 10^{19}$ m^{-2}s^{-1} instead of 10^{20} m^{-2}s^{-1}. As explained in the Introduction this electric field strength determines, together with the size of the ionization laser beam, the energy spread of the ion beam (see equation 1.6).

Now the electric field strength to suppress disorder-induced heating is known it is possible to optimize the total spot size in terms of κ. The optimization of equation 3.32 is too complicated to do analytically. Therefore the spherical and chromatic aberration limited spot sizes are found separately. This is done by leaving out one of the two contributions ($d_{50,S}$ or $d_{50,C}$). Differentiation of the obtained total spot size to κ and equating this derivative to zero gives the value of κ for which the spot size is minimal. Inserting this value back in equation 3.32 gives the spherical/chromatic aberration limited spot size. Figure 3.7 shows a plot of both spot sizes as a function of the current. These two lines give the lower limit of the spot size, but they are also a good approximation of the actual value. The chromatic aberration limited spot size is calculated for a RMS laser width σ_L of 3 μm. Research on a similar subject showed that practical realization of this laser width is possible [41].

As a an example of the optimization process, figure 3.8 shows the spot size at a current of 1 pA as a function of κ. It shows the individual contributions to the ABLIS probe size as well as an estimation of the total probe size given by equation 3.32. It can be seen that the optimum of the beam at this current is limited by spherical aberration and the brightness. A 50 percent spot size of $\approx$0.2 nm can be achieved with a value of κ of $\approx$0.0014. To achieve this value of $\kappa = \frac{r_a(L+f_a)}{f f_a}$ the beam either has to have a very large divergence after the accelerator (f_a very small) or the length of the setup must be several meters. This is however not very suitable for future commercial devices. The length of the total setup should not be
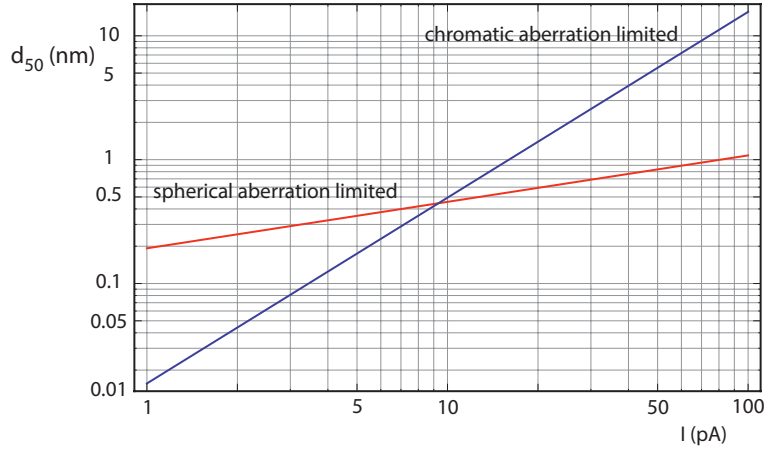
42

Figure 3.7 Plot of the spherical and chromatic aberration limited spot sizes as a function of current. Before the two plots cross each other the spot size of the ABLIS FIB is given by the spherical aberration limited spot size and after the crossing the chromatic aberration determines the spot size.

longer then $\approx$ 1m. With this in mind General Particle Tracing simulations of the complete beam line have been performed at the CQT group with the constraint of a drift length of maximal 20 cm long [39]. These simulations showed that a spot size of $\approx$ 1 nm is possible at 1 pA.

3.7 Optimization of the beamline

As was analytically shown in the previous section, it is possible to reach a spot size of only 0.2 nm at a current of 1 pA. With the current design and the design constraints it is however not possible to do this, since the beam line should then be several meters long. A solution to this problem can be to add an extra element to the setup. This element should diverge the beam so that r_L can become larger and so can κ. As a proof of concept, a GPT simulation was performed of the full ion beam line, stretching from the ionization laser to the target. In this simulation an Einzel lens was placed just after the post acceleration stage. A schematic view of the simulated beam line is shown in figure 3.9a.

An Einzel lens consists of three plates with a hole in it, placed a certain distance from each other longitudinally [35]. The middle of these plates is set at a lower voltage than the other two. In the simulation the outer two plates are set at 30 kV and the middle somewhat arbitrarily at 1.5 kV. The distance between the plates was 2 cm. These parameters together with the drift length are chosen such that the size of the beam at the last lens r_L is at its theoretical optimum (this optimum size can be calculated from the value of κ that gives the minimum in figure 3.8). Figures 3.9b and c show the simulation result. The beam is created (ionized) at $z =$-35 cm, from which it is accelerated in an electric field of 50 kV/m towards $z =$-34 cm. At that point the beam enters the post accelerator which accelerates the ions to 30 keV and stretches up to $z =$-24 cm. At this position the first plate of the Einzel lens is placed. After the Einzel lens the beam drifts to the lens column which starts at $z =$0 cm. In this column two lenses are present. The first one is the so called condenser lens which collimates the beam. After this first lens the beam drifts towards the last lens which focuses the beam to its final spot size. Figure 3.9c shows the spot size that can be reached, which is $\approx$0.2 nm. The result is in good agreement with the analytical estimation shown in figure 3.7.

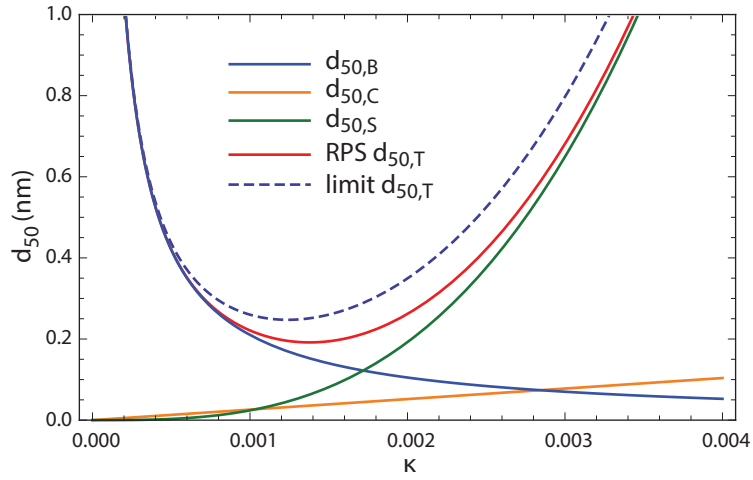The fivefold improvement of the spot size shows the necessity of the extra lens. Due to the

43

Figure 3.8 A plot of the individual contributions to the probe size and the total probe size using the RPS algorithm from [40] as well as an upper limit of the probe size as a function of the parameter κ. For this plot: $I = 1$ pA, $C_C = 32$ mm and $C_S = 136$ mm.

lens, the spot size can become much smaller while staying within the length requirements of the setup. However, before we can conclude this spot size is possible with the ABLIS setup, it needs to be said that it is not known how physically realizable the Einzel lens construction implemented in the simulation is. The electric fields implemented in the simulation are created by infinitely thin plates with a perfectly circular hole. Simulations of what the effect of a real lens will be on the ion beam should be performed in the future. But the expectation is that aberrations of this lens will not play significant a role in the final probe size, since it may focus the ions much less extreme then the final lens. Therefore, the most important conclusion of this chapter is the fact that a spot size of only 0.2 nm is within reach of an ABLIS-based FIB at 1 pA.
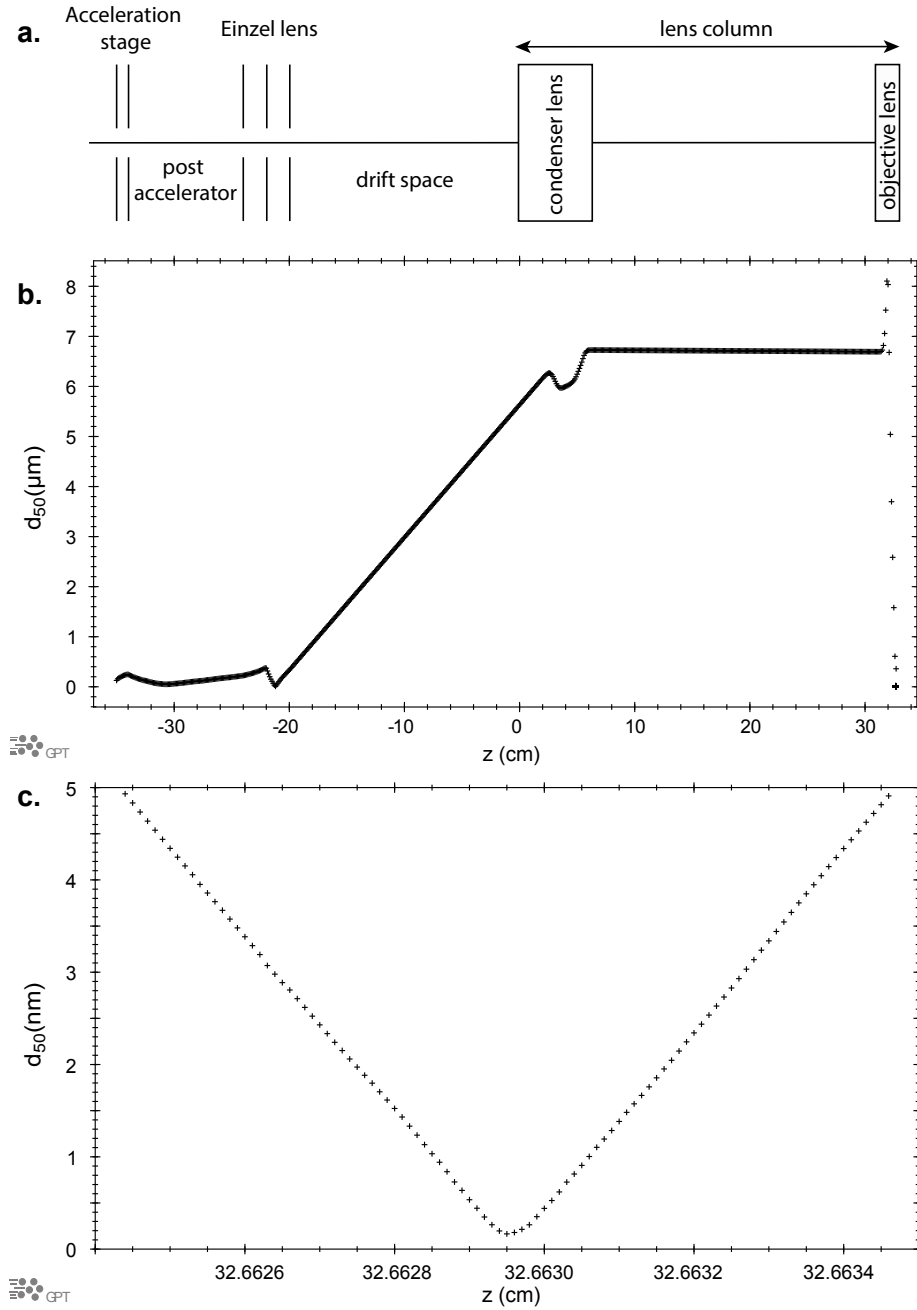
Figure 3.9 a. Schematic overview of the ion beam line used in the GPT simulation. **b.** Result of the GPT simulation of the complete ion beam line, including the added Einzel lens. It shows the diameter containing 50 percent of the current as a function of the longitudinal position over the complete longitudinal range. **c.** Same simulation result as b but zoomed in on the waist of the beam.

Chapter 3 Probe size contributions

Chapter 4

Laser system

The fact that the ABLIS FIB is created from ultracold atoms distinguishes it from other FIB sources. Therefore the laser cooling and compression stage is an essential part of the ABLIS setup. It consists of two main components; the magnetic field gradient and the radiation field, which are both used to compress the beam to the center of the beam line as explained in the Introduction. The magnetic gradient will be custom made, but is outside the scope of this report. We'll focus on the radiation field which, besides compressing the beam, also aims to cool the atoms down to less then a milliKelvin.

For the laser cooling and compression to be successful, the laser field has to have a precise and stable frequency. As explained in the Introduction, a slight deviation from the optimal detuning can cause a large decrease in brightness. Therefore the laser frequency must be accurate and stable within $\sim 0.05\gamma$, which is approximately 300 kHz [22]. This means the average frequency has to be accurate within this range, but the frequency fluctuations have to be smaller then 300 kHz as well. In previous work [22], a stable laser frequency has already been realized. The average fluctuations were smaller than 20 kHz with incidental spikes of ~100 kHz. Besides that, a method based on the Zeeman shift of atoms in a magnetic field was tested in order to set the detuning. However, this method appeared to be unreliable and another method incorporating the use of two acousto-optic modulators (AOMs) was suggested. Section 4.1.3 takes off from here and discusses a method to accurately set the detuning.

Another essential element of laser cooling and trapping is the repump beam. Recall from the Introduction that this beam is needed due to the lack of a closed transition in rubidium. It has to be shifted +2915 MHz from the trapping laser (see figure 1.3). Since the probability that the atom falls back to the wrong ground state is rather low, the intensity of the repump beam is allowed be much less than that of the trapping laser ($< 10\%$). Section 4.1.4 discusses the creation of the repump beam with an electro-optic modulator (EOM).

Besides creating the desired characteristics of the laser such as detuning, stability and the presence of the repump beam, a side target of the laser setup is to be robust and compact so that future ABLIS based FIBs can be equipped with a similar system. Where possible, the number of elements in the setup and their complexity are therefore minimized.

4.1 Laser

4.1.1 Titanium:Sapphire Ring Laser

The laser used to create the light field for the laser cooling and trapping is a Titanium:Sapphire laser[1]. The gain medium in this type of lasers is a sapphire crystal doped with titanium. Due to the broad gain bandwidth it can be tuned over a wide range of wavelengths, for example

---

[1]Coherent 899-21 Titanium:Sapphire Ring Laser by Coherent Inc.

to the 780 nm of the $5S_{1/2}F = 3 \rightarrow 5P_{3/2}F' = 4$ transition. The crystal is excited with a diode-pumped semiconductor laser[2]. Besides the crystal the laser system contains several optical components to ensure single-mode emission of light. The Titanium:Sapphire laser was chosen since it was already present and installed in the lab at the start of the ABLIS research. Another, more compact, solution would be a diode or a fiber laser.

The longitudinal modes of a laser are determined by the optical path length in its cavity. To positively interfere with itself, the total phase shift after one pass through the ring cavity must be a multiple of 2π. This conditions leads to the fact that longitudinal modes only exist with a frequency ω given by [42]

$$\omega = n\frac{c}{L_{optical}},\tag{4.1}$$

in which n is a positive integer number, c is the speed of light and $L_{optical}$ is the optical path length in the cavity. Thus by tuning the optical path length of the cavity, the frequency of the nth mode can be altered. Single-mode lasing can be achieved when only one of the many longitudinal modes comes above the so called lasing threshold due to the gain of the total cavity, see figure 4.2.

Figure 4.2 shows the transmission of the different optical components in the Titanium:Sapphire laser as a function of the frequency. A broad bandwidth filter is already present due to the gain of the crystal and the reflectance of the mirrors. The birefringent filter is narrower; it consists of a wavelength dependent birefringent crystal, which changes the polarization as a function of the wavelength. It can be used to approach the desired frequency, but single-mode lasing can only be achieved with the addition of two etalons, which are called the 'thick' and 'thin' etalon. These names refer to their length, which determines their bandwidth; the thick etalon having a smaller bandwidth. When the transmission maxima of all components overlap and in addition this maximum also overlaps approximately with a single longitudinal mode of the laser, single-mode lasing can be achieved. To prevent standing wave patterns in the gain medium, which can cause multi-mode lasing, an optical diode is placed, due to which the light in the ring cavity can only travel in one direction.

The frequency of the laser is tuned by two components [43]. The first one is a 'tweeter' mirror which accounts for fast cavity length variations. The other one is a rotating Brewster plate driven by a galvanometer. Together with an internal cavity, these active controls narrow the bandwidth to 500 kHz. However, to absolutely lock the laser to a certain transition frequency of rubidium an external spectroscopy setup is needed, which is described in section 4.1.3.

A block scheme of the full laser setup is shown in figure 4.1. Light from the laser is sent to the spectroscopy setup which creates an error signal. This signal contains information about the frequency of the laser that can only be obtained with the use of some mixing electronics. This error signal is supplied to a PID controller which is connected back to the laser.

4.1.2 Modulation techniques

Electro- and acousto-optic modulators play an important role in the laser setup, because they can adjust the frequency of the light. Two EOMs are used; the first one for the creation of the repump beam and the second for the generation of sidebands inside the spectroscopy setup. An AOM is used to set the detuning of the laser, which will be explained in section 4.1.3. So before the setup is explained in more detail, the basics of EOMs and AOMs are explained.

Electro-optic modulation

An EOM can be used to control the amplitude or phase of a light field [42]. It mainly consists of an electro-optic material embedded between two electrodes over which a certain
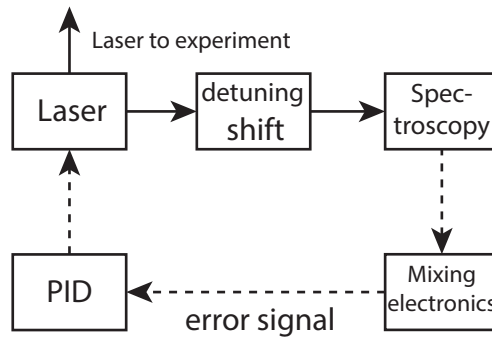
---

[2]Verdi V18 by Coherent Inc.

Figure 4.1 A block scheme of the laser setup. Solid arrows represent laser light and dotted arrows electric connections. Light from the laser is stabilized in a spectroscopy setup by making use of a rubidium vapor cell. Some mixing electronics are needed to get an error signal from the spectroscopy setup. This error signal is sent to the PID controller which controls the laser frequency. To set the detuning of the laser beam, additional elements are placed in the beam line in order to shift the laser frequency.
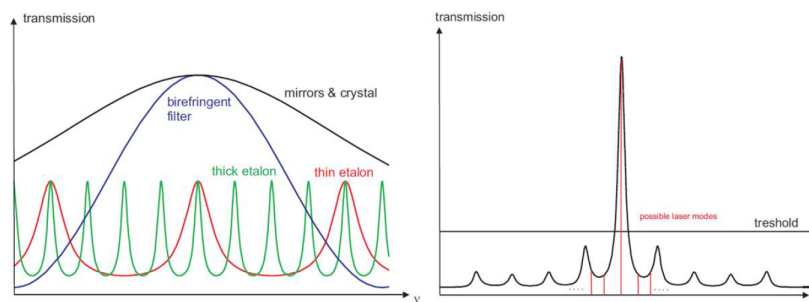
Figure 4.2 Left The transmission of all optical components in the laser as a function of the frequency ν. **Right** Transmission of the full laser cavity. Only one longitudinal mode will have a large enough transmission to overcome the lasing threshold and single-mode lasing will be achieved. This figure has been taken from [44].

voltage is applied. Due to the electric field between the electrodes the refractive index of the electro-optic crystal changes. The refractive index can either be linearly dependent on the electric field, which is called the Pockels effect, or quadratically dependent, which is called the Kerr effect. Both EOMs in the ABLIS setup are based on the Pockels effect.

When a sinusoidal voltage is applied to the crystal, the refractive index n can be written as

$$n(t) = n_0 + \alpha V_a \sin(\omega_{FM} t), \tag{4.2}$$

in which n_0 is the refractive index of the crystal without an electric field, α is a material constant, V_a is the amplitude of the applied voltage and ω_{FM} is the frequency of the applied field. This refractive index determines the phase of the light after passing through the EOM. After passing through the EOM, the electric field E_L of the light can be written as

$$E_L(t) = E_0 \sin(\omega t + \beta V_a \sin(\omega_{FM} t)), \tag{4.3}$$

in which E_0 is the amplitude of the electric field of the light and β is the so called modulation depth which is proportional to the before mentioned α. The modulation depth gives the phase change of the light per volt which is applied over the crystal. An electric field with a harmonic modulation of the phase can also be written as an infinite series of Bessel functions of the first kind $J_i(\beta V_a)$ multiplied by each harmonic of the phase modulation [45]

$$E_L(t) = E_0 J_0(\beta V_a) \sin(\omega t) + E_0 \sum_{n=1}^{\infty} J_n(\beta V_a) \left[\sin(\omega t + n\omega_{FM} t) + (-1)^n \sin(\omega t - n\omega_{FM} t) \right]. \tag{4.4}$$

This equation shows that by frequency modulating a laser beam with an EOM, sidebands are created which are shifted by an amount $n\omega_{FM}$ in the frequency domain, in which n is the order of the sideband, which can be positive or negative. The intensity of these sidebands is proportional to the square of the nth order Bessel function of the first kind, with the modulation depth multiplied with the applied voltage as the argument. When filling in approximations of the Bessel functions, the relative intensity of the first order sideband with respect to the zeroth order can be written as

$$\frac{I_1}{I_0} \approx \frac{\left(\frac{\beta V_a}{2} - \frac{(\beta V a)^3}{16} \right)^2}{\left(1 - \frac{(\beta V_a)^2}{4} \right)^2}. \tag{4.5}$$

Acousto-optic modulation

In an AOM the light is modulated by making use of an acoustic wave that is sent through an optical medium [42]. Due to this acoustic wave the spatial distribution in the material, and therefore also the index of refraction, is altered periodically. This periodic variation will act as a diffraction grating with a grating distance Λ given by

$$\Lambda = \frac{v_s}{f_s}, \tag{4.6}$$

in which v_s is the speed of light in the optical material and f_s is the frequency of the acoustic wave. The angles θ which a diffracted light beam of order n makes with the normal can be calculated with the so called Bragg condition

$$\sin\theta = \pm\frac{n\lambda}{2\Lambda}. \tag{4.7}$$

Since the light is diffracted from a plane that is moving with the speed of sound in the optical material, the diffracted light will experience a Doppler shift. This Doppler shift causes the
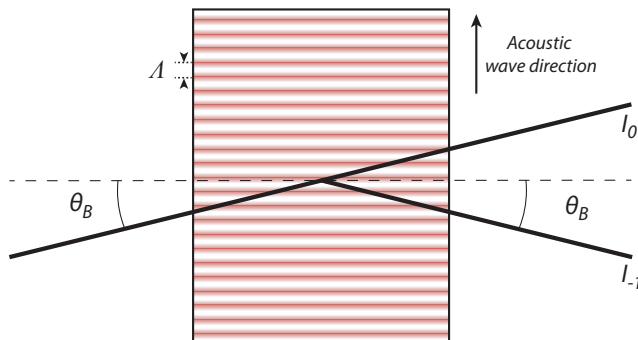
Figure 4.3 AOM configuration in the Bragg regime in which the incident beam as well as the first diffracted order make an angle θ_B with the normal of the AOM. When the (transverse part of the) incident light beam travels in the same direction as the acoustic wave, most of the light will be in the minus first order, which is frequency shifted an amount $-f_s$.

frequency in the first order diffracted beam to shift an amount f_s. An AOM can thus be used as a frequency shifter like an EOM, but an AOM also spatially separates the frequency shifted beams.

AOMs can be separated into two regimes [46]; those for which $Q \ll 1$ and those for which $Q \gg 1$, where Q is given by

$$Q = \frac{2\pi\lambda L f_s^2}{n v_s^2}, \tag{4.8}$$

in which λ is the wavelength of the light and L is the length of the crystal. The AOM in the ABLIS setup is in the so called Bragg regime for which $Q \gg 1$. In this regime, a very large fraction of the light can be transferred to the first order. This happens when both the incident light beam as well as the first order diffracted beam make an angle $\theta_B \approx \frac{\lambda}{2\Lambda}$ with the normal, see figure 4.3.

An important feature of an AOM is the fact that the amount of diffracted light is dependent on the acoustic power; a larger acoustic power will lead to more diffracted light. Therefore an AOM can also be used to actively control the intensity of a laser beam.

4.1.3 Stabilization and Detuning

This section is dedicated to methods to stabilize and detune the laser frequency. In the first part a brief description is given of the spectroscopy methods used. In the second part a new method to set the detuning and its setup are proposed. The third part shows the results of detuning and stability measurements with this new setup.

Spectroscopy methods

In previous research [22] two methods to stabilize the laser frequency were described, one of which was frequency modulation (FM) spectroscopy and the other modulation transfer (MT) spectroscopy. Both methods were explained in much detail. Therefore, only the basic features of FM spectroscopy are repeated here. MT spectroscopy is not treated, since it is not of large significance for the research described in this report.
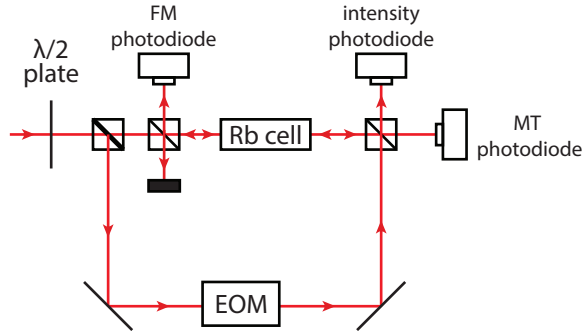
Figure 4.4 Schematic diagram of the spectroscopy setup. Two counter propagating laser beams travel through a rubidium vapor cell. On of these contains sidebands created with the EOM. The spectroscopy signal are obtained with the FM and MT photodiode. The intensity photodiode is used to measure the intensity in the setup. Its signal is used to stabilize this intensity.

The goal of both aforementioned spectroscopy methods is to obtain an error signal as a function of the laser frequency which can be fed back to the laser to actively control the frequency. This error signal, also called a dispersion signal, must be linear and antisymmetric around the desired frequency. It is measured and used as input of a PID controller [3], which produces a feedback voltage which is fed back to the laser to control its active elements (tweeter mirror and rotating Brewster plate).

To produce the dispersion signals in both of the spectroscopy methods a so called saturated absorption spectroscopy setup is used in combination with an EOM which is driven at 6.8 MHz. The saturated absorption setup is shown in figure 4.4. In this setup, two counter propagating laser beams travel through a cell filled with rubidium vapor. One of these beams has traveled through the EOM before entering the vapor cell. Therefore it contains 6.8 MHz shifted sidebands. FM spectroscopy is based on the fact that these sidebands have a different absorption coefficient than the main band, because of their slightly shifted frequency. One can show that the intensity I_{abs} absorbed by the vapor cell contains a term proportional to $\cos{(\omega_{FM}t)}$, which has an amplitude that is proportional to the difference between the absorption of the first order sideband and minus first order sideband [47]. This part of the intensity constitutes the dispersion signal. It can be measured by measuring the transmitted light with the FM photodiode, shown in figure 4.4. When this photodiode signal is multiplied electrically with a harmonic signal with the same frequency ω_{FM} and the same phase, the required dispersion signal is obtained.

Figure 4.5 shows the dispersion signal as a function of the laser frequency for FM spectroscopy as well as for MT spectroscopy. It reveals the reason for the use of the saturated absorption setup. In normal absorption spectroscopy just a single laser beam is sent through the vapor cell. Since the atoms in the vapor cell all move with a different velocity, the absorption signals obtained in this manner are much broader then the natural linewidth of the transition (≈ 6 MHz for ^{85}Rb $F = 3 \rightarrow F' = 4$) due to Doppler broadening. This is overcome with saturated absorption spectroscopy, in which a second beam is sent through the vapor cell as well. For most atoms this has no effect, since the Doppler shift of both of the laser beams will be different; an atom with a certain velocity not close to zero cannot absorb photons from both beams. Only the population of atoms that have a velocity of nearly zero can be excited by both beams, since they do not suffer from the Doppler effect. This means that one of the beams saturates the atom population with small velocities for the other beam. Therefore, signals obtained in a saturated absorption setup contain features which are not Doppler broadened. For the FM spectrum this means that the widths of the
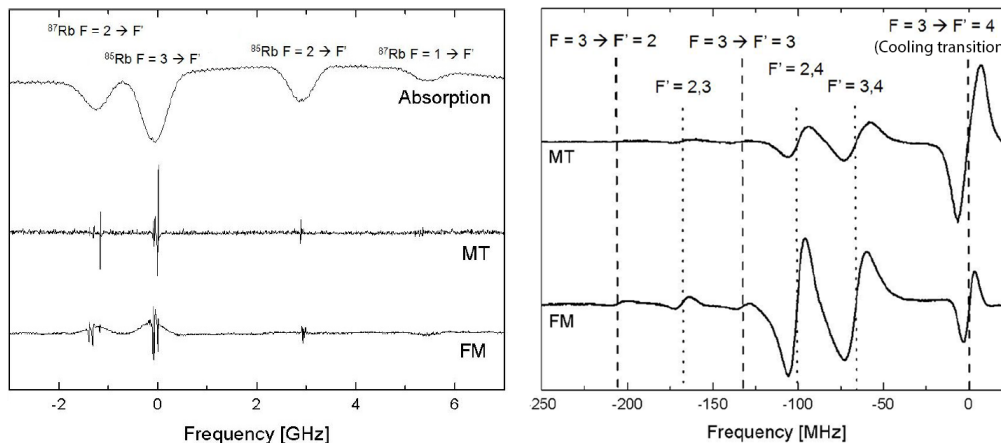
---

[3]Laselock, from Toptica Photonics

Figure 4.5 Left The normal absorption signal, FM spectroscopy signal and MT spectroscopy signal as a function of the laser frequency. The absorption signal shows four dips, two different transitions for each rubidium isotope (mass number 85 and 87). **Right** The FM and MT spectrum zoomed in to the region near the ^{85}Rb $5S_{1/2}F = 3 \rightarrow 5P_{3/2}F' = 4$ transition (most right). The FM spectrum shows two other large dispersion signals, which are so called crossover transitions (labeled by the two hyperfine levels due to which they are caused). Both figures are taken from [22]

dispersion signals are of the order of the linewidth of the transitions, although the spectrum does suffer from a Doppler broadened background. The reason for this Doppler broadened background is not known.

A common feature in all forms of saturated absorption spectroscopy is the appearance of crossover transitions in the measured spectra. These additional dispersion signals appear due to the fact that an atom with a certain velocity $\pm v_{//}$ in the direction of the laser beams can be at resonance with one transition in one of the laser beams while also being at resonance with an other transition in the other beam. These crossover transitions are clearly visible in the spectra shown in figure 4.5, they are indicated with the two hyperfine levels to which the beams excited the atom. The Doppler shifted frequency ω_1 the atom experiences from one laser beam can be written as

$$\omega_1 = \omega + v_{//}k, \tag{4.9}$$

in which $k = \lambda/(2\pi)$ is the wave vector of the laser beam. Simultaneously the Doppler shifted frequency ω_2 the atom experiences from the other laser beam is given by

$$\omega_2 = \omega - v_{//}k. \tag{4.10}$$

Solving these two equations for ω leads to

$$\omega = \omega_{co} = \frac{\omega_1 + \omega_2}{2}, \tag{4.11}$$

in which the symbol ω_{co} is assigned to the frequency of the crossover transition, which is exactly in the middle between every two transitions in the rubidium spectrum. The frequency difference between the $5^2S_{1/2}$ $F = 3 \rightarrow 5^2P_{3/2}$ $F = 4$ transition and $5^2S_{1/2}$ $F = 3 \rightarrow 5^2P_{3/2}$ $F = 2$ transition is for example 184 MHz [48], which means the $F' = 2, 4$ (in which F' denotes the quantum number F of the excited states) crossover transition should be 92 MHz shifted from the cooling transition.

Detuning method and setup

To test the methods to stabilize and detune the laser, a frequency metrology setup is used to accurately measure the laser frequency. In this setup a second laser is used which
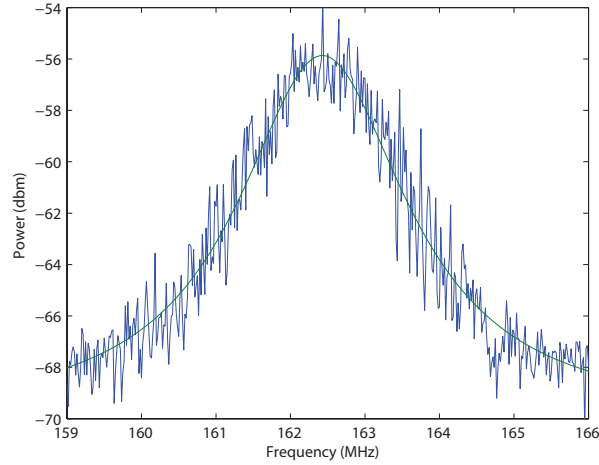
Figure 4.6 Example of a beat note spectrum measured with the spectrum analyzer, the data was fit with a Lorentzian function.

was already present in the lab. This laser is locked to the ^{8}5Rb $F = 3 \rightarrow F' = 4$ transition by MT spectroscopy, but is shifted -160 MHz by using an AOM. A beat note is created of the two lasers by spatially overlapping them on a photo detector. The result of this action is that the photo detector signal will measure a constant background with harmonic signals on top of it. These harmonic signals oscillate with the sum and difference of the frequencies of the two lasers, a phenomenon also known as heterodyning. This photo detector signal is connected to a spectrum analyzer[4] which measures the power of each frequency component in the signal. The result is a spectrum which shows a peak at the frequency difference of the two lasers, from which the frequency of one of the lasers can be determined absolutely when the frequency of the other is known. This is done by performing a least square fit of the spectrum with a Lorentzian distribution in Matlab. An example of a beat note spectrum including a Lorentzian fit is shown in figure 4.6.

Previous work [22] concluded that detuning the laser frequency by exploiting the Zeeman shift was unreliable. In this method a Zeeman shift was induced in the atoms by applying a magnetic field, which was created with a coil around the vapor cell, through which a variable current was sent. Another method to detune the frequency was proposed, which incorporates the use of two AOMs. As explained in section 4.1.2 an AOM can be used to shift the frequency of a laser beam so it can also be used to detune the laser. It is however not possible to do this by locking the laser at the exact transition frequency and shifting it with a single AOM, since efficient AOMs are not available at frequencies of $\approx$1 MHz. The proposed solution in previous work was to use two AOMs, one to shift the frequency up and one to shift it down again, but to a slightly different frequency. In this way also small detunings are possible. A downside is that the system becomes more difficult to align with the addition of two AOMs.

There is another possibility to set and stabilize the frequency around the ^{85}Rb$F = 3 \rightarrow F' = 4$ transition. This method uses of the crossover transitions in the saturated absorption spectra. Before the laser enters the spectroscopy setup it is sent through an AOM twice, which shifts the frequency with an amount $2\omega_{AOM}$. Then the frequency-shifted laser is locked at one of the crossover transitions which is shifted an amount ω_{co} from the ^{85}Rb $F = 3 \rightarrow F' = 4$ transition. In this way the detuning δ of the laser is given by

$$\delta = \omega_{co} + 2\omega_{AOM}. \tag{4.12}$$

This equation shows that with this method the detuning can be set by the frequency of the
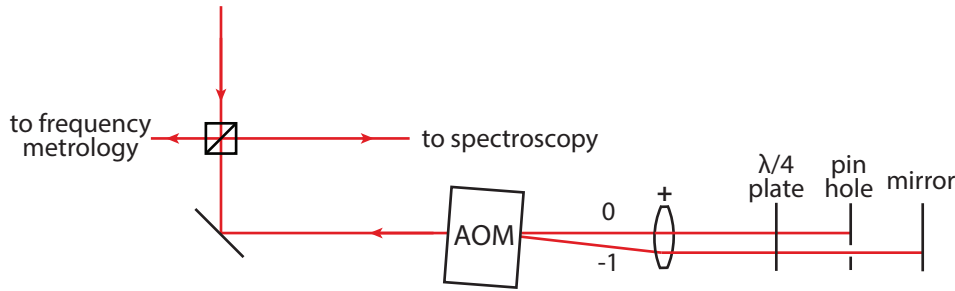
---

[4]Rigol DSA 815) (1.5 GHz)

Figure 4.7 The double pass AOM configuration that is used in the laser setup.

AOM, with the additional advantage that only one AOM is needed. This makes the system easier to align and makes it more compact.

A downside of using an AOM to shift the frequency is the fact that the angle under which the first order beam is diffracted, is dependent on the frequency at which the AOM is driven. This makes a single pass AOM configuration very impractical due to alignment issues. A common method to avoid this problem is to use a double pass AOM configuration which is shown in figure 4.7. In this configuration the laser goes through the AOM twice. Before the beam reaches the AOM, a combination of a $\lambda/2$ plate and a polarizing beam splitter is used to sent a certain fraction of the light to the frequency metrology setup. The other part of the light is sent to the AOM. After the AOM, a lens is placed at exactly one focal length f. The effect of this lens is that all orders are parallel to eachother afterwards. The beams then pass through a $\lambda/4$ plate whose function is explained later. Finally a pinhole blocks the zeroth order and transmits the (minus) first order, which is reflected back to the AOM and diffracted once more. Since the incoming as well as the (minus) first order refracted beam both make an angle θ_B with the normal of the AOM in the Bragg configuration, the direction of the outgoing beam is independent of the frequency at which the AOM is driven. Finally, the outgoing beam is separated from the incoming beam by the same polarizing beam splitter as before. Since the $\lambda/4$ plate is passed twice the polarization of the outgoing beam is rotated $90°$ with respect to the incoming beam. This causes all of the outgoing beam intensity to travel towards the spectroscopy setup. Of course, the effect of the double pass configuration is also that the frequency of the outgoing beam has shifted $2\omega_{AOM}$ from the frequency of the incoming beam.

To make the laser as stable as possible, the peak to peak amplitude of the dispersion signal has to be as large as possible. Therefore, FM spectroscopy is chosen, since it produces the largest crossover signals near the ^{85}Rb$F = 3 \rightarrow F' = 4$ transition. The largest of these is the $F' = 2, 4$ crossover transition, which is shifted by 92 MHz. In order to reach a detuning between 0 and 2γ, the frequency of the AOM must be between 40 MHz and 46 MHz. These frequencies lie within the range of frequencies for which the AOM in the laser setup[5] is suitable.

The downside of using the FM spectrum is the Doppler broadened background. Due to this background the dispersion signal has a certain offset, which is dependent on the laser intensity. This means that if the laser intensity decreases over time (which can happen because of temperature changes for example) the offset of the dispersion signal drops as well. The PID controller will then adjust the frequency such that the original value is reached again. In other words, the frequency will slightly drift away from the set value.

The disadvantage described above can be circumvented by using the fact that the intensity in the first order beam produced by the AOM is proportional to the AOM input power. Therefore it is possible to control the intensity of the beam that enters the spectroscopy
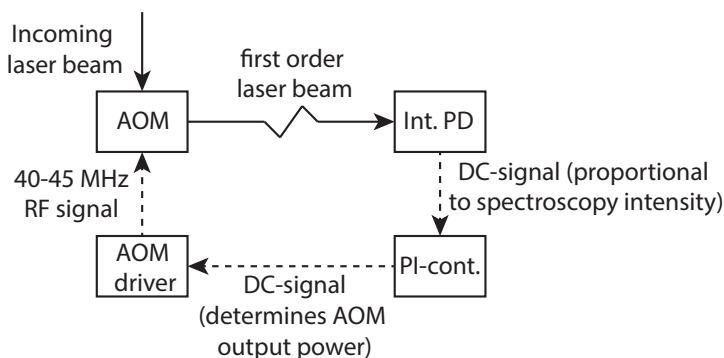
---

[5]IntraAction AOM-40N

Figure 4.8 Schematic view of the Spectroscopy intensity control loop. The first order diffracted beam from the double pass AOM setup is sent to the spectroscopy setup, in which its intensity is measured with the intensity photodiode (see figure 4.4). The photodiode signal is sent to a PI controller that controls the power with which the AOM driver drives the AOM.

setup. In order to do so (a fraction of) this intensity is measured with an extra photodiode in the spectroscopy setup (see figure 4.4). The signal of this photodiode is connected to a home-built PI controller. This controller compares the signal with a set reference value and produces an output signal which is connected to the AOM controller[6] in order to regulate the photodiode signal to the set value. The whole process is schematically shown in figure 4.8.

Detuning and stability measurements

A calibration of the detuning as a function of the AOM frequency, which is done by using the frequency metrology setup, is shown in figure 4.9. The measurement is performed 4 times. In each of these measurements the intensity in the spectroscopy setup was deliberately changed, so that the spectroscopy signal was slightly different. The set point of the PID controller that controls the laser frequency was set to the middle of the dispersion signal manually in each measurement. This was done in order to estimate the error in this process.

It can be seen that the detuning is a linear function of the AOM frequency of which the slope is equal for all measurements. The range over which the frequency can be tuned is good enough for laser cooling experiments. The offset of the different measurements is not the same however. The reason for this variable offset is probably that the set point of one of the lasers was slightly different each time. To overcome this problem, it would be better to leave the set point of the PID controller at the same value all the time. This will only be possible in case the alignment of the spectroscopy setup is exactly the same every time since a slight change in overlap of the two laser beams in the vapor cell will already change the spectroscopy signal. A stable alignment can be achieved by using an optical fiber to transport the laser to the spectroscopy setup. In this way, re-alignment of the optics before the spectroscopy setup (and double pass AOM) will cause less light to be coupled into the fiber, but no deflection of the beam in the spectroscopy setup.

Since new elements (repump EOM and double pass AOM configuration) are added to the spectroscopy setup, a new measurement is performed of the stability of the laser frequency. Figure 4.10 shows the result of this measurement. It shows that over a period of two hours the average frequency of the laser drifts slightly, but well within the performance requirements of 300 kHz. Also the frequency variations are well within the requirements. However, they seem to be larger than before [22]. This comparison is not completely fair however, since a different spectrum analyzer is used to measure the stability.

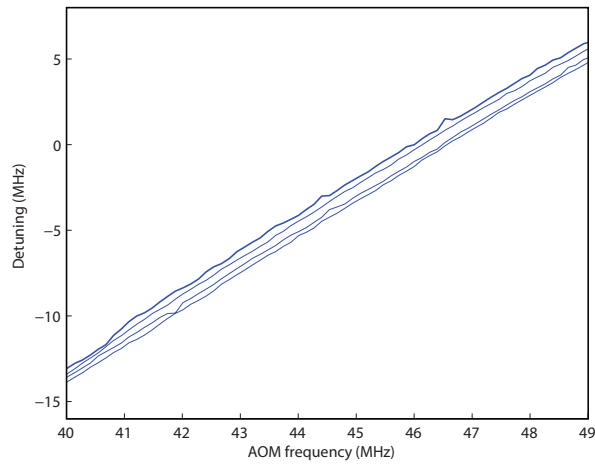[6]IntraAction deflector driver

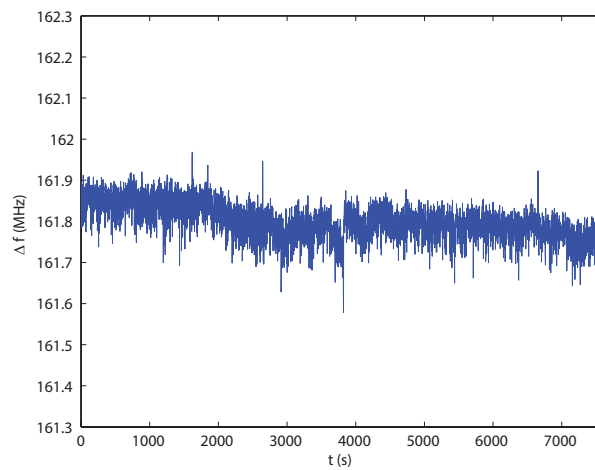**Figure 4.9** A measurement of the detuning as a function of the AOM frequency.

Figure 4.10 A measurement of the stability of the laser frequency.

It can be concluded that the method, in which a double-pass AOM is used and the laser is locked at a crossover transition, works well. The laser can be detuned over the desired range of frequencies and is stable enough to perform laser cooling and trapping experiments.

4.1.4   Repump beam

Now that the laser is stable and can be detuned, the last effort that needs to be done before laser cooling and trapping experiments can be performed is to create the repump beam. The amount of light needed in this repump beam to sufficiently suppress populating the unwanted ground state is not known exactly. The repump beam is needed to depopulate the $F = 2$ ground state, since at the moment the beam enters the laser cooling and compression stage a certain fraction of the population will be in this unwanted ground state. Furthermore, the trapping laser can accidentally excite the atoms to the $F' = 3$ state instead of the $F' = 4$ state (see figure 1.3). However, this will be a very slow process since the energy difference between the two levels is very large compared to the natural linewidth of the transitions. The probability that an atom gets excited to the $F = 3$ excited state is roughly a hundred times as small as that it gets excited to $F = 4$ excited state. Currently, simulations of the laser cooling and compression are being performed at the CQT group, which incorporate the effects of unwanted transitions and the repump beam. The goal of the experiment described here was to create a repump beam with an intensity of at least 10% of the trapping laser, which is expected to be more than enough for the laser cooling and compression to be successful.

An elegant way to create the repump beam is by using an EOM driven at 2915 MHz. In this way sidebands are created which are always exactly at 2915 MHz from the trapping laser. The major advantage of this method is that no extra laser and spectroscopy setup are needed to create this laser beam at its desired frequency. Furthermore the repump beam is automatically overlapping with the trapping beam.

The EOM[7] used, is specifically designed for the purpose of repumping ^{85}Rb. It can be tuned exactly to 2915 MHz in order to minimize the reflected electrical power. A RF function generator was used to create a harmonic signal which was connected to a high power amplifier[8]. To measure the sideband intensity, again a beat note is created of the Ti:Sapph laser and the other laser in the lab. This time the two lasers are inserted in a fiber which is connected to a high speed fiber photodiode[9], capable of measuring high frequency (3 GHz) signals. The photodiode signal is amplified and connected to a high frequency spectrum analyzer[10], which visualizes the sidebands.

Figure 4.11b shows a typical example of a measurement of the sidebands with the spectrum analyzer. For this measurement the Ti:Sapph laser was locked at the ^{85}Rb $F = 3 \to F' = 4$ transition. The largest peak can be seen at ≈ 160 MHz, which is the beat note frequency of the zeroth order beam of the EOM and the other laser. The other two indicated peaks, at $f \approx |160 - 2915| = 2755$ MHz and $f \approx |160 + 2915| = 3075$ MHz account for the the beat note frequencies of the first and minus first order of the EOM with the other laser. The other peaks in the spectrum are due to background noise as shown in Figure 4.11c. Figure 4.11c shows the same spectrum, but now with the laser shifted manually (so not locked) $\approx$2915 MHz. This was done to test whether the bandwidth of the photodiode and amplifier was sufficiently broad so that the zeroth and first order beat note frequencies experienced an equal gain. As can be seen this was clearly not the case since the zeroth order beat note gave a much lower signal when it was shifted. In order to get an accurate measurement of the relative first order sideband intensity as a function of the EOM power, spectra were measured at each power with both, the laser locked at the desired transition and the laser shifted $\approx$2915 MHz. In this way a conversion factor is found between the 160

---

[7]Qubig EO-Rb85-3K
[8]Minicircuits ZHL-16W-43+
[9]Thorlabs FDS02
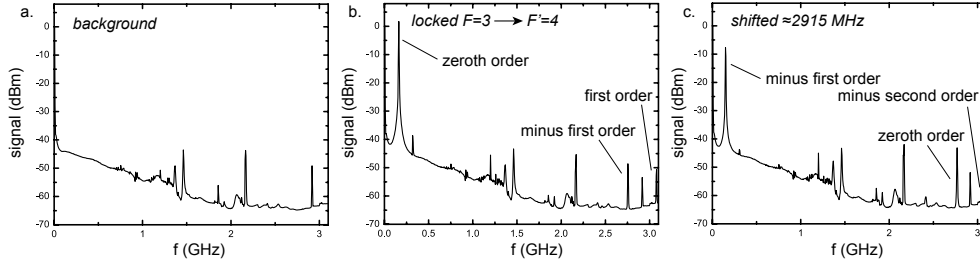[10]Rohde&Schwarz ZVH8 Cable and Antenna Analyzer

Figure 4.11 Typical examples of spectrum analyzer measurements of: (a) the background spectrum, (b) the spectrum with the laser locked at the ^{85}Rb $F = 3 \rightarrow F' = 4$ transitions and (c) the spectrum with the laser shifted $\approx$ 2915 MHz (manually). The plots show the power in the amplified photodiode signal as a function of the frequency.
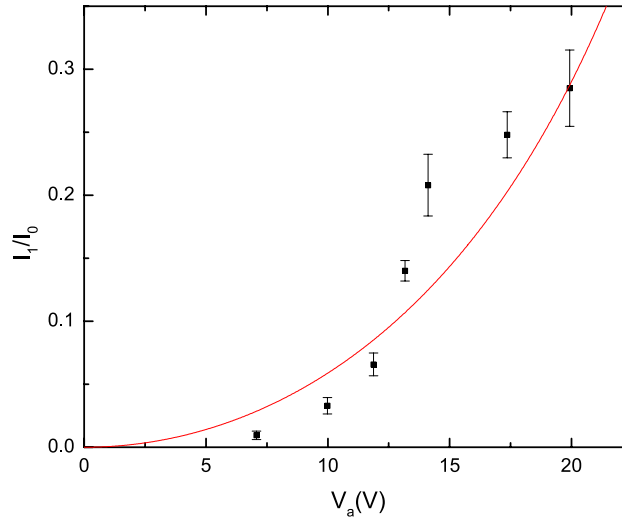

Figure 4.12 Measurement of the relative first order sideband intensity as a function of the EOM voltage. The red line is a fit of the data with equation 4.5, which resulted in a modulation depth of (23 ± 2) mrad/V_{pp}.

MHz and 2915 MHz signals. The value of this conversion factor was $\approx$150, but appeared to be slightly larger for smaller input power, therefore it was determined separately for each measurement.

The result of the measurement of the relative sideband intensity I_1/I_0 of the first order sideband with respect to the zeroth order intensity is given in figure 4.12. The error bars shown are the standard deviations of the mean of five measurements. The measurement is fitted with equation 4.5, which leads to a modulation depth β of (23 ± 2) mrad/V_{pp}. According to the data sheet of the EOM this modulation depth should be $\sim$ 15 mrad/V_{pp}. The fit does not agree very well with the data, although the general trend of the fit is in agreement with the data points. In order to do a more accurate measurement of the sideband intensity an other photodiode should be used with a flat gain over at least 3 GHz. The goal of this experiment was however to achieve first order sidebands with enough power ($\sim$ 10%) to be used as the repumper and not to fully understand the behavior of the EOM. So the conclusion of the experiment is that satisfactory sidebands of 10% are achieved at an applied voltage of $\approx$ 13V, which is reached at an RF input power of 3.5W.

This chapter gave a description of the laser system of the ABLIS setup. A double pass

AOM configuration was added to the setup in order to set the detuning of the laser. Utilizing this AOM the detuning can be scanned from -2γ to 0. Furthermore an EOM is used to create the repump beam. The intensity in this repump beam can be as high as 30 percent of the cooling beam. Therefore the laser system is now ready for laser cooling and trapping experiments.

Chapter 5

Laser cooling setup

Since the laser system is completed at this point, it is possible to perform laser cooling experiments. The experiment described in this section aims to measure the effect of laser cooling with laser-induced fluorescence (LIF), in which the atomic beam is probed with an additional laser beam. This laser beam induces fluorescence which can be detected with a CCD camera. Previous work [23] showed that the atomic beam effusing from the Knudsen cell was visible with LIF. The Knudsen cell will now be mounted onto a larger vacuum vessel in which the atomic beam will be laser cooled in two dimensions. The efficiency of this laser cooling can be tested with LIF. The goal of this experiment is to test the dependence of the laser cooling on experimental parameters such as the detuning and saturation parameter.

The first section is dedicated to the experimental setup which was built in order to perform laser cooling and compression experiments. The last section shows the results of simulations of the experiment. These simulations are performed in order to get an idea of what the fluorescence measurements will look like. In order to make these simulations realistic, the exact position and velocity distributions are needed of particles leaving the tube connected to the Knudsen cell (see figure 1.4). A Monte Carlo simulation was set up to find these distributions. The result of this simulation is compared with measurements of the transverse velocity distribution leaving the Knudsen cell, which were performed in previous work [23].

5.1   Experimental setup

As explained in the Introduction the atomic beam will be created from a Knudsen cell. The atoms will effuse into the vacuum through a collimating tube. In the experiment described here it will then be laser cooled in one dimension. The beam will then drift towards the end of the vessel, where it is probed with a laser beam to induce LIF. The effect of laser cooling the beam is a strong decrease of its divergence. This will be visible as a change in the size and density of the beam in the last vessel .

A schematic view of the beam line is shown in figure 5.1. The whole setup shown is placed on an optical table with dimensions of 2m×1m. The vacuum vessel is fabricated out of three 100CF 6-way crosses mounted to eachother. A turbo-molecular pump is connected to the center vessel which can bring the pressure down to $\sim 10^{-7}$ mbar. The atomic beam is created by the Knudsen cell, which is made from a 16CF cross piece. A schematic view of the Knudsen cell is shown in figure 5.2. The lower part of the Knudsen cell is a flexible bellows piece, in which the rubidium is contained. To load the Knudsen cell, the cross piece is opened and a glass ampule containing rubidium is placed in the bellows. After closing up, the bellows can be bent in order to break the ampule and release the rubidium. By heating the Knudsen cell, the rubidium melts and creates a vapor pressure due to which atoms will leave the cross piece through a tube with a length of 105 mm and an inner radius of 1 mm.

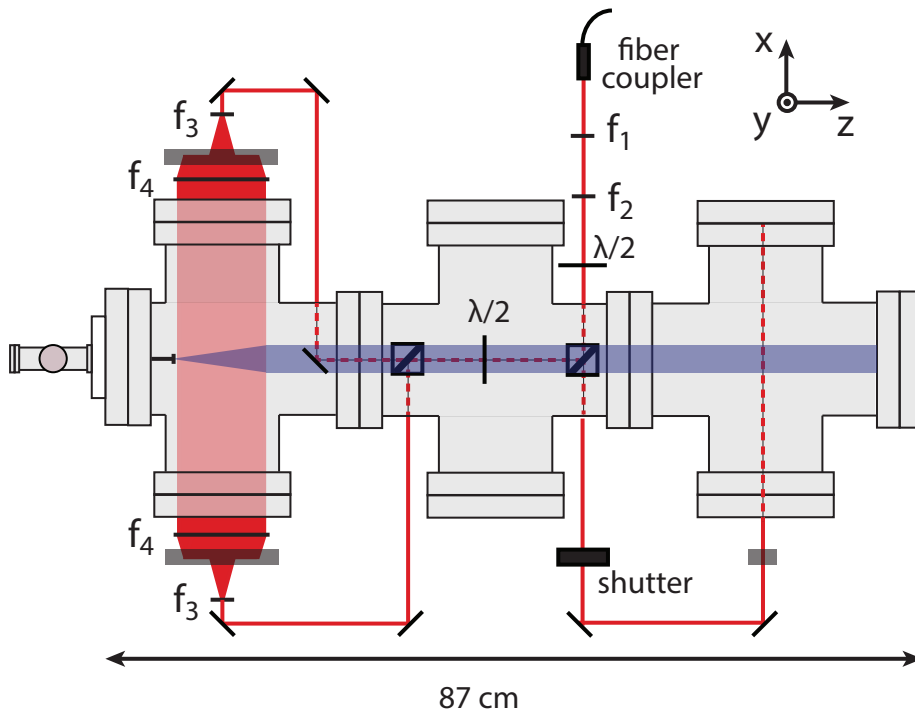The Knudsen cell is heated with four heaters connected to each flange of the cross peace

Figure 5.1 Schematic view from the top of the experiment. The laser beams are indicated in red and are dotted to indicate where they are under the vacuum vessel. The small chamber on the left is the Knudsen cell, which is connected to three larger vacuum vessels. The beam enters the table from a fiber coupler, after which it is expanded by two lenses with focal lengths $f_1 = 25$mm and $f_4 = 150$mm. Part of the laser beam is split off to form the LIF beam. The remainder is split into two parts, which form the laser cooling beams. These are expanded in two directions by the cylindrical lenses, with a focal length $f_3 = -50$mm and $f_4 = 250$mm. Three periscopic mirror configurations transport the laser beams from the table level to the middle of the vessel. The atomic beam effusing from the Knudsen cell is cooled in the first vessel and probed with a laser beam in the last vessel. The figure is not drawn to scale.
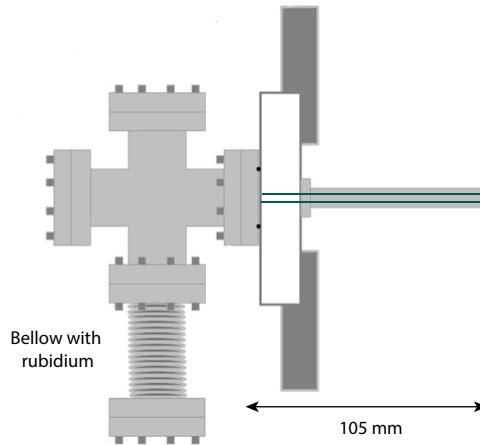
Figure 5.2 Schematic view of the Knudsen cell, which is fabricated from a 16CF cross piece. A bellows is attached to the bottom with which a glass ampule of rubidium in the inside of it can be broken. The rubidium can escape from the tube with a length of 105 mm and an inner radius of 1 mm.

and one heater to the bottom of the bellows. Thermocouples are connected to the center of the cross piece as well as the bottom of the bellows. They are read out by two temperature controllers[1] which independently control the power of the heaters connected to the bellows and the cross piece, so that a constant temperature distribution can be reached in the Knudsen cell. Furthermore, a heating wire is wrapped around the exit tube in order to prevent the rubidium from clogging it. The temperature of the cross piece and the tube are controlled independently from the bellows, so that they can be kept at a higher temperature. The idea of this measure is that most of the rubidium will stay in the bellows instead of precipitating on the walls of the cross piece and the tube.

The light of the laser system, described in chapter 4, is transported to the experiment with an optical fiber. As a free space beam, it is first magnified by two lenses (f_1=25 mm and f_2=150 mm, see figure 5.1), after which its transverse size[2] is 3 mm. A combination of a $\lambda/2$ plate and a polarizing beam splitter splits off a fraction of the beam, which is used as the LIF probe beam. The rest of the beam is split into two beams of equal fractions with a $\lambda/2$ plates and a polarizing beam splitter to create the two cooling laser beams. These are expanded in the z-direction by two pairs of cylindrical lenses (with focal lengths f_3=-50 mm and f_4=400 mm, see figure 5.1). After this expansion the aspect ratio of the beam is 8, meaning that the size in the z-direction is 24 mm. Part of the expansion happens in the vertical direction, since the beam is transported from the table level to the middle of the vacuum vessel by means of a periscopic configuration in between the two cylindrical lenses. The fluorescence light in the last vessel is imaged on a CCD detector[3] through the top viewport of the last vessel (the imaging optics and detector are not indicated in figure 5.1).

The downside of the laser configuration in the experiment is the fact that the frequency of the LIF beam cannot be tuned separately from the frequency of the trapping laser. This will be no problem for a proof of concept measurement to show that laser cooling of the rubidium beam works. However, it can become a problem for measurements of the effect of the detuning on the efficiency of the laser cooling, because changing the detuning will also change the fluorescence signal. Simulations have to be performed to test the severeness of

---

[1] OMROM E5CN-H

[2] The radius at which its intensity has dropped a factor $e^{-\frac{1}{2}}$

[3] Apogee Alta U47+ camera with a e2v CCD47-10 CCD sensor

this problem. A possible solution could be to add two double-pass AOMs to the setup to change the frequency of the LIF beam or to use a second laser.

5.2 Tube simulations

As explained in the beginning of this chapter, simulations are performed of the laser cooling experiment to test what results we can expect from LIF measurements. To make these simulations as realistic as possible we need to know what the probability distribution functions of the position and velocity of the particles will be when they leave the collimating tube of the Knudsen cell. In previous work measurements were performed of the transverse velocity distributions (an example is given in figure 5.5), by scanning the detuning of the LIF beam. Furthermore, a theoretical mode is known of such a collimating tube, which was made by Olander et al. [49]. The theoretical model however predicts the probability distribution function of the angle with which the particles leave the tube instead of the transverse velocity. These two are hard to connect since the temperature of the tube is different from the temperature of the Knudsen cell. Particles that collide with the tube will most likely thermalize with this other temperature. This process makes a calculation of the transverse velocity distribution difficult. So to connect the measurements to the theoretical model, a Monte Carlo simulation is done, whose results can be compared with both.

5.2.1 Simulation setup

The following conditions are used to set up the simulation:

- The particles do not interact, i.e., the only way their trajectory is changed, is by collisions with the wall. This is the so called transparent regime in which the mean free path of the particles is much larger then the length of the tube. For a tube with a radius of 1 mm and a length of 105 mm, this holds for temperatures $T < 100°C$ [23]

- The particles that enter the tube are distributed according to a Maxwell Boltzmann distribution $f(v_i)$ with the temperature $T_{knudsen}$ of the Knudsen cell, i.e.,

$$f(v_i) = \sqrt{\frac{m}{2\pi k_b T_{knudsen}}} e^{-\frac{mv_i^2}{2k_b T_{knudsen}}},$$ (5.1)

  in which v_i is the velocity in direction i. For the x- and y-direction the velocities are chosen from the interval $-\infty < v_i < \infty$ and for the z-direction from the interval $v_z > 0$.

- The transverse position distribution of where the particles enter the tube is uniform and uncorrelated with the initial velocity distribution.

- Particles that collide with the tube wall, will be diffusely reflected, i.e., the probability dS that a particle leaves the tube wall in the infinitesimal solid angle element $d\Omega$ is given by [50]

$$dS = \frac{\cos\theta}{\pi} d\Omega,$$ (5.2)

  in which θ is the angle with the normal of the tube. The infinitesimal solid angle element can be written as

$$d\Omega = \sin\theta d\phi d\theta.$$ (5.3)

  Therefore the probability distribution function $f(\theta)$ for the angle θ is given by

$$f(\theta) = 2\cos\theta\sin\theta,$$ (5.4)

  in which the factor 2 appears due to normalization of the distribution.

- The particles that have collided with the tube are fully thermalized with the temperature of the tube T_{tube}, i.e., the probability distribution $f(v)$ of the magnitude of the velocity v is given by a Maxwell Boltzmann distribution with temperature T_{tube},

$$f(v) = \left(\frac{m}{2\pi k_b T_{tube}} \right)^{\frac{3}{2}} 4\pi v^2 e^{-\frac{mv^2}{2k_b T_{tube}}}. \tag{5.5}$$

In the simulation a particle starts at the beginning of the tube, i.e., $z = 0$. The transverse initial positions x_0 and y_0 are chosen randomly out of a uniform distribution, but in such a way that $\sqrt{x_0^2 + y_0^2} < r_t$, in which r_t is the radius of the tube. The velocities are chosen randomly out of the distributions given in equation 5.1. With the initial positions and velocities, the position at which the atom hits the tube for the first time is calculated. This is done by equating the time dependent radial position to the radius of the tube

$$\sqrt{(x_0 + v_{x,0}t)^2 + (y_0 + v_{y,0}t)^2} = r_t. \tag{5.6}$$

This equation is solved for the time, leading to

$$t = \frac{-v_{x,0}x_0 - v_{y,0}y_0 + \sqrt{r^2 \left(v_{x,0}^2 + v_{y,0}^2 \right) - \left(v_{y,0}x_0 - v_{x,0}y_0 \right)^2}}{v_{x,0}^2 + v_{y,0}^2}. \tag{5.7}$$

The coordinates x, y and z at which the atom hits the tube wall for the first time are calculated with,

$$\begin{aligned} x &= x_0 + v_{x,0}t, \\ y &= y_0 + v_{y,0}t \text{ and} \\ z &= z_0 + v_{z,0}t. \end{aligned} \tag{5.8}$$

The next step is to randomly pick an angle with which the atom leaves the tube according the distribution function given in equation 5.4. This is the angle the new trajectory of the atom makes with the normal of the tube. Furthermore a polar angle ϕ is picked randomly from a uniform distribution between 0 and 2π and a velocity v is picked randomly from the distribution given in equation 5.5. From these three variables the three new velocity components v_x, v_y and v_z can be calculated. This is done by first calculating the velocity $v_\perp$ perpendicular to the surface, the velocity v_z in the z-direction and the other velocity in the plane tangent to the surface of the tube $v_{//}$. From figure 5.3 these velocities are determined to be

$$\begin{aligned} v_z &= v\sin\theta\sin\phi, \\ v_{//} &= v\sin\theta\cos\phi \text{ and} \\ v_\perp &= v\cos\theta. \end{aligned} \tag{5.9}$$

The relation between $v_\perp$ and $v_{//}$ on the one hand and v_x and v_y on the other hand is dependent on the angle α, which is defined in figure 5.4 and equal to

$$\alpha = \arctan\frac{y}{x}. \tag{5.10}$$

Using this value of α, v_x and v_y can be written as

$$\begin{aligned} v_x &= v_{x,2} - v_{x,1} = v_{//}\cos\alpha - v_\perp\sin\alpha \\ v_y &= -v_{y,2} - v_{y,1} = -v_{//}\sin\alpha - v_\perp\cos\alpha \end{aligned}. \tag{5.11}$$
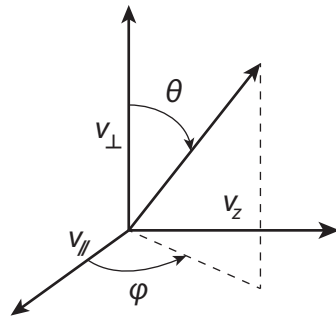
65

Figure 5.3 A schematic view of the three velocities $v_\perp$ perpendicular to the surface, v_z in the direction of the tube and $v_{//}$ in the plane of of the tube and perpendicular to v_z.
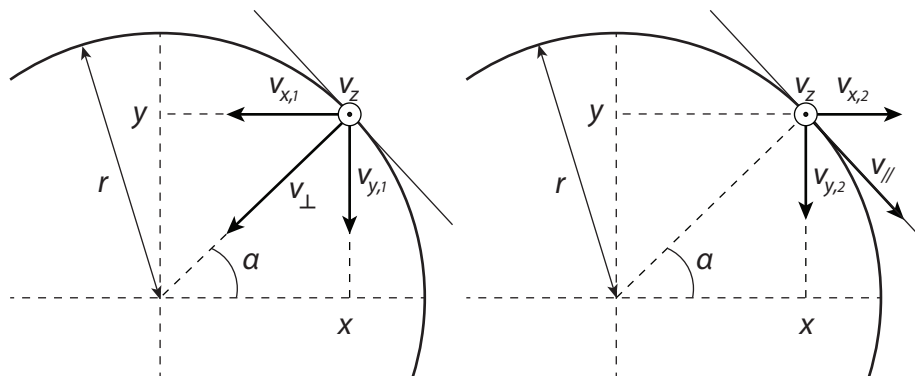

Figure 5.4 A schematic view of the the relation between $v_{//}$ and $v_\perp$ on the one hand and v_x and v_y on the other hand.

Now the new position, velocity and direction of the particle are known the next position where the particle hits the tube is calculated. First, the time which is needed to reach the wall of the tube again, is calculated. Since the particle is at the tube wall now $x^2 + y^2 = r_t^2$. With this constraint, solving equation 5.6 leads to

$$t = -\frac{2\left(xv_x + yv_y\right)}{v_x^2 + v_y^2}.$$
(5.12)

This time is substituted in equation 5.8 together with the old positions x,y and z (filled in as x_0, y_0 and z_0), to find the new positions again. This procedure is repeated until the particle leaves the tube, which happens when either $z < 0$ or $z > L$, in which L is the length of the tube. When $z > L$ the transverse positions x_{end} and y_{end} where the particle leaves the tube are calculated. The time needed to reach the end of the tube from the last position at the wall is given by $t = \frac{L-z}{v_z}$. Therefore x_{end} and y_{end} are given by

$$x_{end} = x + v_x \frac{L-z}{v_z}$$
$$y_{end} = y + v_y \frac{L-z}{v_z}.$$
(5.13)

To make the statistical error in the obtained distributions as small as possible, the whole procedure is repeated a certain number of times such that the number of particles which reaches $z > L$ is ten million.

5.2.2 Simulation results

A plot of the angular distribution obtained with the simulation is shown in figure 5.6, which also shows a theoretical angular distribution. Both were obtained for a tube with a radius of r_t=1 mm and a length of L=105 mm. The angular distribution gives the probability that a particle leaves the tube under an angle θ with the normal of the tube exit. The theoretical distribution $f(\theta)$ was derived by Olander et al. [49]. With this distribution the probability dP that a particle leaves the tube through the solid angle element $d\Omega = \sin\theta d\phi d\theta$ can be written as $dP = f(\theta)\sin\theta d\phi d\theta$. Therefore the distribution plotted in figure 5.6 is $\sin\theta f(\theta)$. As can be seen, the simulated distribution is exactly the same as the theoretical one.

The most important information obtained from the simulation is the transverse velocity distribution. Figure 5.5 shows the simulation result for the transverse velocity distribution together with a measurement performed in previous work [23]. The simulation was performed for equal temperature of the Knudsen cell as in the experiment, i.e., $T_{knudsen}$= 80°C. The temperature of the tube was taken at 100°C, although it is not sure this was also the case in the experiment.

In general, the two are very much alike, the widths of the distributions are of the same order. However, the measurement seems to be broader in the center and has a less extended 'tail'. The reason for this difference can be caused by several experimental issues. First of all the measurement was performed with two laser beams in the vessel, instead of only the LIF beam. They were spatially separated from each other, but it is not certain the second beam or a reflection of it did not interact with the atoms in the imaged part of the vessel. Also, after taking apart the setup, the tube of the Knudsen cell was found to be bent a little bit, which also may have disturbed the measured velocity distribution. It can however be concluded that the analytical model describes the velocity distribution function well, since the simulation results are in general in agreement with the measurements as well as with the model.

An interesting feature of the simulations is the fact that it can test whether there is a correlation between the radial position r at which a particle leaves the tube and the angle θ under which it does it. If this is not the case, simulations of the tube are not necessary
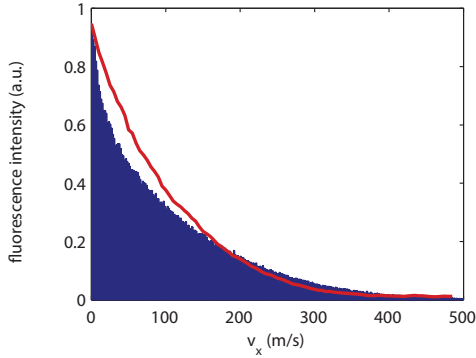
Figure 5.5 A plot of the transverse velocity distribution obtained from the simulation (blue histogram) and from the measurement (red line). The data of the measurement was taken from [23].
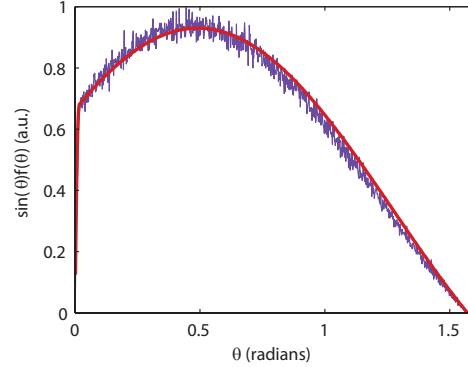

Figure 5.6 A plot of the theoretical angular distribution (red line), and the angular distribution obtained with the simulations (blue line).

anymore in the future, since all information about the distributions is known. The probability distribution $f(r, \theta)$ at the exit of the tube can then be written as $f(r)f(\theta)$. These analytical distributions could then serve as the starting point of any laser cooling simulations.

In order to test the existence of correlations between r and θ, it is assumed that the position distribution is uniform, i.e., $f(r) \propto r$. If the position and angular distribution would be uncorrelated the combined probability distribution would be equal to the product of the individual distributions, i.e., $f(r, \theta) \propto rf(\theta)$. Figure 5.7 shows a density plot of this distribution as well as one of the simulated distribution. Overall, the two are very similar, but there is a subtle difference. The simulated distribution seems to be rotated a little bit, which indicates a small correlation. The explanation of this effect is as follows. Assume a particle leaves the tube under a certain angle θ at a radial position r. Then the last position at the wall of the tube z_{last} is given by

$$z_{last} = L - \frac{r_t + r}{\tan\theta}. \tag{5.14}$$

Furthermore, a particle has a larger probability of originating from a smaller z_{last}, since a particle simply has a larger transmission probability for smaller longitudinal positions. Therefore a particle has a larger probability of leaving the tube at larger radial positions, but how much larger is dependent on the angle with which it leaves the tube, due to the $1/\tan\theta$ term in equation 5.14. In principle it should be possible to calculate the θ dependent radial position distribution, which takes into account the correlation, but it is outside the scope of this thesis. To make the simulation in section 5.3 as realistic as possible and take the correlation between r and θ into account, the positions and velocities of simulated particles in this section are used as the starting positions and velocities in the laser cooling simulations in the next section.

5.3 Laser cooling simulations

Now that we know the velocity and position distribution of particles leaving the collimating tube of the Knudsen cell, it is possible to perform simulations of the laser cooling experiment. In order to do so a software called COOL is used [51]. As input for this software the simulation results of the previous section are used, i.e., the end positions and end velocities of the simulated particles. The COOL software propagates the particles through the laser cooling stage and determines the probability that a particle absorbs a photon during each of
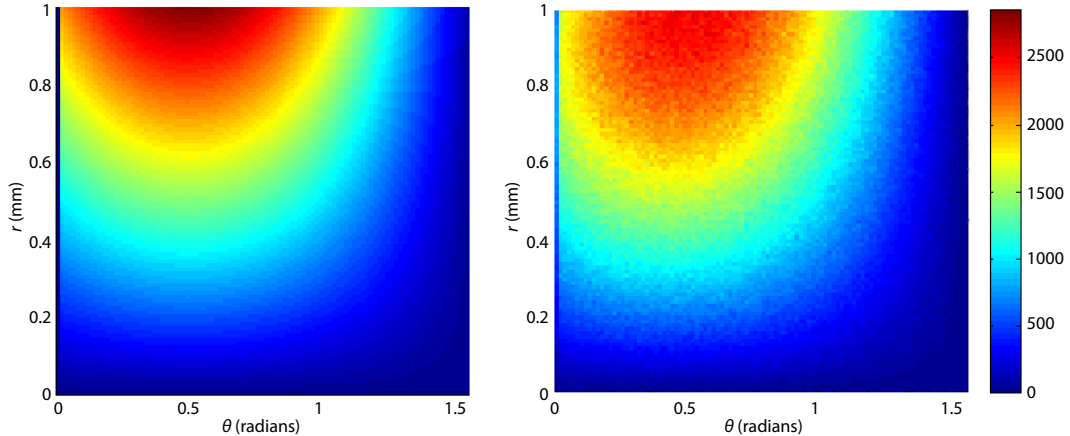
Figure 5.7 Left: Theoretical probability distribution $f(r, \theta)$ under the assumption of a uniform position distribution and no correlations between θ and r. **Right:** Simulated probability density distribution.

the time steps. Whether the particle actually absorbs a photon is based on a Monte Carlo algorithm. When this happens the atom experiences the recoil momentum kicks as discussed in section 1.3.

The configuration used in the simulations is based on the experimental setup discussed in section 5.1. Two uniform, counter-propagating radiation fields are applied to the atomic beam which extend over 5 cm in the longitudinal direction and are cut off at 2.5 mm in the transverse direction. The atoms then propagate 60 cm in the z-direction to a second laser beam whose rms transverse size is 3 mm. A shutter time of the CCD camera was assumed of 1 s. Which part of the fluorescent light is captured in the image of the CCD-camera within this shutter time was determined in previous work [23]. This was implemented in the simulation such that realistic pixel counts are obtained. The simulations were performed for different detunings δ and saturation parameters s of the laser cooling field. The power in the LIF beam is always kept at 1 mW, which matches a saturation parameter of $s_{LIF} \approx 1$. Unless stated otherwise, the detuning δ_{LIF} of the LIF beam is kept at the same value as δ.

Figure 5.8a shows an example of what the CCD image will look like. This simulation was performed for $\delta = -\frac{\gamma}{2}$ and $s = 1$. The average number of counts per pixel in the illuminated part of the image is well above the noise level of the camera, so it can be concluded that the effect of laser cooling should be experimentally realizable. Simulations like this one are performed for different detunings and saturation parameters.

To quantify the effect of changing the laser cooling parameters, for each simulation the number of counts in the center ten percent of pixels of the center column (indicated by the red box in figure 5.8) is calculated. Figure 5.9 shows the result of this number of counts as a function of the saturation parameter. By taking this number of counts, we only look at a certain fraction of the total phase space volume and all counts in that fraction are summed. A certain phase space volume is selected since we only look at the center part of the beam, i.e., we only look at particles for which $|x| < 0.1 l_{CCD}$, in which l_{CCD} is the size of the CCD detector. Furthermore we only look at particles for which the Doppler shift is smaller than the linewidth of the transition, which means we already select atoms based on their x-velocity. Therefore the number of counts in that volume should be proportional to the phase space density, i.e., the reduced brightness, of the beam. To see if this is indeed true, the reduced brightness is also plotted in figure 5.9. This brightness is calculated by determining the radius of a circular area that includes 1 nA of current. From all particles within this radius the brightness is calculated according to equation 1.1. As can be seen the
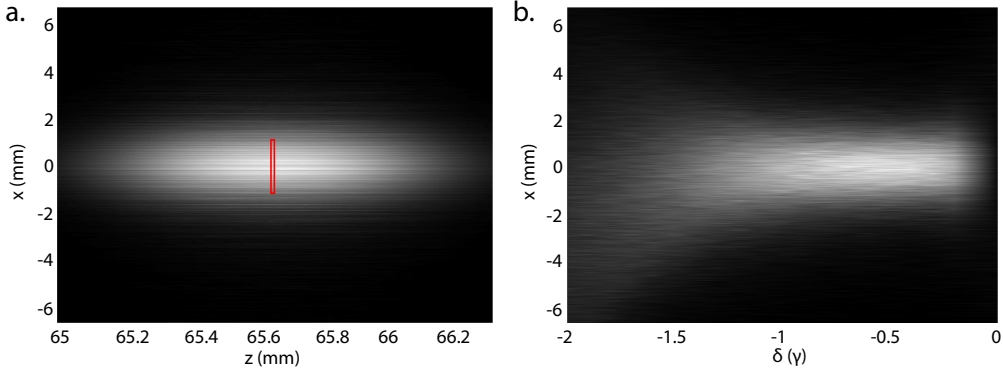
Figure 5.8 a. A plot of a simulated CCD image for $\delta = -\frac{\gamma}{2}$ and $s=1$. The z position is measured from the end of the tube. The red box indicates the pixels that are integrated in order to quantify the laser cooling. **b.** Plot of the center row of pixels against the detuning ($s=1$).

number of counts in the earlier mentioned region is indeed a good measure for the brightness.

To see the effect of changing the detuning, figure 5.8b shows a plot of the center column of pixels (at the highest intensity of the LIF beam) as a function of the detuning. As can be seen, the fluorescence profile is broader when the detuning is larger (more negative). This is due to the fact that laser cooling is less effective for larger detunings. For larger detunings the fluorescent profile also slightly shifts away from the center of the beam line, as is most clearly visible at $\delta = -2\gamma$ in figure 5.8b. This is caused by the fact that the detuning of the LIF beam is equal to the detuning of the laser cooling beam. When the LIF detuning is larger, the population of atoms that will absorb photons is shifted to higher velocities, since these atoms will be resonant with the laser beam due to the Doppler shift. Due to the drift of the atoms this population is however also displaced from the center of the beam.

In order to better quantify the detuning data, again the number of counts in the center ten percent of pixels of the center column is calculated. Figure 5.10 shows a plot of this number against the detuning. To check whether it is a problem that the detuning of the LIF beam cannot be set separately from the detuning of the cooling beam, figure 5.10 also shows the same results but for $\delta_{LIF} = 0$. As can be seen it gives a bit higher number of counts at larger detunings. This is caused by the fact that it always excites the atom population with a velocity around 0 m/s, which is also the population in the center of the beam, due to the drift of the atoms. The difference between the two is not very large however, so it can be concluded that it is no problem that the detuning of the LIF beam cannot be detuned separately from the cooling beam.

Figure 5.9 A plot of the number of counts in the center ten percent of pixels of the center column of the CCD-detector as a function of the saturation parameter for $\delta = -\frac{\gamma}{2}$ (left y-axis) together with a plot of the brightness as a function of the saturation parameter (right y-axis).
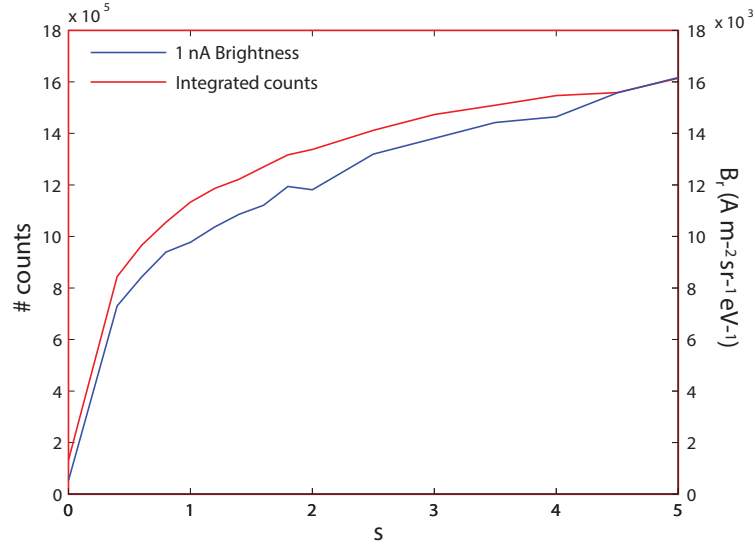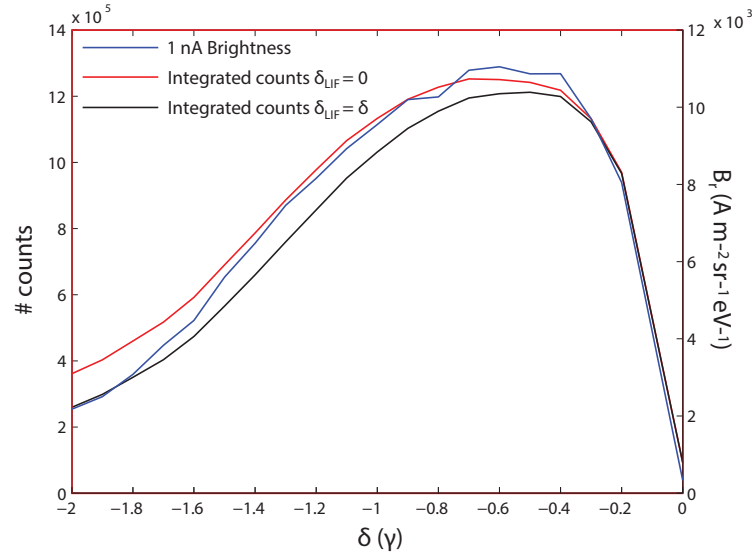

Figure 5.10 A plot of the number of counts in the center ten percent of pixels of the center column of the CCD-detector as a function of the detuning for $\delta_{LIF} = \delta$ and $\delta_{LIF} = 0$ (left y-axis) together with a plot of the brightness as a function of the detuning (right y-axis).

Chapter 5 Laser cooling setup

Chapter 6

Conclusion

The Atomic Beam Laser-cooled Ion Source (ABLIS) is a new source for focused ion beams (FIBs), which are popular tools to measure and modify structures at the nanometer length scale in the semiconductor industry. In the ABLIS an atomic beam is made with a Knudsen cell filled with rubidium vapor. The rubidium leaving the Knudsen cell forms an atomic beam which is laser-cooled and -compressed in two dimensions. When leaving the Knudsen cell the atoms go through a collimating tube, which aims to let through the atoms that can be cooled and compressed but sent back the atoms that can not. In this way the lifetime of the system will be increased, since the rubidium in the Knudsen cell is depleted on a slower pace. After the laser cooling and compression stage the beam is photo-ionized by means of two very intense lasers and the ions are immediately accelerated to their required energy (mostly 30 keV). Finally it is focused to an as small as possible spot with an electrostatic lens configuration.

The first two chapters of this report were dedicated to investigations of the performance limits of an ABLIS-based FIB. The last two chapters described the progress made in its experimental realization.

In chapter 2 the effect of disorder-induced heating on the ion beam quality was investigated. Previous work [22] included predictions that the brightness of the atomic beam after the laser cooling and compression stage can be as high as $2 \cdot 10^7$ $\mathrm{Am^{-2}sr^{-1}eV^{-1}}$. However, particle tracking simulations showed that when this beam is ionized, a lot of this brightness is lost due to disorder-induced heating at current above ≈ 20 pA. More investigations were needed to better understand the phenomenon, especially its dependence on experimental parameters such as the acceleration field strength E_a, the flux density ϕ and the beam current I. In this report an analytical model was set up to describe the evolution of the velocity distribution in the extended regime and inside the acceleration stage. Furthermore, particle tracking simulations were performed to investigate the effects in other regimes, such as the pencil beam regime, and in the whole setup.

The analytical model was based on the extended two particle model by Jansen et al. [28]. A first order perturbation approximation and the assumption of an extended beam had to be made to find an analytical solution to the problem. Therefore the result, an equation for the width of the velocity distribution as a function of experimental parameters, is only valid while the beam is inside the acceleration stage and for large currents ($I \gtrsim 10$ nA). When these constraints are fulfilled the evolution of the velocity distribution is described very well, as was verified with particle tracking simulations. As expected it predicted a larger beam temperature for smaller acceleration fields E_a and larger flux densities ϕ.

Particle tracking simulations showed that the pencil beam regime, in which no transverse heating of the beam takes place, could be extended by applying a larger acceleration field. It was found that the current at which the pencil beam regime ends, scales with $E_a^{\frac{2}{5}}$ and $\phi^{\frac{1}{5}}$. With practically realizable acceleration fields (≈ 5 MV/m) it is possible to extend the pencil

beam regime to ≈70 pA. The acceleration field may be as small as 50 kV/m to sufficiently suppress disorder-induced heating at a current of 1 pA.

In the third chapter, the knowledge about disorder-induced heating acquired in chapter 2 is used to analytically predict the minimum spot size that can be reached with the ABLIS focused ion beam. The electric field needed to suppress disorder-induced heating is used to calculate the energy spread, and thus the chromatic aberration of the lens system, associated with it. The effects of the brightness and chromatic and spherical aberration of a realistic lens system are combined into a single spot size. This analysis revealed that a spot size of 0.2 nm can be reached at a current of 1 pA. At this current the spot size will be limited by spherical aberration and the brightness of the beam. However, in order to reach this small spot size, the size of the ion beam has to be large (≈10 μm) at the objective lens. This can only be reached with either an ion beam line of at least ≈2.5 m or an extra lens. A particle tracking simulation was performed of the complete ion beam line, including an additional Einzel lens to create the large beam size at the objective lens. The simulation confirmed the analytical result that a spot size of 0.2 nm can be reached. The ion beam length to reach this spot size was only 68 cm due to the added Einzel lens.

The fourth chapter dealt with experimental work in which the laser setup was extended and prepared for laser cooling and trapping experiments. A method is implemented to detune the laser frequency in which is made use of a double pass AOM configuration. By conveniently locking the laser to the $F' = 2, 4$ crossover transition, only one AOM is needed. This AOM is passed twice so that no laser beam deflection occurs after passing through the configuration. By changing the frequency of the AOM, the detuning of the laser frequency from the ^{85}Rb laser cooling transition can now be set from -2γ to 0. Furthermore, a repump beam is created by using an EOM. By driving the EOM with an RF frequency equal to the difference between the cooling transition and the repump transition, the first order sideband of the EOM can be used as the repump beam. At an RF input power of ≈3.5 W the intensity of this first order sideband was ten percent of the intensity of the zeroth order. This should be more than enough to perform laser cooling and trapping experiments.

In the last chapter, an experimental setup to perform laser cooling experiments is described. This setup was built in the lab and aims to measure the effect of the detuning δ and the saturation parameter s on the laser cooling. The earlier constructed Knudsen cell [23] is mounted on a larger vacuum system which is placed on an optical table at which the optics for the laser cooling experiment are mounted. Directly after leaving the collimating tube of the Knudsen cell, the atomic beam will be laser-cooled in one direction. The beam will then drift to the end of the vacuum system where it will be probed by another laser beam. This beam will induce fluorescence which is measured with a CCD-detector.

To test the performance of the setup, simulations were performed of the laser cooling and laser induced fluorescence. As input for these simulations a position and velocity distribution of particles leaving the collimating tube is needed. Measurements of the transverse velocity distribution of particles leaving the tube were performed in previous work, but were not fully understood yet. Therefore, a Monte Carlo simulation was set up of the particles in the collimating tube, in order to find the desired distributions. The result of this simulation is in good agreement with the earlier performed measurements of the transverse velocity distribution as well as with an analytical model of the angular distribution, by Olander et al. [49].

The output of the tube simulation, i.e., the position and velocity distribution of particles leaving the tube, was used as the input of laser cooling simulations. These simulations are performed with COOL [51], a code that is also based on a Monte Carlo algorithm. It tracks the positions and velocities of a certain number of particles through a region with laser radiation. With the results of this simulation the positions and velocities of the particles are calculated at the position of the LIF beam. The results show that it is possible to measure the effect of δ and s on the laser cooling with laser-induced fluorescence; it is possible to extract a measure for the brightness of the laser-cooled beam from the LIF data.

Bibliography

[1] G. Moore. *Cramming more components onto integrated circuits*. Electronics pages 114–117 (1965).

[2] *www.itrs.net*.

[3] M. Phaneuf. *Applications of focused ion beam microscopy to materials science specimens*. Micron **30**, 277 (1999).

[4] F. S. L.A. Giannuzzi. *A review of focused ion beam milling techniques for tem specimen preparation*. Micron **30**, 197204 (1999).

[5] S. Reyntjens and R. Puers. *A review of focused ion beam applications in microsystem technology*. J. Micromech. Microeng. **11**, 287 (2001).

[6] P. Hawkes and E. Kasper. *Principles of Electron Optics vol. 2: Applied geometrical optics*. Academic Press (1989).

[7] V. Raffa, P. Castrataro, A. Menciassi, and P. Dario. *Applied Scanning Probe Methods II NanoScience and Technology*, chapter 11. Focused Ion Beam as a Scanning Probe: Methods and Applications, pages 361–412 (2006).

[8] J. Orloff. *The liquid metal ion source, a brief introduction*. In *Coldbeams : ultra-COLD gas for Bright Electron and Monochromatic ion Source* (2012).

[9] C. W. Hagen, E. Fokkema, and P. Kruit. *Brightness measurements of a gallium liquid metal ion source*. J. Vac. Sci. Technol. B **26**, 2091 (2008).

[10] A. E. Bell, K. Rao, G. A. Schwind, and L. W. Swanson. *A low-current liquid metal ion source*. J. Vac. Sci. Technol. B **6**, 927 (1988).

[11] B. Ward, J. Notte, and N. Economou. *Helium ion microscope: A new tool for nanoscale microscopy and metrology*. J. Vac. Sci. Technol. B **24**, 2871 (2006).

[12] R. Livengood, S. Tana, R. Hallstein, J. Notte, S. McVey, and F. Rahman. *The neon gas field ion sourcea first characterization of neon nanomachining properties*. Nucl. Instr. and Meth. in Phys. Res. A **645**, 136140 (2011).

[13] *Orion nanofab from zeiss at http://microscopy.zeiss.com*.

[14] S. Tan, R. Livengood, D. Shima, J. Notte, and S. McVey. *Gas field ion source and liquid metal ion source charged particle material interaction study for semiconductor nanomachining applications*. J. Vac. Sci. Technol. B, **28** (2010).

[15] D. Jun, V. Kutchoukov, and P. Kruit. *Ion beams in sem : An experiment towards high brightness low energy spread electron impact gas ion source*. J. Vac. Sci. Technol. B **29** (2011).

Bibliography

[16] M. Reijnders. *Ion Beams from Laser-cooled Gases*. Ph.D. thesis, Eindhoven University of Technology (2010).

[17] H. Metcalf and P. van der Straten. *Laser Cooling and Trapping*. Springer (1999).

[18] *CRC Handbook of Chemistry and Physics*. CRC press, 92 edition (2011-2012).

[19] N. Debernardi, R. van Vliembergen, and W. Engelen. *Optimization of the current extracted from an ultracold ion source*. New J. of Phys. **14** (2012).

[20] J. O. B. Knuffman, A.V. Steele and J. McClelland. *Nanoscale focused ion beam from laser-cooled lithium atoms*. New Journal of Physics **13** (2011).

[21] P. Mutsaers, E. Vredenbregt, and O. Luiten. *Open technologieprogramma - ultracold fib*. STW proposal (2011).

[22] R. Notermans. *A New High-Brightness Ion Source: the Atomic Laser-cooled Ion Source*. Master's thesis, Eindhoven University of Technology (2012).

[23] B. Jansen. *Atomic beam source for the Ultracold Focused Ion Beam setup*. Master's thesis, Eindhoven University of Technology (2013).

[24] P. Kruit and G. Jansen. *Space Charge and Statistical Coulomb Effects*. Taylor & Francis Group (2009).

[25] H. Boersch. *Experimentelle bestimmung der energieverteilung in thermisch ausgelsten elektronenstrahlen*. Zeitschrift fr Physik **139**, 115 (1954).

[26] T. Tang. *Statistical dynamics theory of the space charge effects in a charged particle beam*. Optik **76**, 38 (1987).

[27] J. Bittencourt. *Fundamentals of Plasma Physics*. Springer, 3rd edition (2004).

[28] G. Jansen. *Coulomb Interactions in Particle Beams*. Ph.D. thesis, Technische Universiteit Delft (1988).

[29] T. Killian, T. Pattard, T. Pohl, and J. Rost. *Ultracold neutral plasmas*. Physics Reports **449**, 77=130 (2007).

[30] J. van Leeuwen and G. Jansen. *Statistical limitations in electron-beam lithography .1. theory*. Optik **65, 3**, 179 (1983).

[31] V. Zolotarev. *One-dimensional Stable Distributions*. American Mathematical Society (1983).

[32] K. Riley, M. Hobson, and S. Bence. *Mathematical methods for physics and engineering*. Cambridge.

[33] *http://www.pulsar.nl/gpt/*.

[34] B. Zimmermann. *Broadened energy distributions in electron beams*. Advances in Electronics and Electron Physics **29**, 257 (1970).

[35] H. Wiedemann. *Particle accelerator physics*. Springer (2007).

[36] M. Born and E. Wolf. *Principles of Optics: electromagnetic theory of propagation, interference and diffraction of light*. Pergamon Press (1984).

[37] P. Hawkes and E. Kasper. *Principles of Electron Optics: Basic geometrical optics*. Academic Press (1989).

[38] Y. Wang and Z. Shao. *Design principles of an optimized focused ion beam system.* Advances in Electronics and Electron Physics **81**, 177 (1991).

[39] B. van der Geer. *Predicted performance of the ultracold fib.* internal memo (2013).

[40] J. Barth and P. Kruit. *Addition of different contributions to the charged particle probe size.* Optik **101, No. 3**, 101 (1996).

[41] B. Knuffman, A. Steele, and J. Mclelland. *Cold atomic beam ion source for focused ion beam applications.* J. Appl. Phys. **113** (2013).

[42] F. Trager, editor. *Springer Handbook of Lasers and Optics.* Springer (2012).

[43] *Operators's manual. The Coherent 899-21 Titanium:Sapphire Ring Laser, Section 1.*

[44] G. Kirchmair. *Frequency stabilization of a Titanium-Sapphire laser for precision spectroscopy on Calcium ions.* Ph.D. thesis, Leopold Franzens University of Innsbruck (2006).

[45] D. McCarron, S. King, and S. Cornish. *Modulation transfer spectroscopy in atomic rubidium.* Meas. Sci. Technol. **19** (2008).

[46] *Instruction manual, Model AOM-40N Acousto-optic light modulator, IntraAction Corp.*

[47] E. Black. *An introduction to pound-drever-hall laser frequency stabilization.* Am. J. Phys. **69**, 79 (2001).

[48] D. Steck. *Rubidium 85 d line data.* available online at http://steck.us/alkalidata/.

[49] D. Olander and V. Kruger. *Molecular beam sources fabricated from multichannel arrays. iii. the exit density problem.* J. Appl. Phys. **41**, 2769 (1970).

[50] R. Feres and G. Yablonsky. *Knudsen's cosine law and random billiards.* Chem. Eng. Sci. **59** (2004).

[51] E. Vredenbregt and K. van Leeuwen. *Laser cooling and trapping visualized.* Am. J. Phys. **71**, 760 (2003).